Svein Brekke

Techniques for enhancement of temporal resolution in three-dimensional echocardiography

Thesis for the degree of philosophiae doctor

Trondheim, May 2007

Norwegian University of
Science and Technology
Faculty of Medicine
Department of Circulation and Diagnostic Imaging

NTNU
Innovation and Creativity

NTNU
Norwegian University of Science and Technology

Thesis for the degree of philosophiae doctor

Faculty of Medicine
Department of Circulation and Diagnostic Imaging

©Svein Brekke

ISBN 978-82-471-3117-6 (printed ver.)
ISBN 978-82-471-3120-6 (electronic ver.)
ISSN 1503-8181

Theses at NTNU, 2007:142

Printed by Tapir Uttrykk

Teknikkar for betre tidsoppløysing i tredimensjonal ekkokardiografi

Bakgrunn: Ultralydbilde av hjartet, ekkokardiografi, er eit viktig diagnoseverktøy for kardiovaskulær sjukdom, og den etablerte todimensjonale bildedanninga viser bevegelsen til hjartemuskelen i sann tid utan blodige inngrep på kroppen. Trass i desse fordelane har kardiologar ønskt seg tredimensjonal (3D) datainnsamling i sann tid heilt sidan ultralydavbilding vart oppfunnen. Fram til nyleg måtte høgkvalitets 3D ultralydbilde av hjarte settast saman av data frå fleire hjartesyklar.

Den mest fundamentale avgrensinga for innsamlingsrate av ultralydbilde kjem frå lydfarten, som er er omlag 1540 m/s i mjukt kroppsvev. I todimensjonal ultralydavbilding skaper ikkje dette problem: Sjølv om ein legg stor vekt på biletkvalitet, kan moderne ultralydskannerar samla inn meir enn 50 gråtonebilder per sekund.

Når ein tek opp eitt enkelt 3D volum av det venstre hovudkammeret, kan så mange som 4000 ultralydstrålar vera påkrevd for å oppnå tilstrekkeleg biletkvalitet. Sidan kvar puls må forplanta seg minst 0.25 m (12.5 cm kvar veg), vil samla tilbakelagt avstand for lydpulsane i eit slikt volum ofte overstiga 1000m, noko som med rett-fram skanning vil gje så låg opptaksrate som 1.5 volum per sekund.

Resultat: I denne avhandlinga undersøker vi to teknikkar for å oppnå betre tidsoppløysing av 3D ultralydopptak: *i)* biletmorfing - ein teknikk som ved å bruka eit estimat for hastigheitsfeltet til vevet i hjartemuskelen reknar ut meir nøyaktige tilnærmingar for mellomliggande biletrammer, og *ii)* ein ny og betre metode for rekonstruksjon, kor ein nyttar ei matriseprobetil å gjera fortløpande rekonstruksjon (volumfletting) og presentasjon av data tekne opp over fleire hjartesyklar. Volumflettinga er i avhandlinga brukt til 3D hjarte-opptak både på vaksne og på foster, og ein eigen teknikk for sykronisering av fosterhjarteopptak - tissue Doppler gating (TDOG) - er særskilt utvikla for dette formålet.

Prototypar har blitt implementert både for morfealgoritmen og for volumfletting i sann tid, og resultat blir presentert i avhandlinga som bilde og filmsekvensar.

Vi konkluderer med at både biletmorfing og sanntids volumfletting kan bli verdifulle byggeklossar i ultralydskannarar som blir konstruert i framtida.

Kandidat: Svein Brekke
Institutt: Sirkulasjon og bildediagnostikk, i samarbeid med Nasjonalt Senter for Fostermedisin, St. Olavs Hospital, Trondheim
Vegleiarar: Prof. Hans G. Torp og postdoc. Erik N. Steen
Finansieringskjelde: Norges Forskningsråd, IKTHELSE

Avhandlinga nemnt over er funnen verdig til å forsvarast offentleg for graden "PhD i medisinsk teknologi". Disputasen finn stad i audioriet, Medisinsk-teknisk Forskningssenter, fredag 28. september 2007, klokka 12:15.

Summary

Echocardiography is an important tool for diagnosis of cardiovascular disease, and the established two-dimensional imaging techniques provide non-invasive visualization of the myocardium, produced in real time with compact ultrasound scanners. However, getting live three-dimensional (3D) images from the heart has been an aspired goal ever since ultrasonic imaging was invented. Just until the last few years, high-quality 3D images of the heart needed to be gated, i.e. reconstructed from two-dimensional data acquired over several heart cycles (similar to how 3D cardiac MR images are formed).

The most fundamental limitation to the acquisition rate of ultrasonic images is posed by the speed of sound, which is about 1540 m/s in soft human tissue. In two-dimensional imaging, this is not a hard restriction: depending on image quality trade-offs, one easily gets a satisfactory real-time response with more than 50 frames per second.

When doing a full 3D scan of the left ventricle, as much as 4000 ultrasonic beams may be necessary to achieve acceptable image quality. As each pulse needs to propagate at least 0.25 m (12.5 cm each way), the propagation distance of the scan can add up to over 1000 m and, consequently, the volume rate in straight forward scanning would be as low as 1.5 acquired volumes per second.

In this thesis, two techniques for improved temporal resolution are investigated: *i)* image morphing, which utilizes a velocity field estimate obtained during the imaging process to calculate intermediate image frames with improved accuracy and *ii)* improved gating techniques, which utilize a matrix transducer for gated acquisition with on-line slice display and volume rendering. The gating technique has been utilized for cardiac scanning - both of adults and fetuses - and a special technique for gating of fetal heart imaging has been developed as well.

Prototype implementations have been done for both the morphing algorithm and the real-time gated acquisition principle, and resulting images are presented in the thesis.

We conclude that both image morphing and real-time gating are potential building blocks in future ultrasound scanners.

Preface

After finishing the siv.ing. education in applied mathematics, I spent eight years working with software development for ultrasound systems at NTNU, SINTEF and GE Vingmed Ultrasound. The most important appeal this field of science has to me is the interaction between medicine and technology. The years at the technology-side of the field of medical ultrasound taught me many details regarding the equipment construction but less about signal processing and medical applications. I realized that working with a Ph.D. thesis would give me an opportunity to broaden my intellectual horizon and get in a better position for doing inspiring research work in the university or in the ultrasound industry.

Acknowledgments

The presented thesis has been submitted to the Faculty of Medicine at the Norwegian University of Science and Technology to be defended for the Ph.D. degree. I am thankful to the Faculty of Medicine and the Department of Circulation and Medical Imaging at NTNU for hosting me during the work of the thesis, to National Center for Fetal Medicine at St. Olavs Hospital, Trondheim, for the fruitful research cooperation regarding fetal cardiac imaging, and to GE Vingmed Ultrasound for providing access to top-quality ultrasound scanners as well as an office during the work. I thank the Norwegian Research Council for a 3 year PhD. scholarship - without this funding the thesis would not have been made.

Many people have contributed in various ways to make it possible for me to complete the thesis, and I want to thank all of you: First of all, I am grateful for the way my supervisor Hans G. Torp has initiated me into the field of acoustics and signal processing, as well as willingly shared his knowledge in ultrasound imaging. Furthermore, Erik N. Steen has been the co-supervisor of the thesis and a helpful and constructive discussion partner regarding some of the papers in the thesis and the introduction. Eva Tegnander and Sturla H. Eik-Nes have given invaluable help in data acquisition and concept validation when working with the papers addressing fetal echocardiography. For the volume stitching paper, Stein Inge Rabben made valuable contributions both through data simulation and text revision, Asbjørn Haugen and Geir Haugen implemented the acquisition setup for the volume stitching, and Asbjørn Støylen kindly added data acquisition for the experiments in the paper to an already planned clinical trial. In the morphing paper, Charlotte B. Ingul did the wall motion scorings and Svein Arne Aase set up the selection of test data to score. Stian Langeland kindly reviewed the speckle tracking part of the introduction. I am grateful for the help Nancy Lea Eik-Nes, Åshild Brekke, and my wife Anne Stensrud have given with text revision, and I appreciate the encouragement and support Kjell Arne Ingebrigtsen has given, sharing his long experience in the field. I would furthermore thank my co-PhD-

students at the Department of Circulation and Medical Imaging – Lasse, Jonas, Tore, Torbjørn, Svein Arne, Peter, Jøger and Fredrik – for fruitful discussions and adequate hiking. Many former and future colleagues in GE Vingmed have also been supportive in the work: The Bergen team, counting Ditlef, Olve and Rune, the acquisition experts, Asbjørn, Geir and Anders S, as well as the GUI- and 3D experts Sevald and Anders T.

Finally, I want to thank my wife Anne and my two children Magnus (6) and Sofie (3) for enduring my frustrations and forcing me to keep the right perspective on the thesis work (the thesis has been my *work*; not my *life*). Thank you so much for being patient and supportive.

Bergen, May 2007

Svein Brekke

Nomenclature

The following notation is used in the text (order of definition follows approximately order of occurence in text):

λ	Wave length of an acoustic wave
T_p	Pulse period (duration)
A	Aperture size of the transducer
r	Distance along an ultrasound beam
$f_\#$	F-number, the ratio between the focal distance and the aperture size
PSF	Point spread function
$\mathrm{sinc}(x)$	Defined as $\frac{\sin x}{x}$ when $x \neq 0$ and 1 when $x = 0$
$f_{x,y}(z)$	Resampling of ultrasound volume data along a view-ray in a volume rendering
∇	The gradient operator for a scalar field
$C(x, y)$	Resulting color pixel value in position (x, y) of the view plane during volume rendering
f_0	Transmit frequency for an acoustic pulse
Δf	Doppler frequency shift for a reflected acoustic pulse
$z(t)$	A complex Gaussian process
$R(m)$	The auto-correlation of lag m (m is an integer) of a stationary complex Gaussian process
$R_N(m)$; R_m	Estimator for $R(m)$ using N consecutive samples from the process
$\mathcal{F}(f)$	The temporal Fourier transform of the function f.
$G(\omega)$	The effect spectrum of a complex Gaussian process
$X(t)$	A two-dimensional image frame acquired at time t
$d(K_1, K_2)$	A metric for quantifying the difference between kernel images in speckle tracking, f.i. SAD or correlation coefficient
$\mathbf{r}$	Arbitrary 3D position

$\mathbf{r}_{ij}$; $\mathbf{r}_{ijk}$	A position in a 2D or 3D scanning grid
$K(\mathbf{r}, X)$	An kernel picked at location $\mathbf{r}$ in the image X
$\hat{\mathbf{d}}_{ij}$	Displacement estimate at position $\mathbf{r}_{ij}$ between successive image frames
$\hat{\mathbf{v}}(\mathbf{r})$	Velocity vector estimate at position $\mathbf{r}$
$\hat{\mathbf{V}}$	Velocity field estimate in an image or volume
$X(\mathbf{r}, t)$	Echo amplitude as function of space and time
$\hat{X}(\mathbf{r}, t)$	Estimated echo amplitude in a morphing of image data
$\mathcal{O}(\text{expr})$	Big-o notation for computational complexity
S, B	Number of ranges and beams in a 2D scanning grid
N_i,N_j,N_k	Number of ranges, azimuth beams and elevation beams in a 3D scanning grid
i,j,k	Range, azimuth and elevation index in a 3D scanning grid
ξ_{ijk}; I_{ijk}	The time-gain compensated echo amplitude value at $\mathbf{r}_{ijk}$
z; z^*	Complex number; complex conjugate
t	Acquisition time, with $t = 0$ corresponding to the first pulse firing time of a 3D scan
t_m; m	Acquisition time of the mth 3D volume is t_m
n; N	Cardiac cycle number and number of cycles in a recording. $n \in \{1, 2, \cdots, N\}$
T_n	QRS trig times, $n \in \{0, 1, \cdots, N\}$
τ	Relative cycle time. $\tau \triangleq (t - T_{n-1})/(T_n - T_{n-1})$, with $T_{n-1} \leq t \leq T_n$
M_n	The number of volumes acquired in cycle number n
$c_n(t)$	Local stitching cost - high cost implies poor match between two specific stitched sub volumes
C	Global stitching cost - high cost implies that some of the stitched sub volumes in a recording had a poor match

Contents

Norwegian summary i
Summary iii
Preface v
Nomenclature vii
Figures and tables xii

Introduction **1**
1 Three-dimensional ultrasonic imaging 2
1.1 Data acquisition 3
1.2 Presenting 3D ultrasound images 9
1.2.1 Volume rendering vs. surface rendering 10
1.3 Clinical benefits of 3D echocardiography 13
1.4 Imaging the fetal heart 13
2 Temporal resolution 15
2.1 Parallel beam processing 15
2.2 ECG-gated 3D imaging 17
2.3 Morphing 18
3 Velocity estimation 19
3.1 The Doppler effect 19
3.2 Autocorrelation 20
3.3 Speckle tracking 22
4 Summary of papers 25
5 Discussion 27
6 Conclusion 31
References 31

A Increasing frame rate in ultrasound imaging by temporal morphing using tissue Doppler **A-1**
1 Introduction A-2
2 Theory A-4

2.1 Tracking motion in deforming bodies A-4
2.2 Impact of the velocity field estimate on morphed images . . A-7
3 Method and material A-8
3.1 Speckle tracking A-8
3.2 Local velocity estimator A-9
3.3 Velocity curves and anatomical tracking A-11
3.4 Velocity field estimates A-11
3.5 Morphed cine-loops A-12
3.6 Test of diagnostic value A-13
4 Results A-13
4.1 Local velocity estimators A-14
4.2 Velocity field estimates A-14
4.3 Image quality of morphed cine-loops A-19
4.4 Test of diagnostic value A-19
5 Discussion A-21
5.1 Local velocity estimator A-21
5.2 Image quality of morphed images A-22
5.3 Test of diagnostic value A-23
5.4 Future work A-23
6 Conclusion A-24
References A-24

B Volume stitching in three-dimensional echocardiography: Distortion analysis and extension to real-time B-1
1 Introduction B-2
2 Methods B-5
2.1 Data acquisition B-5
2.2 Stitched cine-loop playback B-6
2.3 Real-time stitching B-8
2.4 Experiment A: Examination efficiency B-9
2.5 Experiment B: Simulations based on a kinematic model . . B-10
2.6 Volume measurements B-12
2.7 Geometrical distortion B-13
3 Results B-14
3.1 Real-time stitching and cine-loop display B-14
3.2 Experiment A: Examination time B-19
3.3 Experiment B: Simulated ultrasound data B-19
3.4 Volume measurements B-19
3.5 Geometrical distortion B-22
4 Discussion B-22
4.1 Cine-loop display with stitched images B-22

4.2 Real-time stitching B-22
4.3 Experiment A: Examination efficiency B-23
4.4 Experiment B: Volume measurements and geometrical distortion B-23
5 Conclusion B-25
References B-26

C Tissue Doppler gated (TDOG) dynamic 3D ultrasound imaging of the fetal heart C-1
1 Introduction C-2
2 Methods C-3
2.1 Data acquisition C-3
2.2 Reconstruction C-4
2.3 Gating signal accuracy C-4
3 Results and discussion C-5
3.1 Image quality C-5
3.2 Gating signal C-6
3.3 Validating tissue Doppler gating signal by comparison to CW Doppler C-7
3.4 3D data acquisition C-9
3.5 3D reconstruction C-9
3.6 Alternative approaches C-12
4 Conclusion C-12
References C-13

D Tissue Doppler gated (TDOG) real-time stitching in three-dimensional fetal echocardiography D-1
1 Introduction D-2
2 Methods D-2
2.1 Real-time TDOG signal D-2
2.2 Real-time volume stitching D-4
3 Results D-5
3.1 Real-time TDOG signal D-5
3.2 Real time volume stitching D-6
4 Discussion D-6
4.1 Real-time detection of peaks in the TDOG signal D-6
4.2 Volume stitching in-vivo D-8
5 Conclusion D-8
References D-8

Figures and tables

List of figures

1 The human myocardium post mortem 2
2 Different ways to form an acoustic wave front 3
3 Signal processing steps for 3D ultrasound 4
4 Propagation of a pressure wave in a homogeneous medium 6
5 The point spread function (PSF) 7
6 Surface rendering is a technique for 3D visualization 11
7 Volume rendering of the myocardium 12
8 Cardiac views from the fetal heart 14
9 The principle of parallel beam processing 16
10 Two ways to temporally interpolate between successive image frames 18
11 The Doppler effect 19
12 2D velocity vector estimation by speckle tracking 23

A.1 Left panel: Interpolation in Euler coordinates A-5
A.2 A possible path $\bar{\mathbf{r}}(t)$ of one anatomical location in the image. . . . A-6
A.3 Traditional and Doppler aided speckle tracking in a sector scan . . A-9
A.4 Displacement and velocity estimates throughout a cardiac cycle from a material point in the ventricular septum A-15
A.5 Displacement and velocity estimates from a material point in the LV lateral wall A-15
A.6 Displacement and velocity estimates in the ventricular septum . . A-16
A.7 A movie showing the B-mode cine-loop used in figures A.4-A.6 . . A-17
A.8 Velocity field calculations based on tracking of the anatomic structure A-18
A.9 A dilating left ventricle of a healthy adult person A-20

B.1 Data from different scanning volumes and different cardiac cycles . B-5
B.2 One frame in each of the first four cycles of a real-time stitched scan B-6
B.3 Two different algorithms for temporal alignment of subvolumes . . B-7

B.4 Simulating an ultrasound scan by sampling individual beams from a kinematic model B-11
B.5 A stitched scan acquired over four cycles presented in two ways . . B-14
B.6 A four-cycle stitched cine-loop with a stitching artifact in the middle seen due to respiration B-15
B.7 A four-cycle stitched cine-loop with artifacts due to uneven heart rate B-16
B.8 Correlation plots for three different recordings B-18
B.9 Simulated ultrasonic images of the left ventricle B-20
B.10 Curves showing the development of LV cavity volume B-20
B.11 Maximal geometrical distortion $d_{max}(\tau)$ B-21

C.1 B-mode image quality for different frequencies and beam density settings C-5
C.2 The basic signal shown together with the derived gating signal . . C-6
C.3 Visual control of gating accuracy C-7
C.4 Doppler CW data through the umbilical artery and M-mode data through the atrioventricular area C-8
C.5 The B-mode image on the left is recorded immediately after the 3D acquisition C-10
C.6 Volume projections of the heart of a fetus aged 24 weeks C-11

D.1 Processing chain of the real-time TDOG gating technique. D-3
D.2 Division of a volume scan into subvolumes using TDOG stitching . D-4
D.3 TDOG signal with trigger times calculated in real-time from 3D tissue Doppler data D-6
D.4 Three planar slices taken from a 3D cine-loop in a TDOG stitched 4D scan D-7
D.5 Same setup as in figure D.4, but with an irregular TDOG signal . D-7

List of tables

A.1 Size of the drift correction terms A-14
A.2 Wall motion score of 16 segments A-19

B.1 Resulting acquisition rate for a volumetric scan for different stitching configurations B-12
B.2 Examination time and the resulting stitching cost B-17
B.3 List of fractonal difference between estimated and real LV cavity volume B-21

Introduction

The evolution of medical ultrasound started more than half a century ago: The first *in-vivo* images were published by Wild and Neal in 1951[74]. The images showed echo amplitude as a function of depth, a presentation mode referred to as A-mode (amplitude mode). Three years later, the first ultrasonic M-mode (motion mode - intensity image with time and depth along the axes) images of the heart were presented[22] under the name echography, a term that later evolved into echocardiography. The echography recorder was able to both show the images in real time on an oscilloscope and expose light from the oscilloscope onto a 35mm film strip, thereby capturing and storing analog ultrasonic data. The same year, Wild showed two-dimensional (2D) ultrasound images (later named B-mode images, similar to radar B-scans) of breast tumors in-vivo. It is also striking that *in-vivo* volume-projections on an oscilloscope of three-dimensional (3D) ultrasound data was demonstrated as early as 1956[32], many years before the term «computer graphics» was invented!

While the first B-mode images were reconstructed from M-mode scans, devices for real-time cardiac B-mode scanning with a frame rate of 15-25 frames per second became available around 1970[13;49]. In the 70s, echocardiographic examinations became more common, and in the 80s, the ultrasound Doppler technique for visualization of blood flow became available[34]. The combination of morphology studies of the myocardium by B-mode and hemodynamic investigation with 2D color Doppler made echocardiography a popular and powerful diagnostic tool. Later advances in the field of medical ultrasound imaging have been numerous, and informative historical reviews exist[23;44].

During the 90s and 00s, there has been increasing interest in three-dimensional ultrasound imaging of the heart. Achieving an adequate update rate of a volumetric scan is very challenging due the limitation of the acquisition rate posed by the speed of sound, which is about 1540 m/s in soft human tissue. In two-dimensional imaging, this is not a hard restriction: depending on image quality trade-offs one easily gets a satisfactory real-time response with more than 50 frames per second. When doing a full 3D scan of the left ventricle, as much as 4000 ultrasonic beams

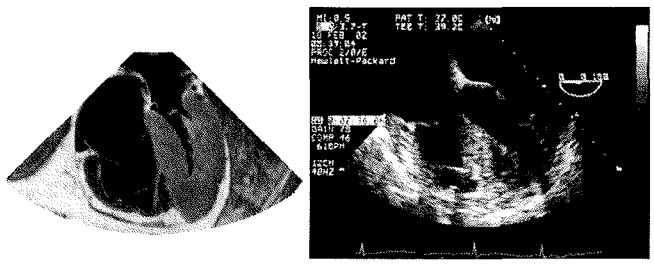

Figure 1: The human myocardium post mortem (left) and in-vivo depicted by ultrasonic imaging (right) (image from anaesthetist.com[1]).

may have to be acquired to achieve acceptable image quality. As each pulse needs to propagate at least 0.25 m (12.5 cm each way), the propagation distance of the scan can add up to over 1000 m and, consequently, the volume rate in straight forward scanning would be as low as 1.5 acquired volumes per second. Different techniques for increasing the volume rate of 3D ultrasound images exist, and the work in this thesis aims to improve some of these techniques.

This thesis is divided into two parts: This first part is an introduction to the subject of three dimensional echocardiography and some of its applications, providing background material to and discussing the impact of the second part, consisting of four papers (three published or accepted for publication in journals with peer review and one proceedings paper).

After this overview, the introduction continues with a short initiation into the principles of ultrasound imaging. The challenges of real-time acquisition and presentation of 3D images are discussed, and a brief historical review of equipment for 3D imaging is given in section 1.

Section 2 of the introduction points out the specific challenges with temporal resolution in 3D ultrasound imaging - some of which are addressed in the papers. Section 3 gives an introduction to velocity measurements performed by ultrasound systems, dwelling on both the Doppler method and the speckle tracking method.

A short summary of the papers presented in chapters A to D is given in section 4, and finally a discussion of the contributions made by the papers is presented in section 5.

1 Three-dimensional ultrasonic imaging

Ultrasound backscatter imaging is a safe, non-invasive technique for investigating the morphology of inner organs. Figure 1 shows the difference between a real human myocardium and an ultrasonic depiction of the same organ.

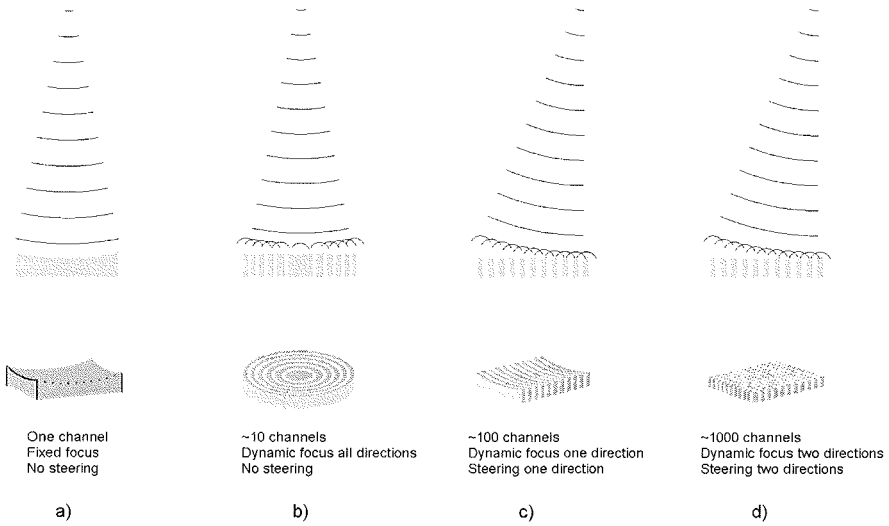

Figure 2: Different ways to form an acoustic wave front and steer the propagation direction: a) the shape of the transducer is directly imposing the initial wave form; b) Concentric transducer elements are activated with a small time delay between each channel, c) An array of stick-formed transducer elements are activated with delays, ensuring both focus and one-directional steering, d) A matrix of transducer elements are activated with delays, enabling both two-dimensional focus and steering in two directions.

1.1 Data acquisition

Ultrasound images are formed by emitting short, pulsed pressure waves into soft tissue and detecting backscattered signals. To get information about the positions of scatterers in the depicted region, both the transmitted pressure wave and the received signal are focused, as sketched in figure 2.

An ultrasound scanner is a device that utilizes a transducer to send and receive ultrasonic pulses in a scheme resulting in two- or three-dimensional images. The main processing steps in the image formation is shown in figure 3.

Different transducer types exist (single element transducers, annular arrays, phased arrays, linear arrays, matrix transducers) which use different techniques to beam focusing[4]. Transducer types for cardiac imaging are illustrated in figure 2: a) shows a curved transducer surface, activated by a one-channel electronic signal, thus directly imposing the initial wave-form in the propagation medium;

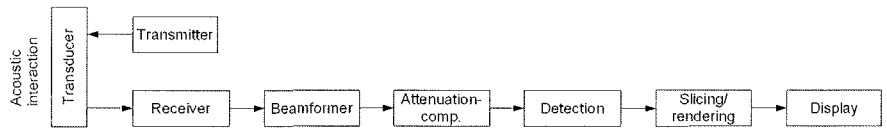

Figure 3: Signal processing steps for 3D ultrasound intensity mapping.

b) shows a transducer consisting of a small number of concentric rings. The transmitted beam may either be focused by curving the array surface, or by activating the ring-elements individually (inner elements are activated with a small delay compared to the outer elements). The resulting beam thereby has coherent oscillation in the focus point, and the circular symmetry gives accurate focusing in all directions in the focal plane. c) shows a phased array transducer consisting of stick-formed elements with a fixed geometric focus in the elevation direction, but an adjustable focus depth in the azimuth direction when the delays are adjusted. Finally, d) shows a phased matrix transducer, where transducer elements are positioned in a two-dimensional grid. Since delays may vary between elements both in azimuth and elevation direction, a matrix transducer is capable of focusing the beam in both directions.

Fixed focus transducers have limited imaging capability compared to array transducers although, for example, in high frequency (30-50 MHz) cardiac imaging of mice, the simplicity single element transducers provide is still attractive [61]. Annular array transducers were widely used in commercial scanners in the 1980s, and the circular symmetry of the beam propagation have beneficial properties for producing high-quality images with a low number of electronic channels. However, the propagation direction of the beam is always normal to the transducer surface, and therefore the transducer itself must be moved when a scanner acquires 2D or 3D images.

Phased array transducers have overcome this limitation, as illustrated in figure 2 c): By giving larger delays in the outer right elements than in the outer left, the direction of the transmitted beam may be changed electronically (the beam may be *steered* in the azimuth direction), as long as the inter-element distance does not exceed a half wave length [4]. Similarly, matrix transducers are able to steer the beam in both azimuth and elevation direction.

The reflected signal is processed in the same manner as the transmitted beam is formed: The signals registered by each array element are summed with individual delays added to each channel. In this way one can configure both the

direction of echo registration and the focus depth (i.e., the depth at which all channels have coherent contributions as illustrated in figure 4). Modern ultrasound scanner apply dynamic focus when setting up the delays for the receive signal: The delays of each channel are dynamically changed corresponding to the depth of the echo, thus ensuring that the received beam is correctly focused at all depths.

To achieve a three-dimensional image, the beam propagation direction must be possible to steer in two directions. This may be achieved by mechanical steering in both directions, by electronic steering in both directions or by steering one direction mechanically and the other direction electronically. Historically, mechanical beam steering has played an important role in both 2D and 3D ultrasound imaging. It requires less computational power since fewer acoustic receive channels needs to be processed compared to electronic steering. When imaging an organ which is stationary, like a breast, a kidney or a liver, the acquisition time of a data volume need not be very short, and thus both mechanical scanning and electronic scanning may give satisfactory image quality.

The heart, on the other hand, has substantial motion with a typical peak wall motion velocity of 10 cm/s. To accurately capture the geometry of the myocardium in a given time point one needs a short capture time, and thus a purely mechanical scanning scheme for a 3D data set is not feasible.

The amount of data needed for a detailed three-dimensional image is extensive: A pyramidal volume covering the left ventricle must in many cases be as wide as $65° \times 65°$, and even a modest lateral resolution of $1°$ imposes more than 4000 beams in a data volume. The propagation time for this amount of ultrasonic beams at a scan depth of 15 cm would alone add up to more than $\frac{3}{4}$ second, making straightforward 3D imaging of myocardial dynamics impossible, at least for a full cardiac scan.

An ideal ultrasound system for 3D cardiac imaging therefore needs to overcome some difficult challenges: *i)* It should have a sufficient number of elements for two-dimensional beam steering, e.g. a quadratic 3 MHz transducer with 16×16 mm aperture and $\lambda/2$ pitch would require $64 \times 64 \approx 4000$ elements. *ii)* All elements should be connected to a dedicated sender capable of emitting a precisely timed ultrasonic pulse and accurately register the echo amplitude at high sampling rate.

Imaging system characteristics

The detail resolution of an ultrasound image is settled by the range resolution and the lateral resolution.

The range resolution is limited by the length of the transmitted pulse: If two scatterers are positioned close to each other along a scan line, the two backscattered pulses will overlap if the distance between the scatterers is small enough.

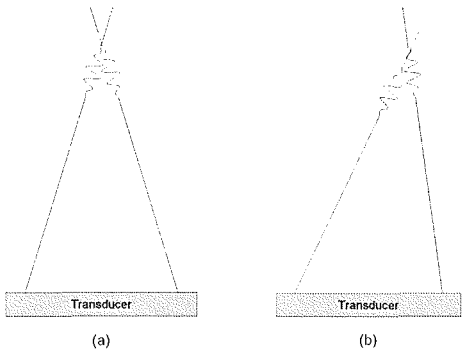

Figure 4: Propagation of a pressure wave in a homogeneous medium. a) In the focus point, all contributions to the wave front are coherent. b) Away from the focus point, the phase of the contribution to the pressure wave front varies over the transducer's aperture.

When utilizing a pulse with duration T_p, the minimal depth difference the imaging can resolve is[4]: $\Delta r = \frac{1}{2}cT_p$.

The lateral resolution is limited by the combined width of the transmitted beam and the received beam. Figure 4 (a) shows how all contributions to the pressure wave amplitude are coherent in the focus point, while in (b), different parts of the aperture contributes with varying phase to the accumulated pressure wave at field points away from the beam axis. The resulting pressure wave amplitude will therefore have the maximum at the beam axis and reduced amplitude on both sides. The relative amplitude as a function of lateral displacement is called a beam profile, and the one-way beam profile has the form of the Fourier transform of the aperture[4]. For a rectangular aperture function with width a in a 2D imaging system focused at depth r, the one-way beam profile is $I_{tx}(x) = \text{sinc}\,\frac{\pi a x}{r\lambda}$ having it's first zero at $f_{\#}\lambda$, where $f_{\#} \triangleq \frac{r}{A}$ is the F-number of the imaging system, λ is the wave length and A is the aperture of the transducer. The distance $w_{beam} = f_{\#}\lambda$ is commonly used as an estimate of the beam width of the imaging system[4], corresponding to the -5 dB width of the beam profile. This estimate for the beam width is called the Rayleigh criterion for lateral resolution.

The two-way profile is calculated as the product of the transmit profile and the receive profile. For a rectangular aperture with the same focusing on transmit and receive, the two-way profile becomes $I(x) = I_{tx}(x)I_{rx}(x) = \text{sinc}^2\frac{\pi a x}{\lambda x}$. However, current ultrasound scanners generally have I_{tx} that differs from I_{rx}, due to dynamic receive focus, to parallel beam processing (see section 2) and to

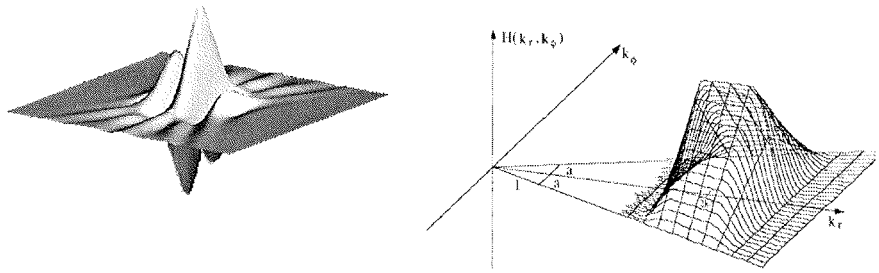

Figure 5: The point spread function (PSF) for a focused, two-dimensional imaging system. Left: The amplitude of a propagating pressure wave in the focal point (from dukemil.egr.duke.edu[68]), right: The spatial Fourier transform of the point spread function (from Angelsen[4]).

harmonic imaging.

Harmonic imaging is a mode where the backscattered signal is registered at the second harmonic frequency. This yields half the wave-length in I_{rx} compared with I_{tx}, thus practically doubling the lateral resolution. However, second harmonic echo is weaker than the echo in the fundamental frequency, and therefore the signal to thermal noise ratio is decreased. On the other hand, the second harmonic echo is better than the fundamental when it comes to reverberation suppression (i.e., multiple echoes). In most real-life cases, second harmonic images show superior image quality compared to images formed with fundamental frequency echoes[35].

The spatial resolution of the imaging system may be formalized through the *point spread function* $PSF(\mathbf{r}|\mathbf{r}_0)$, which is the same as the image of a single punctual scatterer in $\mathbf{r}_0$[4]. Figure 5 illustrates the notion of the point spread function in the time domain (left) and in the frequency domain (right).

It is normally assumed that the imaging system is focused in $\mathbf{r}_0$. A basic property one desires for an imaging system is translational invariance, which in our case means that the image is unaffected by probe translation. A spatially invariant imaging system has a PSF with

$$PSF(\mathbf{r}|\mathbf{r}_0) = PSF(\mathbf{r} - \mathbf{r}_0) \tag{1}$$

Sparse matrix arrays

One way to implement a real-time 3D ultrasound scanner without the complexity of a complete matrix transducer, is to remove some of the elements in the transducer layout. This type of transducer is called *sparse matrix* transducer. A scanner utilizing a regularly sparse matrix transducer for real-time volumetric imaging was presented by Smith and von Ramm in 1991 [51;58], and in 1997, Volumetrics Medical Imaging introduced a commercial scanner utilizing these results [36].

However, sparse transducers have several shortcomings compared to fully sampled transducers: The SNR and hence the contrast resolution is lower, both due to a higher side-lobe level and a smaller total element area which gives lower sensitivity when receiving the echoes [30]. If apodization is applied to each transducer element in an optimized way, the side-lobe level can be lowered a bit compared to the non-apodized case, but at the cost of wider main lobe implying lower spatial resolution [30]. The SNR can also be improved by utilizing a periodically sparse array, i.e., designing the element pattern differently for transmit- and receive beam in such a way that they extinguish each other's side-lobes [7].

Furthermore, harmonic imaging is not feasible with sparse arrays, due to the combination of low power in the harmonic echo and low sensitivity of the sparse transducer. Since harmonic imaging generally improves image quality and is a customary technique in cardiac imaging, sparse transducers do not appear to be attractive when aiming for the best possible image quality.

Fully sampled matrix arrays

Introduced in 2002, the Sonos 7500 from Philips Medical System (Andover, MA, USA) was the first commercial ultrasound system capable of recording 3D data in real time with a fully sampled matrix transducer, thus introducing the second generation of real time ultrasound systems [31]. In 2004, GE Vingmed Ultrasound (Horten, Norway) introduced the Vivid 7 Dimension as the second scanner with a fully sampled matrix transducer.

A matrix transducer for cardiac imaging, with $\lambda/2$ pitch at 3 MHz and aperture of 1-2 cm (to fit between the ribs) should have an element count of magnitude $64 \times 64 \approx 4000$ elements. Direct cabling from each element to the transducer would result in a cable too thick to be practically usable. Therefore, scanning systems with matrix transducers need to do some beam processing in the probe in order to reduce the number of independent signals from the probe to the scanner. This may be done by organizing the transducer elements into groups [39], where the internal delays within each sub-aperture group are processed by electronic circuits in the probe [55].

The fully sampled matrix transducers show a substantial increase of image quality compared to the first generation 3D scanners[31].

1.2 Presenting 3D ultrasound images

The graphic processing capacity of personal computers has improved vastly over the last decade. Specialized graphic hardware (PC graphic cards with a graphic processing unit - a GPU) have not only become cheaper and more powerful, but also the tools for making graphic processing programs have also become more flexible, thus making it possible for 3D ultrasound visualization algorithms to be executed on GPUs. Hence, the recent advances of computer technology have removed one of the primary obstacle for implementation of real-time 3D ultrasound imaging systems.

The principles of 3D ultrasonic imaging was described and scanning equipment sketched[32], two decades before the raster computer display was invented[33]. Thus, one can say that 3D ultrasonography has been a potentially feasible technology that needed a certain technological level to materialize.

Presenting a 3D data set on a 2D output device, such as a computer screen, is not straightforward. Several different presentation modes are available, each having strengths in certain use cases:

Fixed-layout slicing Slicing is an easy and computationally effective way to present a 3D data set: The intersections of the data set with predefined 2D planes in fixed positions are displayed in separate windows on the screen. A commonly used mode is to simultaneously present an azimuth scan, an elevation scan and an orthogonal scan (i.e. orthogonal to the beam propagation direction). This mode gives an immediate overview of the data and, when used in real-time acquisition, a scanning interface similar to B-mode scanning.

Volume rendering For a chosen view direction, each pixel location in the viewing window correspond to a straight line through the data set. This line intersects a number of voxels, and the data value in these voxels may be combined in different ways to determine the intensity of the output pixel. Volume rendering algorithms utilize all (or a range of) these voxel values when projecting the data set onto the output bitmap. Section 1.2.1 describes different algorithms for volume rendering.

Free slicing Volume rendering has the problem that objects in the foreground occlude objects further back in the scene. Even when using a projection method with transparent pixels, important details in the volume data may be hidden in the projection. Free slicing, i.e. showing a cut-plane of the

data set where the position and orientation of the plane is interactively controlled by the user, is a simple, yet effective, way to explore hidden details in the data set. Free slicing is also often combined with volume rendering - only the data behind the view plane is shown, thus reducing the problem with occlusion compared to rendering of the entire volume.

Stereoscopic display A stereoscopic display is a display device that, in order to make an illusion of depth, presents slightly different images to the left and right eye. Each of the two visualizations of the scene utilizes a perspective projection adapted to the view-point of the corresponding eye. There are different ways to implement this: specially designed glasses and monitors (the monitor switches between the two projections and the glasses «multiplexes» the two images to the corresponding eyes), blue and red colored glasses emphasizing colored overlays in the image, and finally specially designed monitors that can simultaneously project two separate images, each having a narrow view angle so that each eye only sees one image. Stereoscopic display of ultrasound images has been proposed several times [32;46;51], but has not yet become common in clinical use.

Virtual reality Virtual reality (VR) is a 3D and interactive presentation of a virtual «world». When used as a display technique for echocardiographic data, this virtual world is the human myocardium represented by a volumetric ultrasound scan. An example of VR visualization equipment is a CAVE, which consists of five large imaging screens constituting a small room (images are projected on the attic, the floor and three of the walls). Although attempts to utilize VR visualization of clinical echocardiographic data have been made[67], no significant benefit of this method has been established.

1.2.1 Volume rendering vs. surface rendering

There are two different approaches to follow when creating modern three-dimensional computer visualizations: Surface rendering, in which light transmission is simulated for a geometric model consisting of a (large) number of mathematically described surface elements, and volume rendering, where the data are sampled in a 3D grid and the displayed images are directly derived from the volume data.

It is common for surface rendering algorithms to model each object in the scene as a set of planar triangles illuminated by a light source, as shown in figure 6. For each pixel in the view plane, a light-ray through this pixel is traced backwards to the first intersecting triangle in the scene, and reflections from the light sources are simulated on the triangle surface[71], and different surfaces in the scene may have individual light reflection parameters. The tracing can additionally, to improve the realism of the rendered scene, be carried out for several reflections for each light ray.

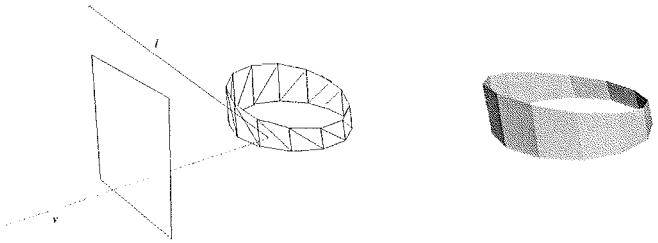

Figure 6: Surface rendering is a technique for 3D visualization where light-rays are traced from virtually defined light sources, via reflections on mathematically represented objects, to a two-dimensional imaging plane.

The surface rendering technique has applications in various fields, and the processing hardware for surface rendering computations has improved drastically, becoming a lot cheaper also, during the last decade. The computer games industry has been the main driving force for this rapid technological progress, but other fields such as CAD systems, petroleum industry and medical visualization, have benefited from the development, too.

Surface rendering based on manually segmented volume data has been presented for various applications in medical ultrasound, for example in gynecology[12], in radiology[26] and in cardiac imaging[28].

Surface renderings derived from volumetric ultrasound data may be appealing when used to study the morphology of the heart. However, the technique is normally not fully automated, the extraction of a meaningful surface model from the volume data is challenging even when manual input is used. Volume rendering is hence a more immediate way to present volume data .

The principle of volume rendering[41] is shown in figure 7. For each pixel (x, y) in the view plane, a light-ray is cast into the volume and the volume data samples along this ray yield a function of depth $f_{x,y}(z)$. Many techniques for calculating the pixel color $C(f_{x,y})$ have been commonly used (even though C is generally a color with three components, the simple cases below yield a scalar intensity for C):

Direct projections: average projection uses $C(x, y) = \text{mean}_z f_{x,y}(z)$, maximum value projection uses $\max_z f_{x,y}(z)$, minimum projection uses $\min_z f_{x,y}(z)$. An image generated by a maximum projection is similar to an x-ray image: If the ray passes any high-intensity region, the pixel is rendered light.

Opacity mappings: To increase the 3D-feeling obtained by the projection methods, it is common to let bright voxels near the view-plane partially occlude

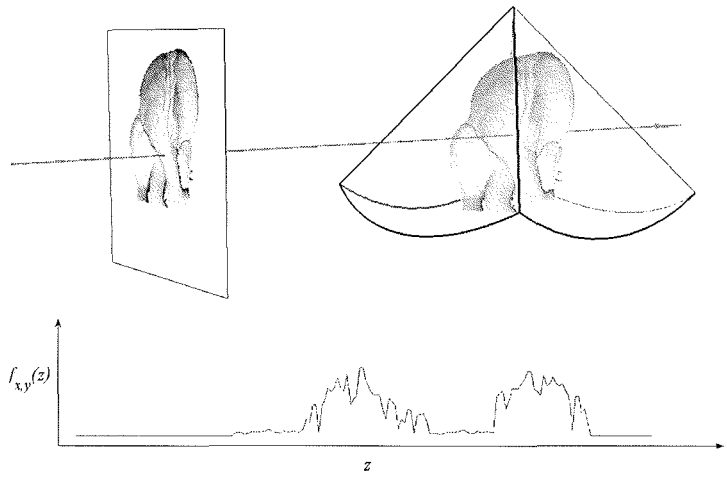

Figure 7: Volume rendering of the myocardium. A light-ray is cast through a pixel (x, y) in the view plane and through the volume, yielding a image sample function $f_{x,y}(z)$ along the beam. (heart model from University of Missouri[72])

other voxels behind. This may be done by adding *opacity*, i.e. a factor α derived from the image samples: $\alpha = \alpha(f_{x,y}(z))$. An opaque sample has a high value of α and corresponds to a brightly rendered location. When using opacity mappings, the intensity may be calculated back-to-front by

$$C^k_{x,y} = C^{k+1}_{x,y}(1 - \alpha_k) + C^k_{x,y}\alpha_k, \tag{2}$$

where k indexes the depth z of the ray cast through pixel (x, y) in the view plane, α_k is the opacity at z_k and $f(z_k) \triangleq f_{x,y}(z_k)$ is the corresponding sequence of image samples. The resulting pixel color is $C(x, y) = C^0_{x,y}$. (In practice, (2) is often calculated front-to-back with a slightly more complicated formula, opening for earlier termination of the recursive calculation.[71])

Gradient shading: In order to get an even better perception of depth (similar to the one obtained with surface rendering), $C(x, y)$ can be calculated as a function of the gradient $\nabla I(x, y, z)$ of the image data at each depth along the ray. Large gradients in a planar region of the volume data will result in pixel values comparable to the ones obtained from a shaded polygon surface. The calculations include defining a light source, and shaded pixel

intensity is scaled with the gradient's component along the light beam: $f_{x,y}(z) = \nabla I(z) \cdot \vec{l}$, with $\vec{l}$ being a unit vector from the light source to the location (x, y, z). Gradient shading normally gives better surface definition than direct projections.

When applied to volumetric ultrasound data, gradient shading usually gives the most satisfactory results. All parts of the volume data tend to have a high level of speckle noise, thus making it difficult to render boundaries of inner organs as well defined surfaces. Authors have described the challenges of presenting 3D ultrasound data in general [53;60], and echocardiographic 3D data in particular [16], as volume renderings. To achieve good surface definitions from ultrasound data, prefiltering is normally required. Depending on the requirements on the computational efficiency, simple filters (such as a Gaussian spatial filter) or more advanced filters (such as an an-isotropic diffusion filter) may be used [60].

1.3 Clinical benefits of 3D echocardiography

Cardiovascular disease is the most frequent cause of death in the western world [76]. Echocardiography has emerged as one of the most important tools for diagnosing and following up patients with various kinds of cardiovascular diseases.

The scope of this thesis is to provide techniques for improved frame rates in 3D echocardiography and fetal echocardiography. Thus, the current and the next sub-sections aim to give a short introduction to the application areas where 3D imaging makes a clinical benefit over 2D imaging.

The most commonly stated motivation for adopting 3D ultrasonic imaging as a clinical tool is the improvement in volume measurements - primarily the volume of the left ventricular (LV) cavity [18]. As the volume can be measured without assumptions on the ventricular shape, a more accurate volume estimate is anticipated. Other important parameters, such as ejection fraction and cardiac output, can then be derived from the measured LV volumes. Other cardiac volumes, such as LV mass, right ventricular and atrial volumes, may be measured accurately from 3D data as well. In addition, morphological investigations of the myocardium can be performed with less restriction than with 2D scans.

Recently, there has been progress towards fully automatic detection of LV shape [47], opening for automatic assessment of important markers as ejection fraction (EF) and cardiac output (CO).

1.4 Imaging the fetal heart

Ultrasonic imaging has had a tremendous impact, not only on cardiovascular investigations of adult and pediatric hearts, but in obstetric medicine as well. As early as 1958, Donald presented images showing body outline and scull outline of

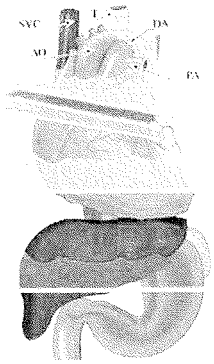

Figure 8: Cardiac views from the fetal heart, suggested for echocardiographic screening by Yagel et al.[75].

fetuses *in-vivo*[21], and the first obstetrical measurements obtained from ultrasonic imaging was the size of the fetal head. Since that, the use of ultrasonography in obstetrics has accelerated, and today ultrasound imaging is an inevitable part of prenatal care.

Congenital heart disease (CHD) is the most frequent pathology in live-births, with an prevalence rate of 8.1/1000, and prenatal detection is reported to reduce the mortality of neonatals with CHD[14]. Echo examination of the fetal heart is the main tool for detecting CHD in fetuses. This is one of the motivations behind the first-trimester ultrasonographic screening of the entire population of pregnant women done in Norway, as well as in some other countries[64].

The basic examination of the fetal heart is traditionally done with B-mode ultrasonic scan. One or several cardiac views may be examined - the most important one being the four chamber view[3;63], but other views may be investigated as well[75], see figure 8. However, the traditional B-mode examination method has shortcomings: Obtaining the volume from just one or a few two-dimensional image slices intersecting the myocardium is inaccurate and depends on assumption of a regular shape[17]. Furthermore, the acoustic access to the various cardiac views may be limited and the resulting images and measurements depend on the operator's skill[62].

Acquisition of volumetric data in the place of, or in addition to, the standard B-mode views has important potential advantages:

- Cardiovascular malformations are possible to visualize from all angles, opening for a better assessment of CHD[2].

- If a satisfactory volumetric cine-loop is acquired, a complete off-line cardiac examination is possible[15;45].
- Missing or misaligned views may be generated off-line, which can be valuable in second opinion.
- The data acquisition could become less dependent on operator's skill.

Existing options for 3D fetal echocardiography are mainly *i)* 3D reconstruction from B-mode scans spanning several cardiac cycles and *ii)* real-time 3D ultrasound scanners.

Regarding *i)*, the most popular technique is probably STIC (spatio-temporal image correlation). In this method, several B-mode cine-loops are captured while the scan-plane is being swept over the myocardium with a stepper motor. The resulting 3D cine-loop is reconstructed by cardiac gating following from a spatio-temporal analysis.[27] The gating process is performed and the data displayed immediately after the data acquisition is completed. The STIC algorithm is not only capable of reconstructing 4D gray-scale data, but can also reconstruct 2D color Doppler data into a 4D map of the blood flow in the heart and vessels.

Regarding *ii)*, real-time 3D ultrasound systems designed for transthoracic scanning of adult subjects have also been applied to fetal cardiac imaging[2;57]. However, even though the acquisition process is simple and fast, the resulting 4D data has inferior spatial and temporal resolution compared to STIC.

2 Temporal resolution

As the speed of sound in soft human tissue is about 1540 m/s and a full ventricular scan with good image quality may consist of as much as 4000 beams, the propagation distance for one single volume adds up to 1000 m when scanning without parallel beam processing at 12.5 cm depth (4000 pulses travels 0.25 m back and fourth). Thus, in this scenario only 1.5 volumes per second of data would be acquired each second. However, a far higher volume rate is needed for cardiac scanning.

Three approaches to increasing the volume rate to an acceptable level are discussed in this section. Practical solutions can utilize one or more of the techniques in 2.1 - 2.3.

2.1 Parallel beam processing

The principle of parallel beam processing was introduced in 1984[56], and a real-time 3D ultrasound system with eight parallel channels was demonstrated in 1991[51]. When applying this technique, one wide ultrasound beam is transmitted

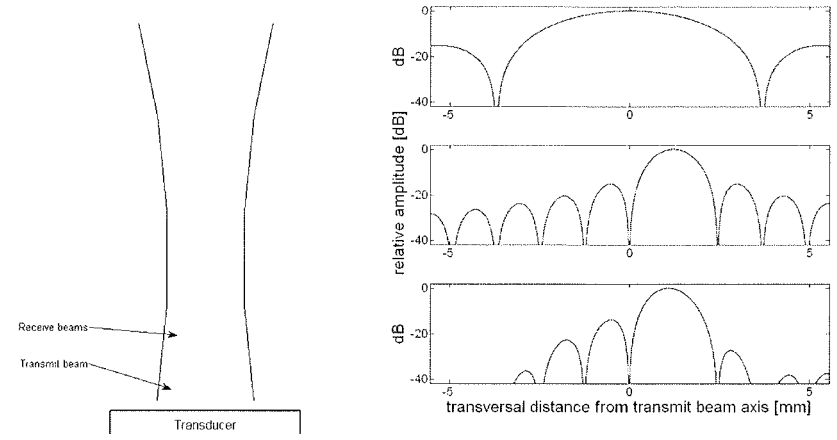

Figure 9: The principle of parallel beam processing: Left: A wide beam is transmitted, while several independent beam forming channels process receive beams simultaneously. Right: The transmit beam (top) and the receive beam (middle) have slightly different directions, thus giving an asymmetric two-way beam profile (bottom).

and several more sharply focused receive beams are created simultaneously by parallel beam processing channels in the scanner. The receive beams are steered in slightly different directions, thus picking up reflected echoes from different parts of the transmitted beam, see figure 9.

If the transmit beam is narrow (just wide enough to cover the receive-beams), the two-way beam profile will be asymmetric, which results in a non-uniform PSF and possible image artifacts[11].

The beam profile for the two-way propagation is the product of the transmit beam profile and the receive beam profile. If the transmit beam profile is very wide (i.e, there is a small degree of transmit focus), the profiles of the receive beams would be almost identical, ensuring uniform PSF. However, the lack of focusing makes the echoes weaker and thus gives a higher noise level.

To increase the acquisition rate from 1.5 volumes per seconds to a level comparable to common frame rates in B-mode imaging, one would need a large number of parallel beams (e.g. 20, 30, or even more, compared to the eight channels implemented by Smith et al.[58]) and consequently extensive hard-ware processing capabilities would be required. In addition, the transmitted beams would have to be wide: 60 volumes per second would imply 40 transmitted beams per volume scan, thus a 60×60 degrees pyramidal scan would require transmit beams

covering a 10×10 degrees sub-pyramid. To maintain a sufficiently strong receive-signal of such a wide beam, the transmitted power would have to be increased, but a power increase is problematic as a wide beam has the maximal acoustic intensity close to or at the transducer surface. Consequently, it would be very challenging to irradiate the full LV at a high frame rate without raising the probe temperature above the regulatory limit of 42°C.

All in all, even if one could apply an arbitrary number of parallel beams, the spatial and temporal resolution of B-mode imaging could hardly be matched for a full cardiac scan. Therefore alternative techniques for improvement of acquisition rate and perceived image quality are interesting to investigate, and possibly apply, in future ultrasound systems.

Synthetic transmit aperture

The data acquisition methods described in section 1.1 rely on a focused ultrasound wave field denoted a *beam*. Since there only is time for one transmitted beam in each direction in high frame-rate applications like cardiac imaging, there must be one particular focus depth applied to each transmit beam and, consequently, parts of the image are out of focus. Synthetic transmit aperture (STA) is a different approach to image formation without this limitation.

An STA image is formed by emitting a spherical wave from one array element at the time, and recording the echoes on all the elements [50]. When all pair-wise transmit-receive responses have been recorded, both the transmit beam and the receive beam can be focused in any imaging point, thus resulting in two-way focus in all image locations. However, STA image forming has two limitations currently making it impractical to use in cardiac imaging: *i)* The amount of data is very large and *ii)* target motion during the pulse transmissions from all channels degrades the image.

2.2 ECG-gated 3D imaging

Already in 1956, shortly after the invention of two-dimensional ultrasonic imaging, the principle of 3D imaging was described and rudimentary images were demonstrated on an oscilloscope [32]. Later, a mechanical position recorder was combined with B-mode imaging to produce cross-sectional images of the heart, with unconstrained positions of the cross-sections [19;25].

An early commercial provider of equipment and soft-ware for 4D echocardiographic data reconstruction was Tomtec Imaging Systems GmbH, Germany [48;69]. Data were acquired by a trans-esophagus probe with a phased array transducer, mounted through a stiff tube. During data acquisition, the probe was pulled back in the tube and thereby scanning a 3D region over several heart cycles. The

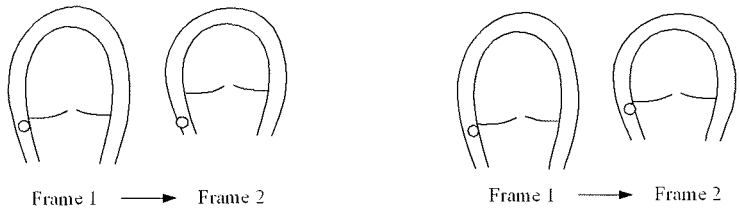

Figure 10: Two ways to temporally interpolate between successive image frames: left: interpolation at a fixed *spatial* location (i.e., in Euler coordinates), right: interpolation at a fixed *anatomical* location (i.e., in Lagrange coordinates).

two-dimensional images were captured as video frames and aligned in time and space off-line, thus forming a 4D data set.

There have been several improvements of the methods for ECG-gated 3DE. Stepper motors have been used to make tilted transthoracic scans[20], magnetic location registration has been utilized to reconstruct B-mode images into volumetric data sets[24], and also to create dynamic 3D scan line data from B-mode scan lines[9].

The advent of matrix transducers has made a new method for cardiac gating possible: Since the beam can be steered freely in space, the total scanning volume can be subdivided into smaller volumes scanned in separate cardiac cycles. This form of gating can be called volume stitching and is investigated in papers B and D.

2.3 Morphing

When an image stream with low frame rate is displayed without any temporal interpolation, moving targets tend to have a staggering look. Plain temporal interpolation of image data

$$\xi_{ij}(t) = (1 - \alpha)\xi_{ij}(t_0) + \alpha\xi_{ij}(t_1) \tag{3}$$

makes the motion look more smooth, but at the cost of lost detail. This is an example of a *morphing* (a smooth, continuous transition from one image into another one[70]), but other morphing algorithms exist as well. If, for each point $\mathbf{r}_{ab}$ in the frame at time t_0, a point $\mathbf{r}_{cd}$ in the frame at time t_1 could be found that showed the same anatomical location, the calculation (3) could be generalized (as

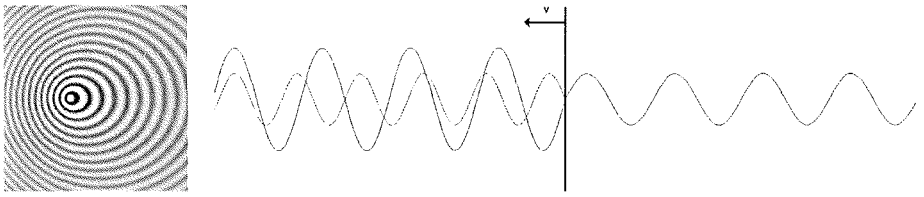

Figure 11: The Doppler effect. Left: a moving point source[73]; right: a moving partial reflector.

shown in figure 10):

$$\xi_{ij}(t) = (1-\alpha)\xi_{ab}(t_0) + \alpha\xi_{cd}(t_1), \tag{4}$$

For given i and j, the indices a, b, c and d need to be decided. This principle is addressed in paper A, where pulse-echo velocity measurements are utilized to estimate the locations $\mathbf{r}_{ab}$ and $\mathbf{r}_{cd}$ in cardiac ultrasound images.

3 Velocity estimation

Ultrasound backscatter imaging can, in addition to utilize backscattered amplitude to form gray-scale images, also be used to measure velocities in tissue or blood, as initially proposed in 1957[54] and with numerous later refinements. In this thesis, velocity data obtained by pulsed ultrasound are used for two different purposes: *i)* as input to an algorithm for image morphing (paper A) and *ii)* as input to an algorithm for automatic detection of a gating signal for the fetal heart (papers C and D).

Two different principles are commonly used for velocity measurements by ultrasound: Doppler measurements and speckle tracking (Paper A utilizes both techniques, while papers C and D only utilize Doppler measurements). The basic theory for both principles is presented in this section.

3.1 The Doppler effect

When a moving object emits or reflects sound, the motion of the object causes a frequency shift of the emitted/reflected sound waves, see figure 11. This phenomenon was discovered by Christian Doppler in 1842 and is called the Doppler effect. The frequency shift Δf for a continuous wave propagating with velocity c and reflected by an object with constant velocity v in the propagation direction

is given by the Doppler equation

$$\Delta f = -f_0 \frac{2v}{c}, \tag{5}$$

where f_0 is the frequency before reflection and $f_0 + \Delta f$ is the frequency after reflection.

In soft human tissue, the propagation velocity is commonly assumed to be $c = 1540$ m/s, while the velocity of the scatterer is in range $v \sim 0.1 - 1$ m/s. Thus, the relative frequency shift is very small, less than 0.1%, and is difficult to measure accurately. Two different approaches have been widely used for Doppler measurements:

- Continuous wave (CW) Doppler, a technique where a continuous, sinusoidal wave is transmitted. The Doppler shift in the reflected signal then has contributions from reflections in all locations along the beam. With a transmit frequency of 3 MHz (typical for cardiac imaging) and a blood velocity of 1 m/s, the frequency shift fall in the range of kHz and is audible to the human ear.

- Pulsed wave (PW) Doppler, where short pulses with wider frequency range are emitted. If the spectrum of the transmitted and received pulse were possible to measure accurately, the velocity of the reflector could have been calculated from one single pulse by substituting center frequencies f_0 and Δf into (5). However, since *i)* the frequency shift is tiny compared with the bandwidth of the pulse, *ii)* the accuracy of both pulse transmission and receive signal sampling is limited and *iii)* there generally are several contributions to the frequency shift of the received signal, originating from scatterers with different velocities, this simple approach is not feasible. Therefore, PW Doppler measurements use several pulse firings, with a constant pulse repetition frequency, in each beam direction, and the back-scattered signals are sampled and analyzed. The registered echoes corresponding to a specific spatial location are modeled as samples from a complex Gaussian process $z(t)$ at times $t_1, \cdots, t_N$[4]. Each sample $z(t_i)$ is the complex envelope of the reflected signal in the observed range, thus representing the amplitude (by $|z|$) and phase (by $\arg(z)$) of the reflected pulse. The properties of the process $z(t)$ are, if the process is stationary, completely characterized by either the autocorrelation function $R(\tau)$, or, equivalently, by the power spectrum $G(\omega) = \mathcal{F}(R(\tau))$, where by definition $R(\tau) \triangleq E(z(t+\tau)z(t)^*)$.[4]

3.2 Autocorrelation

The autocorrelation technique for measuring the Doppler shift in PW Doppler was first introduced for pulsed RADAR imaging[77] and later applied to ultrasonic

Doppler spectrograms and 2D Doppler blood flow imaging [5;34].

If $z(t_k)$ is a discrete stationary process, the autocorrelation $R(m)$ between two samples at times t_k and t_{k+m} depends only on the lag m [6], and a commonly used estimator for $R(m)$ based on the observations $\{z(t_i)\}$ is

$$R_N(m) = \frac{1}{N} \sum_{k=1}^{N-m} z(t_{k+m}) z^*(t_k). \tag{6}$$

From $R_N(0)$ and $R_N(1)$, the following characteristics of the spectrum of the Doppler shift may be derived [37]:

Power The mean reflected signal power is estimated by $R_N(0)$. A high value of $R_N(0)$ indicates a strong echo.

Angular velocity The mean angular velocity is estimated by

$$\omega_N = \arg R_N(1). \tag{7}$$

The scatterers' mean velocity v_N along the beam direction follows from (7) by inserting $\Delta f = \omega_N / 2\pi$ into (5):

$$v_N = c \frac{\omega_N}{4\pi \cdot f_0}. \tag{8}$$

Note that $\omega_N \Delta t$ resides in the interval $(-\pi, \pi]$, implying that a velocity with high magnitude will be folded into the interval $\frac{c}{2\pi f_0 \Delta t}(-1, 1]$, an effect called *aliasing*.

Spectrum spread The bandwidth of the angular velocity is estimated by

$$B_N = \sqrt{2\left(1 - \frac{|R_N(1)|}{R_N(0)}\right)}. \tag{9}$$

The first application of the pulsed Doppler technique in ultrasonic imaging was to measure the blood velocities and present them as Doppler spectrograms. When measuring blood velocities, there are generally several contributors to the velocity estimate of the reflected pulse: a variety of blood cells (which may have different velocity, in particular if the velocity field is turbulent) and reflections from surrounding tissue structures (reverberations, side lobes), give echo with varying Doppler shift. The estimate ω_N is a combination of all these echoes and the resulting spectrum is therefore wider than that of a single reflector echo. Since tissue cells scatter the pulse with considerably higher amplitude than blood

cells do, ω_N will often severely under-estimate the true blood velocity. The low-frequency part of the Doppler shift is called clutter, and several well-performing methods for clutter rejection have been described [10;42].

The Doppler autocorrelation technique has been utilized not only for blood velocity estimation: Local measurements of the myocardial velocity (i.e., tissue Doppler imaging, TDI) is possible to perform as well [43]. Since the mid 1990s this imaging mode has been present in commercial ultrasound scanners, and other imaging modes derived from TDI, such as strain rate imaging, strain imaging and displacement imaging, have been introduced as well [29].

Doppler imaging is a computationally cheap technique and real-time Doppler imaging has been common for over two decades. There are, however, limitations: Firstly, only one component of a 3D vector is measured. If this fact is not well understood by the sonographer, invalid interpretations may result from examinations involving Doppler imaging. Secondly, aliasing is a concern when configuring the imaging system. Using a too low Nyquist limit implies incorrect measurements of velocities with high magnitudes, whereas a too high Nyqvuist limit reduces the accuracy of the Doppler shift estimates and hence degrades the image quality.

3.3 Speckle tracking

The fine-grained pattern found in ultrasound images originates from interference of back-scattered signals from different scatterers, and this pattern is relatively constant from frame to frame in the image sequence. A different approach to velocity estimation is to track the speckle pattern in two- or three-dimensional image data from frame to frame, a technique called speckle tracking.

Consider two successive frames $X_0 \triangleq X(t_0)$ and $X_1 \triangleq X(t_1)$ in a stream of image frames and a position $\mathbf{r}$ in the image X_0. The objective of the speckle tracking technique is to find the position $\mathbf{r}'$ in X_1 showing the same anatomical location as $\mathbf{r}$ in X_0, see figure 12. This is done by an exhaustive search, within a search region S, after the point where the neighborhood image $K(\mathbf{r}, X_0)$ contents surrounding $\mathbf{r}$ in X_0 is most «similar» to the corresponding $K(\mathbf{r}', X_1)$:

$$\mathbf{r}' = \text{argmin}_{\bar{\mathbf{r}} \in S(\mathbf{r})} d\left(K(\mathbf{r}, X_0), K(\bar{\mathbf{r}}, X_1)\right). \tag{10}$$

The metric d quantifies the distance between kernel images and may be of different kinds, as described below. From (10) we readily get the estimate $\hat{\mathbf{v}}$ for the velocity vector in $\mathbf{r}$ at time t_0:

$$\hat{\mathbf{v}}(\mathbf{r}, X, t_0, t_1) = \frac{\mathbf{r}' - \mathbf{r}}{t_1 - t_0} \tag{11}$$

The principle described above applies to both 2D and 3D image sequences. The technique was initially proposed in the early 1970s [8] (named «a class of

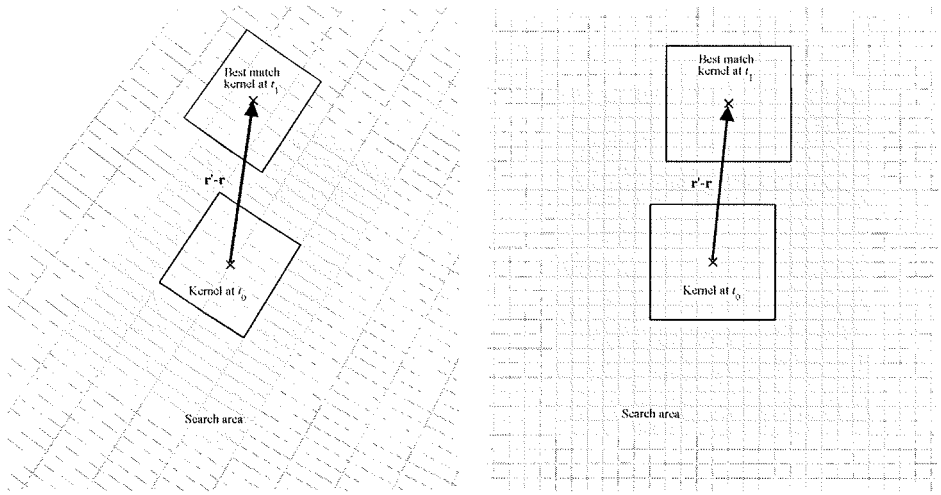

Figure 12: 2D velocity vector estimation by speckle tracking. Left: tracking the speckle pattern directly in the beam data of a sector scan; right: tracking the pattern in data sampled on a Cartesian grid (i.e. scan-converted data).

algorithms for translational image registration»). The first applications in ultrasonic imaging were described a decade later, both utilized for optimal image compounding[65] and for 2D blood velocity vector estimation[66].

There are various aspects to consider when implementing the velocity estimator (11):

Kernel metric Different criteria for kernel matching have been evaluated[38], including the sum of square differences, the sum of absolute differences (SAD) and correlation coefficient. SAD is commonly used due to simpler computations.

Image representation The image data undergo a number of processing steps during imaging, and several of the intermediate representation forms may be used for the speckle tracking search: RF cross correlation, beam space amplitude data, scan converted amplitude data, gray-scale pixel values. Figure 12 shows the different setup of beam data tracking and Cartesian data tracking. In paper A we utilized a SAD algorithm performed on upsampled beam data.

Kernel size The size of the kernel impacts not only the computation time, but the estimator accuracy as well: If the kernel is too small, the SNR of the

cost function will be higher than necessary, implying a high SNR also for the tracking result. A too large kernel size will, if the motion is non-uniform, include locations with different velocity in the matching and may thus give incorrect results.

Search area The search area must be large enough to cover the maximal displacement $|\mathbf{r}'-\mathbf{r}|$ anticipated for the motion of the target in the time from t_0 to t_1. On the other hand, a too large search area causes slower computation of the velocity estimate and, if the image noise or the image decorrelation is large, it is more likely to find the minimum of (10) in an incorrect location. The lower the frame rate/volume rate, the larger the search area needs to be.

Spatial resolution of the image: The spatial resolution of the velocity estimate depends on the resolution of the image itself. The displacement estimate (10) can in good cases have one pixel or better accuracy [52;59]. However, since a neighborhood of the considered location $\mathbf{r}$ is used in the SAD calculation, the estimate has inherent spatial averaging and, consequently, the resolution of the velocity field estimate corresponding to independent sampling will generally have lower resolution than the image. Note also that the spatial sampling rate of the image data should preferably not be lower than the rate corresponding resolution given by the PSF (if not, the pattern of a given anatomical location in frame X_0 might look differently from the pattern in frame X_1, leading to an increased minimal cost and greater possibilities for «untrue» local minima).

Image decorrelation A reliable displacement estimate needs a high local correlation between the neighborhoods of a given anatomical location in successive image frames. The main factors decreasing the said correlation are: *i)* substantial deformations over distances smaller than the kernel size, *ii)* target rotation, *iii)* ultrasound imaging system is not completely translational and rotational invariant, *iv)* thermal noise in the image and finally, specifically for 2D image data, *v)* target motion out of the image plane.

Temporal resolution A high temporal resolution of the image data results in small maximal displacement and thus a small search area. In addition, there will be less decorrelation between successive images, resulting in a lower minimum value in (10) and thus a more accurate velocity estimate. On the other hand, if the temporal resolution is high and the motion small (e.g., lateral motion less than one beam width), sub sample estimation errors may occur.

Signal to noise ratio (SNR) An image with a high level of thermal noise (low SNR) will exhibit decorrelation between successive images and a relatively

high minimum value in (10). Consequently, decreasing SNR yields reduced accuracy of the velocity estimate. A way to improve the the SNR for the SAD calculation is to restrict velocity estimation to points with a strong echo (a technique often referred to as feature tracking[40]).

Image artifacts Artifacts such as static reverberations may give rise to incorrect local minima of (10) and can therefore degrade the estimator accuracy.

Computational efficiency The Doppler autocorrelation in (6) is very effective - $\mathcal{O}(N_{pulses})$ where $N_{pulses} \lesssim 5$ is the number of pulse firings in each beam direction. Clutter rejection may come in addition. Speckle tracking has algorithmic complexity $\mathcal{O}(N_{search}N_{kernel})$, where N_{search} is the number of image samples in the 2D search area/3D search volume, and N_{kernel} is the number of image samples in the kernel matching area/volume. Moderate values in practical searches are $N_{search} \sim 100$ / $N_{kernel} \sim 25$ for 2D tracking and (suggestively) $N_{search} \sim 1000$ / $N_{kernel} \sim 100$ for 3D tracking. Both Doppler estimates and speckle tracking estimates normally utilize spatial averaging after the local estimation.

4 Summary of papers

This thesis describes techniques that may provide increased temporal and spatial resolution when ultrasound systems capture or present volumetric echocardiographic data sets. Each of the four papers that constitute the thesis are self-contained, and they are presented exactly as published.

Two different techniques have been investigated: temporal morphing (paper A) and gated acquisition with stitching (papers B to D).

In a real-time volumetric scan of the full LV, the data acquisition rate can become very low - maybe as low as 10 volumes/s if a high spatial resolution is required. Temporal morphing, i.e. smooth, continuous transitions between successive frames, is a technique to improve the presentation of data with low acquisition rate. Paper A shows how velocity data, either obtained from the image data by speckle tracking or acquired in an extra tissue Doppler data stream, can be utilized for calculation of morphed image data with any frame rate. The technique applies to both two-dimensional and three-dimensional data. The algorithm was tested on temporally decimated B-mode data, thus morphed B-mode images were created and compared qualitatively and quantitatively to the original images. Four different velocity field estimates were evaluated: two local velocity field estimates and two estimates comprising a model fit and a global velocity estimate. One of the model based estimates, the *myocardium field estimate,* was the one yielding the best image quality of morphed images.

A novel estimator for tissue velocity vectors was introduced: Doppler aided speckle tracking (DAST). The estimated 2D or 3D velocity vector was obtained by combining a Doppler autocorrelation estimate along the beam with a speckle tracking estimate transverse to the beam. The DAST velocity estimates were utilized in the morphing calculations.

A test of the diagnostic value of the morphed images was performed. A blinded wall motion scoring test was conducted using data from 20 patients picked randomly from a large data base. Pathological classification of myocardial segments was performed twice (based on original B-mode cine-loops and on decimated and morphed cine-loops). The test showed a relatively good match between the results in the two cases, even though the morphed cine-loops had frame rates as low as 12-18 fr/s.

Original contributions from paper A: Introduction of the DAST estimator for velocity estimation. Description and implementation of image morphing, i.e temporal interpolation in Lagrange coordinates, utilizing DAST velocity estimation in B-mode ultrasound images.

Paper B demonstrates multicycle stitching of ultrasound data in real time. A computer program for real-time stitching was implemented, running integrated with the scanner control software on a Vivid 7 ultrasound scanner. The concept of geometrical distortion due to tissue motion was formalized and a quantitative measure for the distortion was proposed. By simulating 3D ultrasound scans in a kinematic model of the left ventricle, the reduction of distortion obtained by multicycle stitching was quantified: For a typical, fixed scan setup of a full LV scan, the peak distortion was reduced from 9 mm for an unstitched scan to below 2 mm for a stitched scan acquired over 6 or 8 cardiac cycles (utilizing a constant heart rate of 59 beats/min and identical scan setups for the stitched and the unstitched scans).

A clinical test was performed, where two kinds of stitched volume acquisition were compared: Stitching with real-time display and post-processed stitching. Even though the operator found the real-time display useful for better control of stitching artifacts, neither reduced examination time nor increased quality of the stitched data sets was found for the real-time method compared with the post-processed method.

Original contributions from paper B: Real-time stitching and presentation of volumetric ultrasound data from several consecutive cardiac cycles was described and implemented. The concept of geometrical distortion was formalized, and the amount of distortion was quantified through simulations based on a kinematic model of the left ventricle.

Paper C introduces a novel technique for synchronization of ultrasound data: Tissue Doppler gating (TDOG). Due to lack of an ECG signal for gating, 3D ultrasound images of the fetal heart have traditionally been cumbersome to reconstruct. Even though the existsing spatio-temporal image correlation (STIC) technique is commercially available, it only provides 3D reconstruction as a post-processing step. When using TDOG gating, extra frames with two-dimensional tissue Doppler data were acquired together with the B-mode frames, and the

Doppler data were transformed to a synchronization signal (the TDOG signal). To test the technique, data were acquired from eight different fetuses with gestational age from 20-24 weeks. A manual sweep was performed in each recording, ensuring that the recorded B-mode sequence covered the entire fetal heart. Spatially averaged tissue Doppler signals were calculated and the resulting TDOG trace was shown to exhibit strong peaks caused by the rapid relaxation of the myocardium. The time points of the peaks were detected and used to create gated, four-dimensional (three spatial dimensions and time) data sets covering the entire fetal heart. Successful visualizations were obtained for four of the fetuses, and 2D cine-loops from the eight standard views of the fetal heart were successfully extracted from one single 4D data block.

Original contributions in paper C: Description and implementation of TDOG as a new technique for cardiac gating. Successful application of TDOG in fetal echocardiography, example images presented.

To test how TDOG could perform as a clinical tool, a prototype with real-time TDOG signal processing was implemented. In paper D it is demonstrated that a TDOG signal can be calculated in real-time, and that it is feasible to use the TDOG signal as a replacement for ECG when doing stitched, volumetric scanning of the fetal heart. Thus, the techniques of paper C and paper B were combined, and the TDOG technique provided instant visualization of the three-dimensional fetal heart scans at 60 volumes per second. However, the utilized probe had too low resolution for high-quality fetal heart imaging, and the image quality obtained was not sufficient for clinical use. If a matrix probe optimized for resolution at 5-8 cm depth becomes available, the method may provide the best known gating technique in the future.

Original contributions in paper D: A prototype real-time implementation of the the tissue Doppler gating technique was made. In-vivo *fetal cardiac data were acquired acquired and presented.*

5 Discussion

The ultimate goal when constructing 3D echocadiographic systems is to provide both high spatial resolution and high temporal resolution in real time, with an acquisition volume large enough to cover the full left ventricle (LV). Implementing a high degree of parallel beam processing is a good step towards this goal, but it is unrealistic to achieve both high frame rates and full cardiac coverage by parallel processing alone (see section 2.1). As transducer technology continues to progress, it is likely that the spatial resolution will improve due to increased number of elements and support for higher frequencies, and consequently more beams are required to cover the LV in one scan. Therefore, to be able to acquire and present 3D data at both high spatial and high temporal resolution in the future, the techniques presented in this thesis will still be relevant.

The morphing technique in paper A was shown to reduce image smoothing artifacts due to temporal up-sampling for ultrasonic images with low frame rate (10-20 frames/s). Image morphing relies on a velocity field estimate for the imaged region in each frame, with the extra condition that the integrated velocity of the whole cardiac cycle should vanish. In paper A a simple scheme for drift compensation was used (A.18), distributing the error accumulated over the cardiac cycle evenly on all frame-to-frame estimators. This approach has a disadvantage: if a large error occurs in a position in one frame while the other frames has accurate velocity estimators at that point, this single estimation error degrades the compensated velocity estimator (and thus the morphed images) in the whole cycle. Several different approaches to error corrections exist and should be considered when refining the morphing implementation presented in paper A:

- Two-way tracking: If each frame-to-frame displacement was tracked both fowards and backwards in time, the mean of the two displacement vectors could have given a more reliable result than just using one of them. Also, a large difference between these two vectors would have indicated inaccurate tracking.
- One could use dynamic programming for finding the most plausible distribution of the error term in (A.18) among the frames. In frames with a low correlation coefficient between the best match kernels, a large drift compensation could be allowed.
- Spatial processing for selection of the statistically «best» estimate in a region (e.g. the mean of the vector estimates in the regian, the median of each component the vector estimates or a least square error estimate).
- Feature tracking, i.e. restricting start points for the displacement search to locations with a strong echo[40].

In paper A, we found that the two model-based velocity field estimates performed far better than the purely local ones when utilized for image morphing. However, the extra step with model extraction implies an additional risk, since the model may not be correctly fitted to the data. If a model used for image morphing is unable to handle motion patterns present in a pathological case, then the morphed data would show artifacts in the pathological region and therefore not be very helpful for the sonographer.

However, even with this potential drawback, the wall motion scoring evaluation showed that the morphed images were still carrying most of the information needed for classification of the myocardial segments.

As seen in paper A, the morphings with the best image quality utilized semi-automatic model fitting when calculating the *myocardum field estimate* for the

velocity field. In a clinical setting, the need for manual assistance would be a major drawback of the method. For a method involving model fitting to be practically usable, it should utilize a fully automatic LV shape detection with both radial and lateral displacement estimates. Hence, combining deformable contour tracking, e.g. as described by Orderud[47], with a 3D-implementation of the morphing algorithm in paper A, could provide a practical way of image quality improvement for low volume-rate 3D data.

The other approach to increase temporal resolution, presented in papers B and D of this thesis, utilized cardiac gating of a 3D volume partitioned into a fixed number of sub-volumes. The assembled volumes were merged and volume rendered in real-time, thus providing immediate display of cardiac 3D data with e.g. four times higher temporal resolution than was possible without gating. Even though progress is made by the ultrasound imaging industry towards fully usable real-time 3D scanners for cardiac examination, there will still be circumstances where gating as presented in papers B will significantly improve the results:

- Second harmonic imaging is more challenging for massive parallel beam processing, since the mechanical index (MI) needs to be higher than in fundamental frequency imaging. Transmitting wide beams with high power easily overheats the probe surface. In a gated scan, one could use a narrower transmit beam and still cover the full LV.
- When acquiring 3D color Doppler data or 3D tissue Doppler data, the acquisition rate demand is even tougher than for 3D gray-scale images. Thus, the volume stitching principle will continue to be useful for 4D hemodynamic analysis of the cardiac cavities, and for 4D analysis of myocardial tissue viability.
- For a detailed 3D morphological study of the valve motion one would need a particular high temporal resolution, since some of the valve motion exhibit high velocity and high acceleration.

However, it can be very difficult to apply the stitching technique on some patients. The two main problem areas being heart rate variations and respirational motion. For patients with constantly varying heart cycle length, there will frequently be no acquired subvolumes that can be well aligned, giving stripe artifacts in the images due to the misalignment. Likewise, if the general condition of the patient is so weak that breath-hold is not possible, the probe often gets displaced relative to the myocardium due the respirational motion of the chest. This gives misaligned subvolumes, too. The main rationale for the real-time stitching mode presented in paper B was to eliminate stripe artefacts by letting the sonographer monitor the stitching quality during acquisition. Disappointingly, no significant stitching quality improvement could be proved by the conducted clinical test.

Paper C and D outline a technique for data acquisition of 3D fetal heart data corresponding to the one for transthoracic imaging introduced in paper B. As was shown in paper C, a successful TDOG recording could provide a 4D data block from which 2D cine-loops of all classical views of the fetal heart were extracted. However, as the TDOG gating signal was derived from Doppler shifts, only motion along the beam was intercepted and the method did not work well for subcostal insonation (only 2 of 5 fetuses presented in paper D had an adequate gating signal). A combination of the TDOG signal with image based analysis, e.g. spatiotemporal image correlation (STIC), could potentially provide robust real-time gating, even when only subcostal insonation is possible.

In fetal cardiac imaging, the scan angle is smaller ($\approx 30°$) than in transthoracic imaging ($\approx 65°$), thus the availible cardiac matrix probes can be set up to yield a higher temporal resolution for fetal heart applications than for adult hearts. However, fetal heart imaging is demanding both regarding spatial resolution, due to small size, and temporal resolution, due to high heart rate. A dedicated matrix transducer for transabdominal imaging of the fetal heart should therefore have larger aperture and higher frequency, thereby effectively increasing the spatial resolution.

How would an ideal transducer for fetal heart imaging be? The challenges are substatial when designing a probe with sufficient element count and a beam forming system with high enough processing capacity: Since the scan angle need not exceed 30°, an element pitch of λ would be sufficient. If the aperture was increased from the current $\approx$ 15 mm to 20mm in a square transducer, and the frequency was increased to 5 MHz transmit 10 MHz receive, we would get a wave length of $\lambda = 0.15$ mm, an element count of more than 17000. At 5 cm depth, the beam with would be $f_{\#}\lambda \approx 0.4$ mm, thus 68 beams would be needed in each scan direction and over 4500 beams required for a full volume scan. The propagation time for one single pulse at 8cm scan depth would be about 0.5 s, and 50 parallel beam processing channels would give a temporal resolution of 100 fr/s (which typically gives 40 frames per cardiac cycle). The massive parallel processing would require wide transmit beams, giving a relatively high side lobe level and consequently a low SNR. Such an imaging system might become available in the future, but does not seem realistic for the time being.

Even a real-time system with a 3D image quality comparable to the one demonstrated in paper C, where a receive frequency of 5 MHz was utilized for a gated recording with $\sim$ 100 frames/s, would be very challenging to construct. A matrix transducer similar to the 3V probe utilized in paper D, but with higher frequency to increase spatial resolution, would need a form of gated acquisition to match the frame rate at a full cardiac scan. Such a high quality imaging system may be realizable in a shorter time frame, and the technique of paper D should be of high relevance for a high frame rate set-up.

6 Conclusion

The challenges of achieving high frame rate in 3D ultrasound imaging, imposed by the restrictions given by the speed of sound, make special techniques for boosting the frame rate relevant also in the future. The two approaches investigated in this thesis, morphing and sub-volume stitching, are practical solutions to this challenge and are potential building blocks of commercial ultrasound systems.

The morphing technique, though having limitations due to noisy velocity field estimates, provides means for increasing the display update rate in data streams with as low acquisition rate as 10-15 frames/s. For example, 3D tissue Doppler imaging is an imaging modality where high frame rate simulation through morphing has a potential benefit.

The stitching technique is already present in some commercial products, but might lose relevance as processing hardware for parallel beams improves. However, when maximal temporal and spatial resolution is desired, cardiac gating will probably continue to play a role, and one might anticipate that the real-time, stitched scanning mode will be present in future systems as well. In particular in fetal cardiac imaging, when the heart rate is high and a high spatial resolution is needed, robust and automatic means for image stitching can become valuable. When dedicated matrix probes for high-resolution 3D fetal imaging become available, the real-time TDOG technique will give an opportunity for optimizing both spatial and temporal resolution.

References

1. Trans-oesophageal echocardiography - transverse views, 2007. URL `http://www.anaesthetist.com/icu/organs/heart/tee/xverse.htm`. [Online; accessed 21-March-2007].

2. P. Acar, Y. Dulac, A. Taktak, and S. Abadir. Real-time three-dimensional fetal echocardiography using matrix probe. *Prenat Diagn*, 25(5):370–375, May 2005.

3. L. D. Allan, D. C. Crawford, S. K. Chita, and M. J. Tynan. Prenatal screening for congenital heart disease. *Br Med J (Clin Res Ed)*, 292(6537): 1717–1719, Jun 28 1986.

4. B. A. J. Angelsen. *Waves, signals and signal processing in medical ultrasonics*, volume I. Dept. of Physiology and Biomediacl Engineering, Norwegian University of Science and Technology, Trondheim, Norway, 1995.

5. B. J. A. Angelsen. Instantaneous frequency, mean frequency and variance of mean frequency estimators for ultrasonic blood velocity Doppler signals. *IEEE Trans Biomed Eng*, 28(11):733–741, Nov 1981.

6. B. A. J. Anglesen. A theoretical study of the scattering of ultrasound from blood. *IEEE Trans Biomed Eng*, 27(1):61–67, February 1980.

7. A. Austeng and S. Holm. Sparse 2-D arrays for 3-D phased array imaging–design methods. *IEEE Trans Ultrason Ferroelectr Freq Control*, 49(8): 1073–1086, Aug 2002.

8. D. Barnea and H. Silverman. A class of algorithms for fast digital image registration. *IEEE Trans Comput*, 21:179–186, 1972.

9. S. Berg, H. Torp, D. Martens, E. Steen, S. Samstad, I. Høyvik, and B. Olstad. Dynamic three-dimensional freehand echocardiography using raw digital ultrasound data. *Ultrasound Med Biol*, 25(5):745–53, Jun 1999.

10. S. Bjærum, H. Torp, and K. Kristoffersen. Clutter filter design for ultrasound color flow imaging. *IEEE Trans Ultrason Ferroelectr Freq Control*, 49(2):204–216, Feb 2002.

11. T. Bjåstad, S. A. Aase, and H. Torp. The impact of abberation on high frame rate cardiac b-mode imaging. *IEEE Trans Ultrason Ferroelectr Freq Control*, 54(1):32–41, Jan 2007.

12. H. G. Blaas, S. H. Eik-Nes, T. Kiserud, S. Berg, B. Angelsen, and B. Olstad. Three-dimensional imaging of the brain cavities in human embryos. *Ultrasound Obstet Gynecol*, 5(4):228–232, Apr 1994.

13. N. Bom, C. T. Lancee, G. van Zweiten, F. E. Kloster, and J. Roelandt. Multiscan echocardiography. I. Technical description. *Circulation*, 48(5): 1066–1074, Nov 1973.

14. D. Bonnet, A. Coltri, G. Butera, L. Fermont, J. L. Bidois, J. Kachaner, and D. Sidi. Detection of transposition of the great arteries in fetuses reduces neonatal morbidity and mortality. *Circulation*, 99(7):916–918, Feb. 1999.

15. S. Brekke, E. Tegnander, S. H. Eik-Nes, and H. G. Torp. Tissue Doppler gated (TDOG) dynamic 3D ultrasound imaging of the fetal heart. *Ultrasound Obstet Gynecol*, 24(5):192–198, May 2004.

16. Q. L. Cao, N. G. Pandian, J. Azevedo, S. L. Schwartz, M. Vogel, D. Fulton, and G. Marx. Enhanced comprehension of dynamic cardiovascular anatomy by three-dimensional echocardiography with the use of mixed shading techniques. *Echocardiography*, 11(6):627–633, Nov 1994.

17. F. M. Chang, K. F. Hsu, H. C. Ko, B. L. Yao, C. H. Chang, C. H. Yu, R. I. Liang, and H. Y. Chen. Fetal heart volume assessment by three-dimensional ultrasound. *Ultrasound Obstet Gynecol.*, 7(1):42–48, Jan 1997.

18. C. Corsi, R. M. Lang, F. Veronesi, L. Weinert, E. G. Caiani, P. MacEneaney, C. Lamberti, and V. Mor-Avi. Volumetric quantification of global and regional left ventricular function from real-time three-dimensional echocardiographic images. *Circulation*, 112(8):1161–1170, Aug 23 2005.

19. D. L. Dekker, R. L. Piziali, and E. D. Jr. A system for ultrasonically imaging the human heart in three dimensions. *Comput Biomed Res*, 7(6): 544–553, 1974.

20. A. Delabays, N. G. Pandian, Q. L. Cao, L. Sugeng, G. Marx, A. Ludomirski, and S. L. Schwartz. Transthoracic real-time three-dimensional echocardiography using a fan-like scanning approach for data acquisition: methods, strengths, problems, and initial clinical experience. *Echocardiography*, 12(1):49–59, Jan 1995.

21. I. Donald, J. MacVicar, and T. G. Brown. Investigation of abdominal masses by pulsed ultrasound. *Lancet*, 271(7032):1188–1195, June 7 1958.

22. I. Edler and C. H. Hertz. The use of ultrasonic reflectoscope for the continuous recording of the movements of heart walls. *Kungl Fysiogr Sällsk Lund F*, 24:1–19, 1954.

23. H. Feigenbaum. Evolution of echocardiography. *Circulation*, 93:1321–1327, 1996.

24. S. Fukuda, T. Hozumi, H. Watanabe, T. Muro, H. Yamagishi, M. Yoshiyama, K. Takeuchi, and J. Yoshikawa. Freehand three-dimensional echocardiography with rotational scanning for measurements of left ventricular volume and ejection fraction in patients with coronary artery disease. *Echocardiography*, 22(2):111–119, Feb 2005.

25. E. A. Geiser, M. Ariet, D. A. Conetta, S. M. Lupkiewicz, L. G. C. Jr., and C. R. Conti. Dynamic three-dimensional echocardiographic reconstruction of the intact human left ventricle: technique and initial observations in patients. *Am Heart J*, 103(6):1056–1065, 1982.

26. O. H. Gilja, A. I. Smievoll, N. Thune, K. Matre, T. Hausken, S. Ødegaard, and A. Berstad. In vivo comparison of 3D ultrasonography and magnetic resonance imaging in volume estimation of human kidneys. *Ultrasound Med Biol*, 21(1):25–32, 1995.

27. L. F. Goncalves, W. Lee, J. Espinoza, and R. Romero. Examination of the fetal heart by four-dimensional (4D) ultrasound with spatio-temporal image correlation (STIC). *Ultrasound Obstet Gynecol*, 27(3):336–348, Mar 2006.

28. A. S. Gopal, A. M. Keller, R. Rigling, D. L. K. Jr, and D. L. King. Left ventricular volume and endocardial surface area by three-dimensional echocardiography: comparison with two-dimensional echocardiography and nuclear magnetic resonance imaging in normal subjects. *J Am Coll Cardiol*, 22(1):258–270, Jul 1993.

29. A. Heimdal, A. Stoylen, H. Torp, and T. Skjaerpe. Real-time strain rate imaging of the left ventricle by ultrasound. *J Am Soc Echocardiogr*, 11 (11):1013–1019, November 1998.

30. S. Holm, B. Elgetun, and G. Dahl. Properties of the beampattern of weight- and layout-optimized sparse arrays. *IEEE Trans Ultrason Ferroelectr Freq Control*, 44(5):983–991, Sept 1997.

31. R. C. Houck, J. Cooke, and E. A. Gill. Three-dimensional echo: transition from theory to real-time, a technology now ready for prime time. *Curr Probl Diagn Radiol*, 34(3):85–105, May-Jun 2005.

32. D. H. Howry, G. Posakony, C. R. Cushman, and J. H. Holmes. Three-dimensional and stereoscopic observation of body structures by ultrasound. *J Appl Physiol*, 9:304–306, 1956.

33. C. H. Jr and M. J. Irwin. Display system for displaying information in the form of a horizontally oriented curve on a raster type CRT. US Patent 4117473, 1977.

34. C. Kasai, K. Namekawa, A. Koyano, and R. Omoto. Real-time two-dimensional blood flow imaging using an autocorrelation technique. *IEEE Trans Sonics Ultrasonics*, 32:458–463, May 1985.

35. M. Kornbluth, D. H. Liang, A. Paloma, and I. Schnittger. Native tissue harmonic imaging improves endocardial border definition and visualization of cardiac structures. *J Am Soc Echocardiogr*, 11(7):693–701, Jul 1998.

36. B. J. Krenning, M. M. Voormolen, and J. R. Roelandt. Assessment of left ventricular function by three-dimensional echocardiography. *Cardiovasc Ultrasound*, 1(1):1–12, Sep 2003.

37. K. Kristoffersen. Time-domain estimation of the center frequency of Doppler spectra in diagnostic ultrasound. *IEEE Trans Ultrason Ferroelectr Freq Control*, 35(4):484–497, July 1988.

38. S. Langeland, J. D'hooge, H. Torp, B. Bijnens, and P. Suetens. Comparison of time-domain displacement estimators for two-dimensional rf tracking. *Ultrasound Med Biol*, 29(8):1177–1186, Aug 2003.

39. J. D. Larson. 2-D phased array ultrasound imaging system with distributed phasing. US Patent 5229933, 1993.

40. M. Leitman, P. Lysyansky, S. Sidenko, V. Shir, E. Peleg, M. Binenbaum, E. Kaluski, R. Krakover, and Z. Vered. Two-dimensional strain-a novel software for real-time quantitative echocardiographic assessment of myocardial function. *J Am Soc Echocardiogr*, 17(10):1021–1029, Oct 2004.

41. M. Levoy. Display of surfaces from volume data. *IEEE Computer Graphics and Applications*, 8(3):29–37, May 1988.

42. L. Lovstakken, S. Bjaerum, K. Kristoffersen, R. Haaverstad, and H. Torp. Real-time adaptive clutter rejection filtering in color flow imaging using power method iterations. *IEEE Trans Ultrason Ferroelectr Freq Control*, 53(9):1597–1608, Sept 2006.

43. W. N. McDicken, G. R. Sutherland, C. M. Moran, and L. N. Gordon. Colour Doppler velocity imaging of the myocardium. *Ultrasound Med Biol*, 18(6-7):651–654, 1992.

44. R. A. Meyer. History of ultrasound in cardiology. *J Ultrasound Med*, 23 (1):1–11, Jan 2004.

45. M. Meyer-Wittkopf, S. Cooper, J. Vaughan, and G. Sholler. Three-dimensional (3D) echocardiographic analysis of congenital heart disease in the fetus: Comparison with cross-sectional (2D) fetal echocardiography. *Ultrasound Obstet Gynecol*, 17(6):485–492, June 2001.

46. H. Nakatani, S. Tamura, K. Tanaka, A. Kitabatake, and M. Inoue. A binocular stereoscopic display system for echocardiography. *IEEE Trans Biomed Eng*, 26(2):65–68, February 1979.

47. F. Orderud. A framework for real-time left ventricular tracking in 3d+t echocardiography, using nonlinear deformable contours and Kalman filter based tracking. In *Computers in Cardiology Proceedings vol 33*, pages 125–128, Missouri, 2006. Computers in Cardiology Inc.

48. N. G. Pandian, N. C. Nanda, S. L. Schwartz, P. Fan, Q. L. Cao, R. Sanyal, T. L. Hsu, B. Mumm, H. Wollschlager, and A. Weintraub. Three-dimensional and four-dimensional transesophageal echocardiographic imaging of the heart and aorta in humans using a computed

tomographic imaging probe. *Echocardiography*, 9(6):677–687, Novembe 1992.

49. J. Patzold, W. Krause, H. Kresse, and R. Soldner. Present state of an ultrasonic cross-section procedure with rapid image rate. *IEEE Trans Biomed Eng*, 17(3):263–265, July 1970.

50. M. H. Pedersen, K. L. Gammelmark, and J. A. Jensen. In-vivo evaluation of convex array synthetic aperture imaging. *Ultrasound Med Biol*, 33(1): 37–47, Jan 2007.

51. O. T. V. Ramm, S. W. Smith, and H. G. P. Jr. High-speed ultrasound volumetric imaging system - part II: Parallel processing and image display. *IEEE Trans Ultrason Ferroelectr Freq Control*, 38(2):109–115, Mar 1991.

52. R. Righetti, S. Srinivasan, and J. Ophir. Lateral resolution in elastography. *Ultrasound Med Biol*, 29(May):695–704, 5 2003.

53. G. Sakas, L. A. Schreyer, and M. Grimm. Preprocessing and volume rendering of 3D ultrasonic data. *IEEE Trans Comp Graph and App*, 15(4): 47–54, July 1995.

54. S. Satumora. Ultrasonic Doppler method for inspection of cardiac function. *J Axoust Soc Am*, 29:1181–1185, 1957.

55. B. J. Savord. Integrated circuitry for use with transducer elements in an imaging system. US Patent 2001/0043090 A1, 2001.

56. D. P. Shattuck, J. Ophir, G. W. Johnson, Y. Yazdi, and D. Mehta. Explososcan: a parallel processing technique for high speed ultrasound imaging with linear phased arrays. *J Acoust Soc Am.*, 75(4):1273–1282, 1984.

57. M. S. Sklansky, G. R. DeVore, and P. C. Wong. Real-time 3-dimensional fetal echocardiography with an instantaneous volume-rendered display: early description and pictorial essay. *J Ultrasound Med.*, 23(2):283–289, Feb 2004.

58. S. W. Smith, H. G. P. Jr., and O. T. von Ramm. High-speed ultrasound volumetric imaging system part I: Transducer design and beam steering. *IEEE Trans Ultrason Ferroelectr Freq Control*, 38(2):100–108, Mar 1991.

59. S. Srinivasan, R. Righetti, and J. Ophir. An experimental characterization of elastographic spatial resolution: analysis of the trade-offs between spatial resolution and contrast-to-noise ratio. *Ultrasound Med Biol*, 30(10): 1269–1280, October 2004.

60. E. Steen and B. Olstad. Volume rendering of 3D medical ultrasound data using direct feature mapping. *IEEE Trans. Med. Imaging*, 13(3):517–525, Sept. 1994.

61. L. Sun, C. Feng, J. M. Cannata, J. A. Johnsen, J. T. Yen, and K. K. Shung. A real-time high frame rate high frequency ultrasonic system for cardiac imaging in small animals. In *Proc IEEE Ultrasonic Symposium*, pages 2206–2209. IEEE UFFC, IEEE UFFC Society, 2006.

62. E. Tegnander and S. H. Eik-Nes. The examiner's ultrasound experience has a significant impact on the detection rate of congenital heart defects at the second-trimester fetal examination. *Ultrasound Obstet Gynecol*, 28 (1):8–14, Jul 2006.

63. E. Tegnander, S. H. Eik-Nes, and D. T. Linker. Incorporating the four-chamber view of the fetal heart into the second-trimester routine fetal examination. *Ultrasound Obstet Gynecol*, 4(1):24–28, Jan 1994.

64. E. Tegnander, W. Williams, O. J. Johansen, H. G. Blaas, and S. H. Eik-Nes. Prenatal detection of heart defects in a non-selected population of 30,149 fetuses–detection rates and outcome. *Ultrasound Obstet Gynecol*, 27(3):252–265, Mar 2006.

65. G. E. Trahey, S. W. Smith, and O. T. von Ramm. Speckle pattern correlation with lateral aperture translation: Experimental results and implications for spatial compounding. *IEEE Trans Ultrason Ferroelectr Freq Control*, 33(3):257–264, May 1986.

66. G. E. Trahey, J. W. Allison, and O. T. von Ramm. Angle independent ultrasonic detection of blood flow. *IEEE Trans Biomed Eng*, 34(12):965–967, December 1987.

67. A. E. van den Bosch, A. H. Koning, F. J. Meijboom, J. S. McGhie, M. L. Simoons, P. J. van der Spek, and A. J. Bogers. Dynamic 3D echocardiography in virtual reality. *Cardiovasc Ultrasound*, 3:37, 2005.

68. D. U. Virtual Imaging Laboratory. A brief introduction to ultrasound, 2007. URL `http://dukemil.egr.duke.edu/Ultrasound/k-space/node2.html`. [Online; accessed 21-March-2007].

69. X. F. Wang, Z. A. Li, T. O. Cheng, M. X. Xie, G. Hu, Y. B. Deng, L. Liu, and Q. Lu. Four-dimensional echocardiography: methods and clinical application. *Am Heart Jounal*, 132(3):672–684, Sept 1996.

70. C. D. Watkins, A. Sadun, and S. Marenka. *Modern image processing : warping, morphing, and classical techniques*. Academic Press Professional, 1st edition, 1993.

71. A. Watt. *3D Computer Graphics*. Addison Wesley, 3rd edition, 1999.

72. J. Whitlock and K. Palaniappan. Vr heart model, 2007. URL `http://meru.cecs.missouri.edu/mvl/vrheart/Heart.html`. [Online; accessed 13-March-2007].

73. Wikipedia. Doppler effect — Wikipedia, the free encyclopedia, 2007. URL `http://en.Wikipedia.org/wiki/Dopplereffect`. [Online; accessed 21-March-2007].

74. J. J. Wild and D. Neal. Use of high-frequency ultrasonic waves for detecting changes of texture in living tissues. *Lancet*, 1(1):655–657, Mars 1951.

75. S. Yagel, S. M. Cohen, and R. Achiron. Examination of the fetal heart by five short-axis views: a proposed screening method for comprehensive cardiac evaluation. *Ultrasound Obstet Gynecol*, 17(5):367–369, 2001.

76. S. Yusuf, S. Reddy, S. Ounpuu, and S. Anand. Global burden of cardiovascular diseases: part I: general considerations, the epidemiologic transition, risk factors, and impact of urbanization. *Circulation*, 104(22):2746–2753, Nov 2001.

77. D. S. Zrnic. Spectral moment estimates from correlated pulsed pair. *IEEE Trans Aerosp Electron*, 13:344–354, 1977.

Increasing frame rate in ultrasound imaging by temporal morphing using tissue Doppler

Svein Brekke, Charlotte B. Ingul, Svein A. Aase and Hans G. Torp
Dept. of Circulation and Medical Imaging, NTNU, Trondheim, Norway

Abstract

The diagnostic value of echocardiographic images seems to diminish when the frame rate is low. In this work, morphing based on velocity information was utilized to improve the perceived smoothness of B-mode cine-loops with low frame rate. Based on an estimate of the velocity field calculated from B-mode speckle tracking and tissue Doppler measurements, morphed cine-loops with arbitrarily high frame rate were created.

Morphing was applied to cardiac ultrasound cine-loops with apical insonation. The quality of the morphed data was evaluated by removing frames from duplex B-mode and tissue Doppler recordings, then replacing the removed B-mode frames with morphed ones. The decimated and morphed sequences were compared to the original ones.

Wall motion scoring, a subjective evaluation technique for regional viability of the myocardium, was applied to data from 20 patients with varying pathology. 60 cine-loops were scored twice, first with original data and later with morphed data. The results were compared for each recording, and the scorings were identical in the two cases for 94% of the segments.

We conclude that much of the diagnostic value is retained in recordings with 15 frames per second when temporal morphing is applied.

IEEE Trans UFFC, vol. 53, no. 5, pp. 936-946, May 2006.

1 Introduction

In ultrasonic imaging of the human heart, one always has to find a compromise between image quality and frame rate, in particular when doing color Doppler or tissue Doppler imaging. When acquiring real-time 3D cardiac ultrasound data, this compromise becomes even harder. However, there are techniques to enhance the display of ultrasound data when the frame rate is low.

When the data rate of an ultrasound scan is below the screen refresh rate, a common way to make the motion look smoother is to interpolate the data at a given screen refresh time as a linear combination of the previous and next ultrasound data available. (This is possible if the display lags 1 frame behind the data acquisition.) If the target of the image is moving or deforming, such interpolation creates artefacts, and when in cardiac imaging the frame rate gets below 20, smoothing artefacts become severe.

There are however other methods for creating intermediate frames that better preserve structure. An image metamorphosis, or a morphing for short, is a continuous, smooth transformation from one digital image to another [27]. In this work, tissue velocity data were utilized to create morphed frames in echocardiographic image sequences, and a specific clinical context was considered: Stress echo examinations of the adult left ventricle (LV).

In this application area, the patient's heart rate is high and thus high frame rate is required. Furthermore, simultaneous recording of 2D tissue Doppler and B-mode images are often advantageous, and it is even possible to record tissue Doppler data at a higher frame rate than the B-mode data [12]. In addition, with a 2D array probe, simultaneous tissue Doppler recording in two or three imaging planes has become feasible, which further reduces the achievable frame rate. A typical setup on a Vivid 7 system from GE Healthcare can be at least 50 frames per second in tissue Doppler and 10 frames per second for B-mode in each of three image planes. With real time 3D tissue Doppler imaging of the left ventricle, acquisition rates will become even lower - probably below 10 gray-scale volumes per second. Adequate algorithms for morphing 3D gray-scale images will then be helpful when striving to sustain B-mode image quality.

To calculate a continuous morphing from one frame $X(t_0)$ into a successive one $X(t_1)$, the velocity field in the entire image is required. Two different sources of information are commonly used to estimate velocities of human tissue by ultrasound: Doppler autocorrelation and speckle tracking.

Tissue Doppler

Since the 1980s, ultrasound scanners have used Doppler autocorrelation techniques to measure the blood velocity field in B-mode images [11]. The velocity field is usually presented to the operator as a colour overlay to the B-mode image.

The same technique was also proved to work for tissue velocity measurement and display [15;22]. The radial velocity component of the muscle may be estimated from Doppler shifts measured in the myocardium, but the lateral velocity remains unknown, often referred to as angle-dependency of the method [21]. (Directions are specified relative to the ultrasound beam: Radial direction is along the ultrasound beam and lateral direction is perpendicular to the beam.) Another limitation by the Doppler approach is the aliasing problem: The measured radial velocity is correct only if the Doppler shift does not exceed half the pulse repetition frequency [9].

Despite of the limitations, tissue Doppler has proved to be a useful tool for assessment of myocardial ischemia [20]. A recent step forward towards automatic quantification of left ventricular function is auto-detection of apex and the atrioventricular plane (AV-plane) by tissue Doppler, demonstrated in Torp et al. [23].

Speckle tracking

In ultrasonic as well of other types of backscatter imaging, the relative position of scatterers within a region creates an interference pattern in the image. The pattern in a given position remains relatively unchanged from frame to frame in an image sequence, even though the structures in the image moves or deforms [16]. This fact can be utilized to calculate the displacement of the tissue in a specific location $\mathbf{r}$ from one frame to the next, by searching for the speckle pattern surrounding $\mathbf{r}$ in different but nearby positions. Performing speckle tracking from one frame to the next in every point in an image results in an estimate $\hat{\mathbf{d}}_{ij} \triangleq \hat{\mathbf{d}}(\mathbf{r}_{ij})$ of the tissue displacement between the two time points. However, the spatial resolution in the derived displacement field is lower than that of the image itself, since neighbouring resolution estimates are strongly correlated. The mean velocities in the image between the two frames $X(t_0)$ and $X(t_1)$ may be estimated by $\hat{\mathbf{v}} = \hat{\mathbf{d}}/\Delta t$. Early work on speckle tracking include Barnea and Silverman [2] (a generic formulation of pattern tracking using sum of absolute differences, SAD), Trahey et al. [24] (using the displacement field for enhanced compound imaging) and Bohs and Trahey [3]; Trahey et al. [25] (using it to estimate magnitude and direction of blood flow). Speckle tracking used to generate images of the elastic properties of human tissue has also been investigated by numerous contributors, e.g. O'Donnell et al. [17]; Ophir et al. [18]; Varghese and Ophir [26]. Recently, speckle tracking has been used for both strain rate imaging and anatomic tracking of regions in the myocardium [6]. Furthermore, warping (nonrigid mappings from one image into another) derived from tracking of larger blocks, has been used for image quality improvements in compound ultrasound imaging [8;13].

This work shows how velocity estimates obtained by speckle tracking and tissue Doppler may improve image quality through morphing of B-mode data

with low frame rate, and the diagnostic value of B-mode data with different frame rates has been evaluated. The text continues with five parts: A theory section with description of concepts and notation, a section describing the method and material used in the experiments, a section presenting the results of the experiments, a section with discussion of the results and finally a conclusion.

2 Theory

2.1 Tracking motion in deforming bodies

Ignoring, for a moment, that an ultrasound image is a discreet representation of a continuously moving body, a 2-dimensional moving image can be described as a continuous function of time and space.

$$X(\mathbf{r}, t); \qquad \text{with } X : \mathcal{D} \times [0, T] \to \mathbb{R} \tag{A.1}$$

The domain $\mathcal{D}$ of the image mapping X may either be a part of a 2-D plane (usually a sector or a rectangle), or of 3-D space (e.g. a pyramidal volume), and the mapping is defined for all spatial coordinates $\mathbf{r} \in \mathcal{D}$. Our goal is to find an estimate $\hat{X}$ for the intermediate mappings $X(\mathbf{r}, t)$ given two "frames", i.e. given the full image at two specific moments in time:

$$\hat{X}(\mathbf{r}, t \,|\, t_0, t_1, X(\mathbf{r}, t_0), X(\mathbf{r}, t_1)) \tag{A.2}$$

A simple estimate for the intermediate sequence can be written

$$\hat{X}(\mathbf{r}, t) = (1 - \alpha)X(\mathbf{r}, t_0) + \alpha X(\mathbf{r}, t_1). \tag{A.3}$$

In each point, this is a linear combination of the images values in the two sampled frames. The ratio $\alpha = \frac{t - t_0}{t_1 - t_0}$ runs from 0 to 1 as t runs from t_0 to t_1. Interpolation in a coordinate system that is fixed in space is often referred to as interpolation in *Euler coordinates*, see figure A.1.

When imaging the myocardium with inter-frame delay $t_1 - t_0$ equal to 50 ms or more, the values $X(\mathbf{r}, t_0)$ and $X(\mathbf{r}, t_1)$ will be sampled from different locations that may be as much as 5-10 mm apart [10]. Thus, the estimate in (A.3) degrades as frame rate decreases. A possible way to enhance the estimate in (A.3) is to follow myocardial motion in the interpolation: If for any $\mathbf{r}_0$ in the first given frame $X(\mathbf{r}, t_0)$, the position of the same scatterer in the second frame $X(\mathbf{r}, t_1)$ is denoted by $\mathbf{r}_1$, then for the location t at time $t \in (t_0, t_1)$ on the particle path, an enhanced estimate could be written

$$\hat{X}(\bar{\mathbf{r}}, t) = (1 - \alpha)X(\mathbf{r}_0, t_0) + \alpha X(\mathbf{r}_1, t_1) \tag{A.4}$$

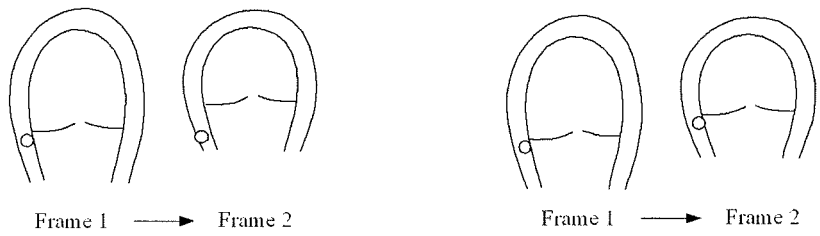

Figure A.1: Left panel: Interpolation in Euler coordinates, summing the echoes from two different material points. Right panel: Interpolation in a Lagrange-coordinates, summing the echoes from the same material point.

which is a linear combination of two echoes reflected by the same scatterer, with $\bar{\mathbf{r}}$ being the position of the actual scatterer at time t. Coordinates that follow the particle path in each location is referred to as *Lagrange coordinates*, see figures A.1 and A.2. If the velocity field $\mathbf{v}(\mathbf{r}, t)$ was completely known and a particle was located at $\mathbf{r}_0$ at time t_0, the path $\bar{\mathbf{r}}(t)$ of this particle may be calculated numerically for any $t > t_0$ from

$$\bar{\mathbf{r}}(t) = \mathbf{r}_0 + \int_{t_0}^{t} \mathbf{v}(\bar{\mathbf{r}}(\tau), \tau) d\tau. \tag{A.5}$$

The only inaccuracy of the estimator in (A.4) would then be the sampling error in obtaining the two images. However, available velocity estimates are neither very accurate, nor very densely sampled in space.

Now, let $X(t) \triangleq X(\mathbf{r}_{ij}, t) \triangleq \{\xi_{ij}(t)\}$ be an ultrasound B-mode image sampled at time t, where ξ_{ij} are the individual gain-compensated and log-compressed image samples. The indexes $i \in \{1, \cdots, S\}$ and $j \in \{1, \cdots, B\}$ denote sample number in radial and lateral direction and spans a grid that may be of sector type or linear type, S being number of samples per beam and B the number of beams in the grid. (Generalization to 3-D is straight forward with points $\mathbf{r}_{ijk} \in \mathbb{R}^3$; one index for each dimension). Let $X(t_0)$ and $X(t_1)$ be two successive ultrasound frames, and assume that a velocity estimate $\hat{\mathbf{V}}(\mathcal{T}) \triangleq \{\hat{\mathbf{v}}_{ij}(T_n)\}$ is sampled on the same spatial grid as X, but on different time points $\mathcal{T} \triangleq \{T_n\}_0^N$ satisfying $T_0 \leq t_0 \leq T_1$ and $T_{N-1} \leq t_1 \leq T_N$. The aim is to find a smooth transition of the image $X(t_0)$ into $X(t_1)$ defined for all intermediate times t between t_0 and t_1, i.e. an estimate of the form

$$\hat{X}(t \,|\, t_0, t_1, X(t_0), X(t_1), \hat{\mathbf{V}}(\mathcal{T})). \tag{A.6}$$

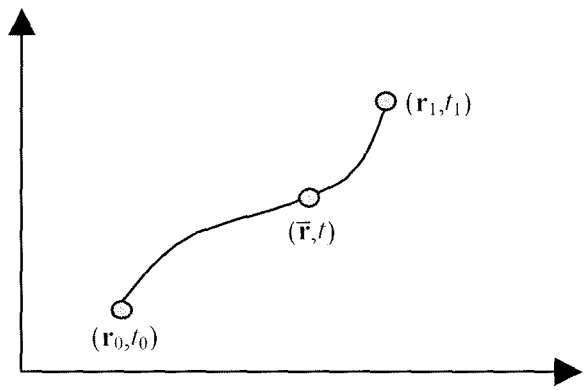

Figure A.2: A possible path $\bar{\mathbf{r}}(t)$ of one anatomical location in the image.

Interpolated frames in a fixed coordinate system (Euler coordinates) are calculated by applying (A.3) to each sample $\mathbf{r}_{ij}$, causing many of the estimated samples $\hat{\xi}_{ij}(t)$ to be a weighed sum of echoes from different material points. The result for the whole image is smearing or duplication of small structures. One way to reduce the artefacts is to use an approximation to the true Lagrange interpolation in (A.5). Consider a grid point $\mathbf{r}_{ij}$ for which a good estimate $\hat{\xi}_{ij}(t)$ is required, and let the points $\mathbf{r}_{ab}$ in $X(t_0)$ and $\mathbf{r}_{cd}$ in $X(t_1)$ be chosen so that a particle path from $\mathbf{r}_{ab}$ to $\mathbf{r}_{cd}$ passes through $\mathbf{r}_{ij}$, as in figure A.2: An enhanced estimator for the morphed pixel can then be written as a linear interpolation between the pixel values:

$$\hat{\xi}_{ij}(t) = (1-\alpha)\xi_{ab}(t_0) + \alpha\xi_{cd}(t_1) \tag{A.7}$$

When calculating the mophed images presented in this work, the velocity was assumed not to change much between t_0 and t_1, justifying that the particle motion from $\mathbf{r}_{ab}$ to $\mathbf{r}_{cd}$ was approximately constant. Thus, each morphed image sample was calculated by setting

$$\begin{aligned} \mathbf{r}_{ab} &\approx \mathbf{r}_{ij} - \alpha\hat{\mathbf{v}}_{ij}(T')(t_1 - t_0) \\ \mathbf{r}_{cd} &\approx \mathbf{r}_{ij} + (1-\alpha)\hat{\mathbf{v}}_{ij}(T')(t_1 - t_0) \end{aligned} \tag{A.8}$$

in (A.7), with integer indexes a, b, c and d. The utilized velocity $\hat{\mathbf{v}}_{ij}(T')$, T' being the acquisition time of the tissue Doppler frame closest to $\frac{1}{2}(t_0+t_1)$, was the velocity estimate closest in space and time to the morphed image sample.

Though not investigated in detail in this study, one should be aware there are other and possibly better ways than (A.8) to calculate $\mathbf{r}_{ab}$ and $\mathbf{r}_{cd}$ based on $\hat{\mathbf{V}}$:

1. If any one of the velocity gradients

$$\frac{\partial \mathbf{v}(\mathbf{r})}{\partial \mathbf{r}} \triangleq \begin{bmatrix} \frac{\partial v_x}{\partial x} & \frac{\partial v_y}{\partial x} \\ \frac{\partial v_x}{\partial y} & \frac{\partial v_y}{\partial y} \end{bmatrix} \tag{A.9}$$

   is large, then $\hat{\mathbf{v}}_{ab}(T')$ may differ substantially from $\hat{\mathbf{v}}_{cd}(T')$, and it would be appropriate to incorporate both in the estimator, e.g. by using the mean of these two velocities: Find points $\mathbf{r}_{ab}$ and $\mathbf{r}_{cd}$ satisfying $\bar{\mathbf{v}}\Delta t = \mathbf{r}_{cd} - \mathbf{r}_{ab}$ where $\bar{\mathbf{v}} = \frac{1}{2}(\hat{\mathbf{v}}_{ab}(T') + \hat{\mathbf{v}}_{cd}(T'))$ and $\mathbf{r}_{ij} = \mathbf{r}_{ab} + \alpha\bar{\mathbf{v}}$. Additionally, the path with constant velocity $\bar{\mathbf{v}}$ from $\mathbf{r}_{ab}$ to $\mathbf{r}_{cd}$ must pass through $\mathbf{r}_{ij}$ at time t, which gives condition (A.8) with $\hat{\mathbf{v}}_{ij}(T')$ replaced with $\bar{\mathbf{v}}$.

2. If the acceleration is high, $\hat{\mathbf{v}}_{ij}(t_0)$ may differ substantially from $\hat{\mathbf{v}}_{ij}(t_1)$, and (A.8) may be enhanced by using $\tilde{\mathbf{v}} = \frac{1}{\Delta t}\int_{t_0}^{t_1} g(\hat{\mathbf{v}}_{ij}(\mathcal{T}), t)dt$ instead of $\hat{\mathbf{v}}_{ij}(T')$, where the function g is any function that interpolates the sequence $\hat{\mathbf{v}}_{ij}(\mathcal{T})$ at time t, e.g. linear interpolation or spline interpolation.

3. The most accurate, but also the most computationally expensive approximation to $\mathbf{r}_{ab}$ and $\mathbf{r}_{cd}$ would be to calculate the exact solution (A.5) numerically:

$$\begin{array}{rcl} \Delta\mathbf{r}(\tau) & = & \int_t^{\mathcal{T}} \hat{\mathbf{V}}(\mathbf{r}_{ij} + \Delta\mathbf{r}(t'), t')dt' \\ \mathbf{r}_{ab} & \approx & \mathbf{r}_{ij} + \Delta\mathbf{r}(t_0) \\ \mathbf{r}_{cd} & \approx & \mathbf{r}_{ij} + \Delta\mathbf{r}(t_1) \end{array} \tag{A.10}$$

   This would allow for interpolation of locations along a curve rather than a straight line. By increasing the spatial resolution of the velocity field $\hat{\mathbf{V}}$ by e.g. spline-interpolated prior to integration, the integral even could be evaluated at higher spatial resolution than the sampling grid of the image.

The estimators 2 and 3 above may be computed readily from $X(t_0)$, $X(t_1)$ and $\hat{\mathbf{V}}(\mathcal{T})$, while the estimator 1 involves searching after valid solutions in each grid point $\mathbf{r}_{ij}$, and there may be points with zero, one or several solutions.

2.2 Impact of the velocity field estimate on morphed images

The morphing algorithm in (A.7) utilizes the velocity estimate locally to create intermediate frames. Each coordinate $\mathbf{r} \in \mathcal{D}$ is morphed along the path $\bar{\mathbf{r}}(t)$ given by (A.5), thus transforming the initial domain $\mathcal{D}$ of the image mapping to a different shape $\bar{\mathcal{D}}(t)$. By replacing the true velocity $\mathbf{v}$ by the spatial and

temporal sampled estimate $\hat{\mathbf{V}}$, we get an approximation $\hat{\mathcal{D}}(t)$ of this transform. For a morphing to be physically correct, each $\hat{\mathcal{D}}(t)$ should constitute an elastic deformation of $\mathcal{D}$, which specifically implies that no morphing paths of different location should cross each other, and that all points in $\hat{\mathcal{D}}(t_1)$ should be the destination of a morphing path starting in $\mathcal{D}(t_0)$.

When measuring velocity in a practical measurement system, velocities are available only in a limited number of points in space, and the number of velocity samples in ultrasonic images generally is lower than the number of B-mode samples. Hence, to achieve a velocity estimate in each point of the B-mode image, one needs to interpolate the velocity measurements to a higher spatial resolution. In section 3, two different strategies for up-interpolation are investigated: 1) measure the velocity in fixed spatial grid and thereafter do linear interpolation between grid points and 2) measure the velocity in certain anatomical landmarks in the image and then extend these velocities to the entire image.

To avoid crossing morphing paths, large spatial gradients in the velocity field estimate should be avoided. In regions with intra-cardiac blood flow, the true velocity field frequently has large gradients due to turbulence and is thus unrealistic to capture accurately. Additionally, tissue Doppler velocity estimates in blood flow regions are characterized by high variance and aliasing. In contrast, the myocardium itself is characterized by relatively low strain from frame to frame, implying limited velocity gradients. Thus, one could expect that a velocity field estimate that suppresses velocity measurements from blood flow exhibit fewer artefacts when utilized for morphing of B-mode images.

3 Method and material

3.1 Speckle tracking

Tracking the speckle pattern in one location from one frame to the next is performed in two steps: Searching and matching. The matching criterion may use the radio frequency echo signal (RF signal) where both amplitude and phase of the backscattered pulse contributes to the cost function, or it may use detected echo data, discarding the phase information and only using the amplitude [4]. For matching done on detected data, both maximizing the cross-correlation and minimizing the sum of absolute difference have been investigated.

The accuracy of estimated displacement vector is better in radial direction than in the lateral [4;19], because the spatial resolution is lower in the lateral direction. To enhance the lateral resolution, one commonly interpolate the image, e.g. with a factor of two, doubling the number of beams in the search. More advanced techniques for getting sub-sample accuracy in the lateral direction have been suggested: Grid-slopes [7] and synthetic lateral phase [5]. Calculating time lag in the

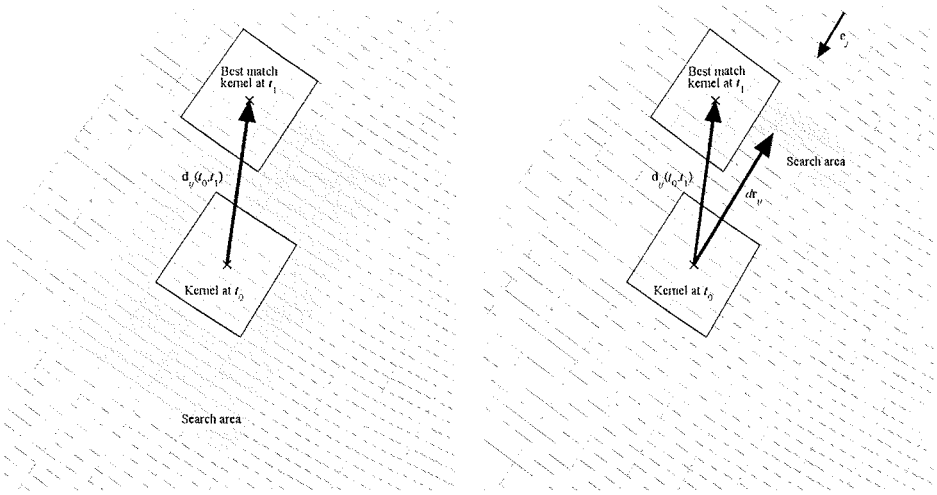

Figure A.3: Left panel: Traditional speckle tracking in a two-dimensional sector scan, with realistic search region size, kernel size and scan geometry. Right panel: Doppler aided speckle tracking may use much smaller search region.

RF signal gives the best result for small displacements in the radial direction, while in the lateral direction, RF signal matching performs well only if the lateral sampling distance is very small. However, in myocardial cine-loops with low frame rate, the maximal displacements are substantial and the lateral sampling distance is relatively large. Hence, according to Bohs et al. [4], one can expect that searching in the detected signals yields the best result in the myocardium, and the tracking performed in this work was calculated with this method.

3.2 Local velocity estimator

A new technique for local tissue velocity estimation is proposed: Doppler aided speckle tracking (DAST). The technique is only applicable when B-mode and tissue Doppler data is acquired simultaneously. Calculation of $\hat{\mathbf{v}}(\mathbf{r}_{ij})$ for any location $\mathbf{r}_{ij}$ in the acquisition grid consists of two steps, see figure A.3:

1. Radial displacement is calculated from the tissue Doppler data: $d\mathbf{r}_{ij} = \Delta t\, v_D \mathbf{e}_j$, where $\mathbf{e}_j$ is a unit vector directed from the probe along beam number j, and $v_D \triangleq v_D(\mathbf{r}_{ij}, T')$ is the radial velocity estimate calculated from the tissue Doppler frame at time T' succeeding t_0. The vector $d\mathbf{r}_{ij}$ is

shown in figure A.3 and corresponds to a displacement of

$$i_D = v_D \Delta t / \Delta r \tag{A.11}$$

samples along the beam, with Δr denoting the radial sampling distance.

2. A speckle tracking search is performed, with the search region centered in $\mathbf{r}_{i+i_D,j}$. In each location $\mathbf{r}_{kl}$ in the search region, a sum of absolute differences is calculated:

$$\begin{aligned} \mathrm{SAD}(k,l|\mathbf{r}_{ij},i_D) &= \sum_{m=-M}^{M}\sum_{n=-N}^{N} |X(i+m,j+n,t_0) \\ &- X(i+m+k+i_D,j+n+l,t_1)|, \end{aligned} \tag{A.12}$$

where the kernel size is $(2M+1, 2N+1)$. Finally, the SAD function is calculated for each shift (k,l) within a predefined search region, and the displacement of $\mathbf{r}_{ij}$ from $X(t_0)$ to $X(t_1)$ is estimated as the distance from $\mathbf{r}_{ij}$ to the search location with the minimal sum, say $k=K$ and $l=L$:

$$\hat{\mathbf{d}}_{ij}(t_0,t_1) = \mathbf{r}_{i+i_D+K,j+L} - \mathbf{r}_{ij} \tag{A.13}$$

From (A.13) the local velocity estimator is calculated as

$$\hat{\mathbf{v}}_{ij}(t_0 + \frac{\Delta t}{2}) = \frac{\hat{\mathbf{d}}_{ij}(t_0,t_1)}{\Delta t} \tag{A.14}$$

The SAD function was either calculated directly from the B-mode frames, or calculated from frames that were up-sampled by a factor R_{lat} with a polynomial low-pass filter in the lateral direction. In the latter case, the points $\mathbf{r}_{xy}$ in (A.13) denote grid points in a grid more densely sampled than the original frame.

In tissue Doppler imaging the Doppler data may be acquired at higher frame rate than the B-mode data[12]. For recordings with N times higher tissue Doppler frame rate than B-mode frame rate, the speckle tracking start displacement i_D is calculated from a weighed sum over the available tissue Doppler velocity estimates by replacing v_D in (A.11) by:

$$\bar{v} = \frac{1}{\sum_1^N w_n} \sum_1^N w_n v_D(T_n), \tag{A.15}$$

where the intermediate weights $w_2, \cdots, w_{N-1}$ has value 1, and the start- and end weight $w_1 = \frac{T_2 - t_0}{\Delta T}$ and $w_N = \frac{T_N - t_1}{\Delta T}$ are smaller than unity. Thus, (A.15) is an approximation to the "true" Doppler mean velocity

$$\frac{1}{\Delta t}\int_{t_0}^{t_1} v_D(t)dt. \tag{A.16}$$

From the local displacement estimator in (A.13), the particle path from location $\mathbf{r}_{ij}$ is calculated for a cine-loop with frame times $\{t_n\}_{n=0}^{N_{fr}}$ by

$$\begin{aligned} \bar{\mathbf{r}}(t_0) &= \mathbf{r}_{ij} \\ \bar{\mathbf{r}}(t_{n+1}, \mathbf{e}) &= \bar{\mathbf{r}}(t_n) + \hat{\mathbf{d}}(t_n, t_{n+1}) + \mathbf{e} \end{aligned} \tag{A.17}$$

The drift compensation term $\mathbf{e}$ ensures that the start point and end point in the cine-loop is the same:

$$\mathbf{e} = -\frac{1}{N_{fr}} \left[\bar{\mathbf{r}}(t_{N_{fr}} | \mathbf{e} = 0) - \mathbf{r}_{ij} \right]. \tag{A.18}$$

This compensation is based on the assumption that the state of the myocardium is the same in the first and the last frame in the cine-loop.

3.3 Velocity curves and anatomical tracking

Radial and lateral displacement tracked with the DAST estimator was investigated *in-vivo* on cine-loops showing apical views of the left ventricle of healthy adults. Displacements curves and derived velocity curves were compared to corresponding results of pure speckle tracking and pure tissue Doppler tracking applied to each recording. A lateral interpolation factor R_{lat} of 2 was applied, and the size of the search region for pure speckle tracking was derived from maximal allowed velocities: 13 cm/s in radial direction and 10 cm/s in lateral direction, see figure A.3. In the speckle tracking step in the combined estimator, the search region size corresponded to 1.5 cm/s radially and 10 cm/s laterally.

We present curves derived from one example recording, a four-chamber apical view with duration 1.2 seconds, B-mode frame rate of 40 frames per second and tissue Doppler frame rate of 120 frames per second. Both a location showing agreement as well as one showing disagreement between the three calculation methods are presented.

3.4 Velocity field estimates

Aiming to interpolate subsequent ultrasound frames in true Lagrange coordinates, it is essential to have an adequate velocity estimate in every image location. Unfortunately, available local estimators tend to be too noisy to yield good results when used in morphing calculations. Different velocity field estimates were combined with the morphing estimator (A.7) to calculate morphed cine-loops from in-vivo B-mode frame sequences. Images considered were from three specific cardiac views: Apical four chamber, apical two chamber and apical long axis. In these views, the motion of the LV walls is principally along the ultrasound beams.

Four different velocity field estimators for morphing calculations were examined. The two first were purely local, while the two last, aiming to control the spatial gradients in the resulting velocity field, were extensions of velocity measurements from certain locations in the myocardium to a field estimate for the entire image:

1. *Doppler field estimate.* Tissue Doppler velocity measurements in the entire image: Velocities were calculated beam- and sample wise from tissue Doppler data and interpolated to the resolution of the B-mode image.

2. *Doppler field estimate with smoothing.* Same as 1., but with an additional 2-dimensional average filter applied, using a window size of 18 samples in the radial direction and 3 beams in the lateral direction (approximately 5 by 5 mm at the focal depth).

3. *Myocardium field estimate.* Using the DAST velocity estimator introduced in section 3.2: The user specified a curve through the center of the myocardium. Seven control points were positioned in the first frame of a cine-loop, and the motion of these points (except for the point in the LV apex, which was assumed to have zero velocity) was tracked throughout the cycle utilizing the estimator in section 3.2. By linear interpolation between the control points, the velocity estimate was extended to the entire ventricular wall, and by linear interpolation in the lateral direction on each sample depth in the image, the velocity estimate was extended to the whole ventricle. At the left and right side of the myocardium curve, the velocity vector was assumed to be constant at each sample depth.

4. *AV-plane field estimate.* The positions of the ventricular apex and the AV-plane may be detected and tracked automatically by tissue Doppler [23]. Applying this method gave an estimate for the radial displacement, and hence the radial velocity of the ventricular apex and the two AV-knots. Velocities in the entire frame was calculated from these three velocities by bi-linear interpolation in polar coordinates.

In the latter two algorithms, the velocity was assumed to decrease linearly from the AV-plane to zero in the cardiac base. The position of the cardiac base, being outside the imaged region, was rudimentary estimated to be on depth $1.7 * r_{AV}$, where r_{AV} was the distance from the probe to the AV-plane at the start of the cine-loop. The rationale for the factor 1.7 was that the length of the atria normally are approximately 70% of the length of the ventricles in a dilated myocardium.

3.5 Morphed cine-loops

The morphing calculations were applied to detected B-mode data sampled on a sector grid. Morphing as described in (A.7) and (A.8) was implemented in MATLAB and tested on various duplex B-mode and tissue Doppler recordings with apical insonation of the myocardium. Cine-loops created with all four velocity field estimators in section 3.4 are presented and compared to data created with linear interpolation (i.e. interpolation in Euler coordinates).

As a measure of morphing estimation error, the root mean square difference between morphed pixel data and original pixel data was calculated frame-wise for each morphing method:

$$D(t_n) \triangleq \frac{1}{S \cdot B} \sqrt{\sum_{i=1}^{S} \sum_{j=1}^{B} \left| \xi_{ij}(t_n) - \hat{\xi}_{ij}(t_n) \right|^2} \tag{A.19}$$

The image samples ξ_{ij} were single byte unsigned integers, i.e. $0 \leq \xi_{ij} \leq 255$.

3.6 Test of diagnostic value

Wall motion scoring is a diagnostic technique where local viability of the myocardium is assessed from B-mode ultrasound images [1]. To score the wall motion for a patient, cine-loop data must be available from three specific cardiac views: apical 4-chamber, apical 2-chamber and apical long axis. From the three cine-loops, 16 different segments of the myocardium are scored based on thickening and inward motion, and given one of the values 1 (normal), 2 (hypokinesis), 3 (akinesis) and 4 (dyskinesis).

Ultrasound recordings that were previously used for diagnosis by wall motion scoring, were investigated to evaluate the quality of morphed B-mode data compared to B-mode data with higher frame rate. Each recording was decimated to a frame rate of approximately 15 frames/sec., and the removed frames were recreated by temporal morphing. The morphings were calculated by the myocardium velocity field estimate, see section 3.4.3. The morphed data sets were scored again, blinded and by the same operator as did the initial scoring. The results of the two scorings were compared, both patient-wise and segment-wise.

Data from 20 patients were examined; 10 healthy individuals with normal ventricle and 10 patients with myocardial infarction. The recordings consisted of B-mode cine-loops with 2D tissue Doppler data, and had frame rates between 26 and 126. The patients heart rates varied from 46 to 104, and the number of frames per cardiac cycle was between 20 and 150.

	Septum 40 fr/sec	LV lat. wall 40 fr/sec	Septum 10 fr/sec
Tissue Doppler tracking	0.2 / -	0.4 / -	0.6 / -
Speckle tracking	1.9 / 2.0	9.3 / 1.0	12.4 / 7.9
DAST	0.5 / 0	2.6 / 3.9	0.3 / 2.0

Table A.1: Size of the drift correction terms (A.18) applied to the coordinates of scatterers tracked throughout the cardiac cycle. Format: Radial correction/lateral correction in millimeters.

4 Results

This section present curves, images and movies created by the methods presented in sections 3.2 to 3.6, with only brief textual presentation. Interpretation and evaluation of the findings are presented in section 4.

4.1 Local velocity estimators

Figure A.4 shows how the tissue displacement and tissue velocity of a scatterer in the ventricular septum changed over time when estimated by each of the three local estimators: tissue Doppler tracking (green lines), speckle tracking (red lines) and finally the DAST estimator proposed in section 3.2 (blue lines). In addition, the rightmost panel shows the anatomically tracked path of the scatterer, i.e. displacement coordinates plotted for all time points in the same diagram.

While the velocity vectors in the ventricular septum usually is well aligned with the imaging plane, velocity vectors in the LV lateral wall frequently has a substantial component perpendicular to the imaging plane. Velocity and displacement curves measured in the LV lateral wall is shown in figure A.5, the ultrasound recording being the same as in figure A.4.

Figure A.6 shows the same information as figure A.4, at the same anatomical location and taken from the same ultrasound recording, but only using 25% of the recorded data for estimation (i.e. a data decimated by a factor of four).

The drift compensation terms (A.18) applied in the curves shown in figures A.4 to A.6 are listed in table A.1.

The movie in figure A.7 dynamically shows anatomically tracked paths from figures A.4 to A.6 in a side by side display, plotted on-top of the original B-mode image.

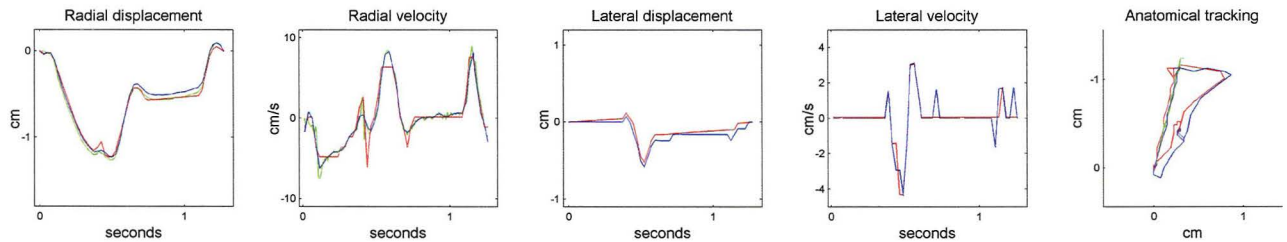

Figure A.4: Displacement and velocity estimates throughout a cardiac cycle from a material point in the ventricular septum. Red lines show velocities generated by B-mode speckle tracking, green lines velocities generated by tissue Doppler and blue lines velocities generated by combined tissue Doppler and B-mode speckle tracking estimation. Rightmost: The two-dimensional path through the cycle.

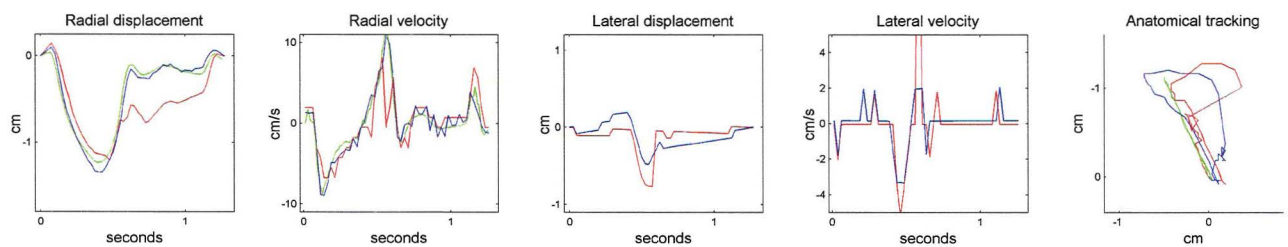

Figure A.5: Displacement and velocity estimates from a material point in the LV lateral wall. Notation as in figure A.4.

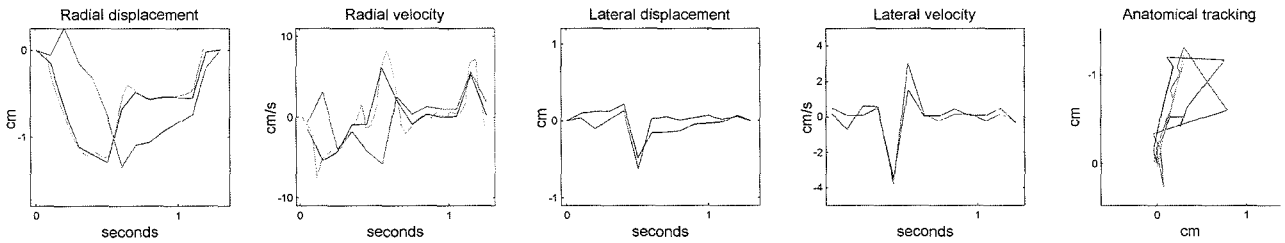

Figure A.6: Displacement and velocity estimates in the ventricular septum. Calculations were based on the same material point and the same cine-loop as in figure A.4, but with B-mode data decimated from 40 to 13 frames per second and tissue Doppler data decimated from 120 to 39 frames per second.

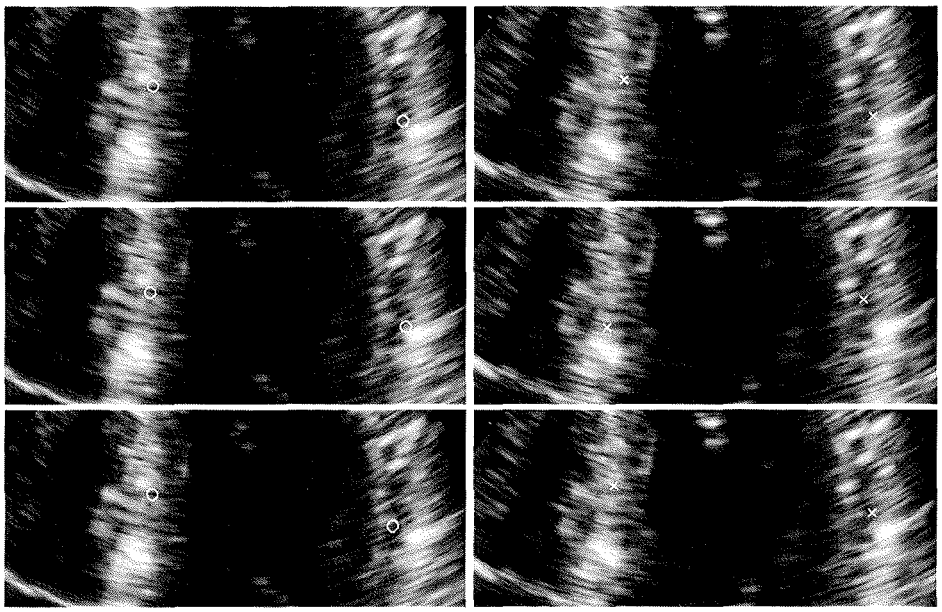

Figure A.7: A movie showing the B-mode cine-loop used in figures A.4-A.6. Six displays are shown synchronized: Original data with 40 frames per second in the left column and decimated data with 10 frames per second in the right column. Tracking results are plotted on-top of the ultrasound images for three velocity estimators: Tissue Doppler (top), speckle tracking (middle) and DAST (bottom). *Thesis comment: The movie was part of the published paper and is available at http://folk.ntnu.no/sveinbr/TviMorphingSamples/AnatomicTracking.mpg.*

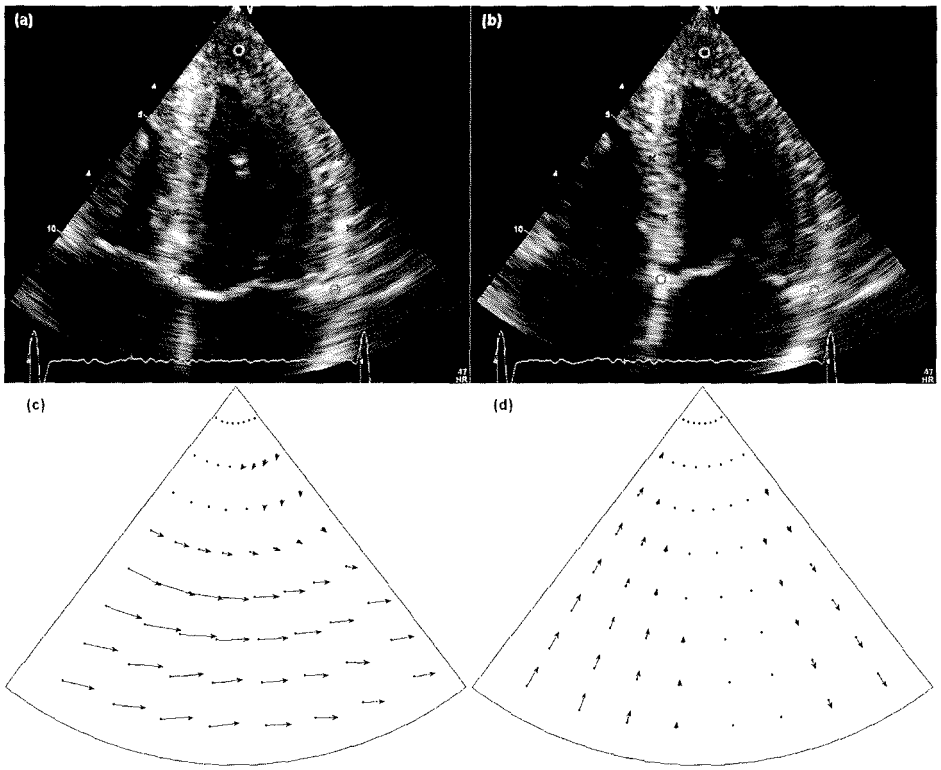

Figure A.8: Velocity field calculations based on tracking of the anatomic structure. (a) and (b) shows tracked anatomic points in the myocardium at two time points; the delay from (a) to (b) is 100 ms. Panel (c) shows the myocardium field estimate, which utilized the velocity vector in all the points marked in (a) and (b). Panel (d) shows the AV-plane velocity field estimate, which utilized only the radial displacement of the three points marked with red circles.

4.2 Velocity field estimates

Displacement fields resulting from the two last field estimates in section 3.4 are shown in figure A.8. Between the two frames shown in (a) and (b), the entire left ventricle moved laterally in the image. This motion was captured well by the myocardium field estimate, in contrast to the AV-plane field estimate, thus illustrating how much purely radial velocity measurements may differ from velocity vector measurements. In other parts of the cardiac cycle the difference between the two field estimates was less pronounced.

4.3 Image quality of morphed cine-loops

Figure A.9 shows six cine-loops in a synchronized display, all loops presenting the same recording with different processing. Panel (a) shows the original data at 40 frames per second. In panels (b) to (f), the data was decimated by a factor 4 and had frames recreated by morphing utilizing the four velocity field estimates in section 3.4, as well as with plain linear interpolation. The duplication of the AV-knots (marked AV1 and AV2 in figure A.9) was only severe in the linear interpolation case; all four morphing algorithms handled this rapid motion better. Furthermore, on-screen examination of a the slow-motion cine-loop in figure A.9 showed that the lateral motion of the septum was best handled by morphing calculated from the myocardium field estimate.

The maximal estimation error (A.19) occurred in frame 23 for all the morphing methods of the images in figure A.9. The maximal errors were: 0.1414 for the linear interpolation in (b), 0.1443 for the tissue Doppler field estimate in (c), 0.1444 for the tissue Doppler field estimate with smoothing in (d), 0.1283 for the myocardium field estimate in (e) and 0.1331 for the AV-plane field estimate in (g).

4.4 Test of diagnostic value

To achieve a frame rate of approximately 15 frames per second with integer decimation factors, the actual frame rates of the decimated data fell between 12 and 18 frames per second. The resulting decimation factors varied from 2 to 9. Wall motion scorings performed on the original data and on the morphed data are listed in table A.2. To summarize:

- 94% of the 320 segments had exactly the same score in the two cases.
- Slightly more recordings were impossible to score in the morphed data (5.3%) than in the original data (3.4%).
- In the original data, 34 of 320 segments were scored pathological. 25 of these 34 were scored pathological in the morphed data (74%)

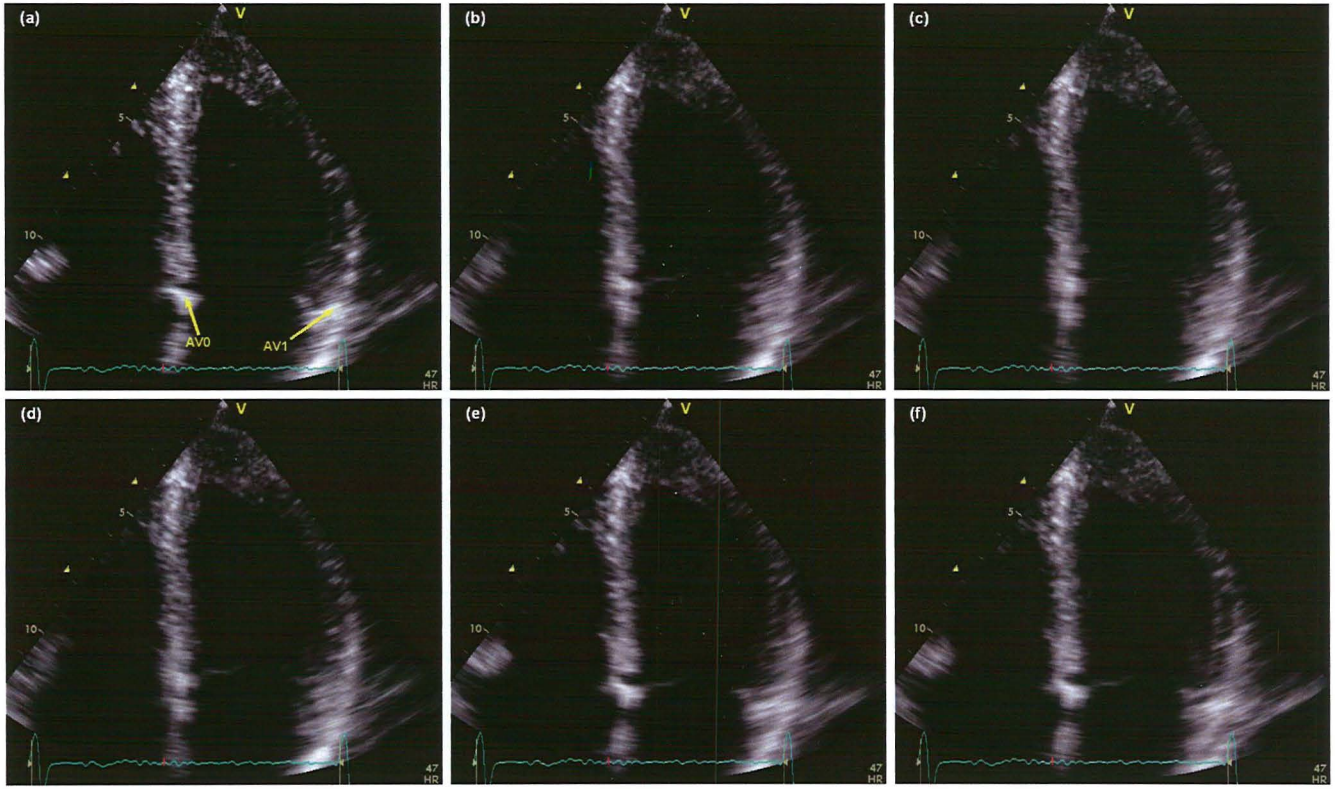

Figure A.9: A dilating left ventricle of a healthy adult person is shown in (a). A morphed replacement of this image based on a 50 ms earlier frame and a 50 ms later frame is shown for five different velocity field estimates: (b) No velocity (i.e. linear interpolation), (c) Doppler field estimate (d) Doppler field estimate with smoothing, (e) myocardium field estimate and (f) AV-plane field estimate. The media movie shows these six loop running slow motion. *Thesis comment: The referred movie was published as part of the paper and is available at http://folk.ntnu.no/sveinbr/TviMorphingSamples/six_loops_syncronized.mpg.*

Score of segments	Normal patients	Ischemic patients
1. Normal	149/147	126/126
2. Hypokinesis	2/2	14/9
3. Akinesis	0/0	17/19
4. Dyskinesis	0/0	1/0
5. Not possible to score	9/11	2/6

Table A.2: Wall motion score of 16 segments in the myocardium for 10 normal patients and 10 patients with ischemia. Format: Segments in original data/segments in morphed data.

- In the morphed data, 30 of 320 segments were scored pathological. 5 of these 30 were scored normal in the original (17%).
- No patients were scored pathological based on the original data but normal based on the morphed data, i.e. no false negatives.
- One patient was scored normal based on the original data but pathological based on the morphed data, i.e. one false positive.

5 Discussion

5.1 Local velocity estimator

Figure A.4 shows how an anatomical location in the ventricular septum was tracked throughout the cardiac cycle by the three velocity estimators tissue Doppler tracking, speckle tracking and combined tracking for a recording with 40 B-mode frames per second. The displacements curves show good agreement in both radial and lateral direction, as does the anatomically tracked path. The velocity curves shows at which points in time the tracking results separate. The drift compensation terms (A.18) applied are listed in the first column of table A.1. This term, being the distance between the start- and end point of the tracked cycle, is the accumulated estimation error of the frame-to-frame displacement estimates. Although being lowest for the tissue Doppler estimate at this location, it was low (less than 10% of the total span of the path) for all estimators. The real velocity, however, remains unknown, but examination of the anatomically tracked path plotted in a running cine-loop display gives an impression of the accuracy of the estimators. As seen in figure A.7, the accuracy seems to be good.

Figure A.5 shows corresponding curves for a location in the LV lateral wall. In this region of the myocardium, the real velocity direction normally does not lie

in the imaging plane, leading us to expect the speckle search to be less accurate as the scatterers move in and out of the imaging plane. The displacement curve derived by speckle tracking was evidently different from the tissue Doppler and DAST curves, and the applied correction term of 9.3 mm indicates inaccurate tracking. Also a sudden drop in the velocity curve in the middle of the relaxation phase indicates a large estimation error at that specific frame. Examination of the tracked location in a cine-loop display (figure A.7) confirmed that the DAST estimator followed the image better than the speckle tracking did.

Figure A.6 shows the same location as figure A.4, but with only every fourth frame used for tracking in all the estimates. In this case, it is reasonable to use the curves obtained at higher frame rates as a "correct result", and the radial displacement and velocity curves for the DAST estimator was evidently more accurate than that of the speckle tracking curves. In the lateral direction, both speckle tracking and the DAST estimator showed similar behaviour, not very different from the case with higher frame rate. It was not unexpected that pure speckle tracking had large estimation error when the frame rate got very low, because lower frame rate in the contraction and relaxation phase of the cardiac cycle implies larger deformations of the myocardium from frame to frame, and deformations may change the speckle pattern at the considered anatomical location.

A lateral up-sampling rate of $R_{lat} = 2$ was used in the calculation of the presented curves. However, experiments with rates equal to 1, 2, 3, 4 and 5 were conducted with similar results.

The conducted experiments suggest that the DAST estimator should be chosen over pure speckle tracking when calculating estimates for the velocity vector based on ultrasound recordings with low frame rate. For use in real-time 3D tissue Doppler imaging, the available acquisition rate will be in the range of those used in figure A.6, thus the DAST estimator should be a candidate for both regional analysis and image morphing.

5.2 Image quality of morphed images

In panel (c) and (d) of figure A.9, local velocity estimates from tissue Doppler measurements were utilized. On-screen examination of the running loops showed a "restless" or "turbulent" image of the myocardium, indicating that this type of velocity field estimate is not smooth enough to create valid morphings.

In panel (e) and (f) of figure A.9, velocity estimates from selected anatomical points were interpolated to a velocity field estimate for the entire frame, shown in figure A.8 at a specific frame. The interpolation between few points ensured that the velocity gradients were well controlled. Examination of the movie in figure A.9 confirmed that overall performance, when considering both radial and

lateral movements in the image, was best for the myocardium field estimate. This conclusion was also supported by the mean square error calculations, where the myocardium field estimate had lower error than the other methods. The fact that both the smoothed and non-smoothed local Doppler estimates yielded higher mean square error than plain linear interpolation (0.144 vs. 0.141) justifies the claim that the velocity gradients of the Doppler velocity estimate was too large to create useful morphings.

In the myocardium field estimate, seven control points were used to position the myocardium curve in the initial frame. The choice of the number seven corresponds to the division of the myocardium into six segments, a subdivision used in each cardiac view during wall motion scoring. More control points would have allowed for higher local variations of the velocity estimate along the myocardium curve, while fewer control points would make the calculation more computationally effective. If a small area with myocardial pathology is present, higher spatial resolution of the velocity field estimate could be required, and increasing the number of tracked control points then might be necessary to create helpful morphings.

Even though the myocardium field estimate yielded the best results in the experiments, a combination of this and the automatic AV-plane method should be feasible. One could use the detected AV-plane and apex locations to automatically position a number of control points in the first frame of the cine-loop, and secondly use anatomical tracking as described in section 3.4.3, thereby getting a fully automatic morphing algorithm which handles well both lateral and radial motion of the LV walls.

In recordings with high tissue Doppler frame rate compared to B-mode frame rate and the local velocity estimator is calculated by (A.15), the radial component of the velocity field estimate is of type 2) stated in section 2.1. Hence we expect that high accelerations in the radial direction are handled well. However, if the optimum morphed image quality is to be investigated, an implementation of (A.10) should be considered.

5.3 Test of diagnostic value

The overall repeatability of test conducted was 94%, which is similar to reported result for WMS experiments[14]. More discouraging was the poor repeatability of 64% for the hypokinetic segments (only 9 of 14 had identical scores), and that three times more recordings were impossible to score (6 rather than 2). However, since the number of observations was low, these result may be due to statistical incidence. It is possible, though, that applying the optimal velocity estimator (A.10) could have improved the overall repeatability.

5.4 Future work

Although outside the scope of this study, the following experiments, utilizing the methods presented in here, could provide valuable information about the performance of the methods:

- Simulation study in 2 and 3 spatial dimensions: How do the different local velocity estimators match the original velocity in a simulated ultrasound recording with gray-scale and tissue Doppler data?
- Morphing cine-loops by integrating the particle path as in (A.10), which is assumed to yield the best possible morphing given the velocity field estimate.

6 Conclusion

The visual quality of B-mode ultrasound cine-loops with low frame rate was improved by temporal morphing using the velocity field in the image. Two adequate estimators for the velocity field were demonstrated for apical view cardiac images: One combined tissue Doppler and speckle tracking method and one pure tissue Doppler method. Both methods gave substantial improvement in visual quality compared to standard interpolation methods. The combined method performed better for lateral motion, but was dependent on operator input, in contrast to the fully automatic tissue Doppler method.

A blinded, repeated wall motion score study showed that much of the diagnostic value was retained in decimated and morphed data, even with frame rates as low as 12-18 frames/sec. The morphing algorithm applied in this study was semi-automatic, but with potential to be extended to a fully automatic method.

References

1. S. Ali, H. Egeblad, F. Steensgård-Hansenand, K. Saunamaki, S. Carstensen, and S. Haunsø. Echocardiographic assessment of regional and global left ventricular function wall-motion scoring in parasternal and apical views versus apical views alone. *Echocardiography*, 14(4):313–320, July 1997.
2. D. Barnea and H. Silverman. A class of algorithms for fast digital image registration. *IEEE Trans Comput*, 21:179–186, 1972.

3. L. N. Bohs and G. E. Trahey. A novel method for angle independent ultrasonic imaging of blood flow and tissue motion. *IEEE Trans Biomed Eng*, 38(3):280–286, Mars 1991.

4. L. N. Bohs, B. J. Geiman, M. E. Anderson, S. C. Gebhart, and G. E. Trahey. Speckle tracking for multi-dimensional flow estimation. *Ultrasonics*, 38(1-8):369–375, 2000.

5. X. Chen, M. J. Zohdy, S. Y. Emilianov, and M. O'Donell. Lateral speckle tracking using synthetic lateral phase. *IEEE Trans Ultrason Ferroelectr Freq Control*, 51(5):540–550, May 2004.

6. J. D'Hooge, B. Bijnens, J. Thoen, F. V. de Werf, G. R. Sutherland, and P. Suetens. Echocardiographic strain and strain-rate imaging: A new tool to study regional myocardial function. *IEEE Trans Med Imaging*, 21(9): 1022–30, Sep 2002.

7. B. J. Geiman, L. N. Bohs, M. E. Anderson, S. M. Breit, and G. E. Trahey. A novel interpolation strategy for estimating subsample speckle motion. *Phys Med Biol*, 45(6):1541–1552, June 2000.

8. A. R. Groves and R. N. Rohling. Two-dimensional spatial compounding with warping. *Ultrasound Med Biol*, 30(7):924–942, July 2004.

9. J. A. Jensen. *Estimation of Blood Velocities Using Ultrasound. A Signal Processing Approach.* Cambridge University Press, Cambridge, United Kingdom, 1 edition, 1996.

10. K. Kaluzynski, X. Chen, S. Y. Emelianov, A. R. Skovoroda, and M. O'Donnell. Strain rate imaging using two-dimensional speckle tracking. *IEEE Trans Ultrason Ferroelectr Freq Control*, 48(4):1111–23, July 2001.

11. C. Kasai, K. Namekawa, A. Koyano, and R. Omoto. Real-time two-dimensional blood flow imaging using an autocorrelation technique. *IEEE Trans Sonics Ultrasonics*, 32:458–463, May 1985.

12. J. Kirkhorn, S. Bjærum, B. Olstad, K. Kristoffersen, and H. G. Torp. A new technique for improved spatial resolution in high frame rate color Doppler imaging. In *Proc IEEE Ultrasonic Symposium*, pages 1947–1950. IEEE UFFC Society, 2003.

13. J. F. Krücker, G. L. LeCarpentier, J. B. Fowlkes, and P. L. Carson. Rapid elastic image registration for 3-D ultrasound. *IEEE Trans Med Imaging*, 21(11):1384–94, 2002.

14. A. Kumar, S. Minagoe, and P. A. Chandraratna. Two-dimensional echocardiographic demonstration of restoration of normal wall motion after acute myocardial infarction. *Am J Cardiol*, 57(1):1232–1235, June 1986.

15. W. N. McDicken, G. R. Sutherland, C. M. Moran, and L. N. Gordon. Colour Doppler velocity imaging of the myocardium. *Ultrasound Med Biol*, 18(6-7):651–654, 1992.

16. J. Meunier. Tissue motion assessment from 3D echographic speckle tracking. *Phys Med Biol*, 43(5):1241–1254, May 1998.

17. M. O'Donnell, A. R. Skovoroda, B. M. Shapo, and S. Y. Emelianov. Internal displacement and strain imaging using ultrasonic speckle tracking. *IEEE Trans Ultrason Ferroelectr Freq Control*, 41(3):314–325, May 1994.

18. J. Ophir, I. Céspedes, H. Ponnekanti, Y. Yazdi, and X. Li. Elastography: A quatitative method for imaging the elastisity of biological tissues. *Ultrason Imaging*, 13:111–134, 1991.

19. B. S. Ramamurthy and G. E. Trahey. Potential and limitations of angle-independent flow detection algorithms using radio-frequency and detected echo signals. *Ultrason Imaging*, 13(3):252–268, July 1991.

20. R. Sicari. Relevance of tissue Doppler in the quantification of stress echocardiography for the detection of myocardial ischemia in clinical practice. *Cardiovasc Ultrasound*, 3:2–7, Januar 2005.

21. C. Storaa, P. Aberg, B. Lind, and L. A. Brodin. Effect of angular error on tissue Doppler velocities and strain. *Echocardiography*, 20(7):581–587, October 2003.

22. G. R. Sutherland, M. J. Stewart, K. W. Groundstrøm, C. M. Moran, A. Flemming, F. J. Guell-Peris, R. A. Riemersma, L. N. Fenn, K. A. Fox, and W. N. McDicken. Color Doppler myocardial imaging: a new technique for the assessment of myocardial function. *J Am Soc Echocardiogr*, 7:441–58, 1994.

23. A. Torp, S. I. Rabben, A. Støylen, H. Ihlen, K. Andersen, L.-Å. Brodin, and B. Olstad. Automatic detection and tracking of left ventricular landmarks in echocardiography. *Proc IEEE Ultrasonic Symposium*, pages 474–477, 2004.

24. G. E. Trahey, S. W. Smith, and O. T. von Ramm. Speckle pattern correlation with lateral aperture translation: Experimental results and implications for spatial compounding. *IEEE Trans Ultrason Ferroelectr Freq Control*, 33(3):257–264, May 1986.

25. G. E. Trahey, J. W. Allison, and O. T. von Ramm. Angle independent ultrasonic detection of blood flow. *IEEE Trans Biomed Eng*, 34(12):965–967, December 1987.

26. T. Varghese and J. Ophir. Estimating tissue strain from signal decorrelation using the correlation coefficient. *Ultrasound Med Biol*, 22(9):1249–1254, 1996.

27. C. D. Watkins, A. Sadun, and S. Marenka. *Modern image processing : warping, morphing, and classical techniques*. Academic Press Professional, 1st edition, 1993.

Volume stitching in three-dimensional echocardiography: Distortion analysis and extension to real-time

Svein Brekke[1], Stein I. Rabben[2], Asbjørn Støylen[1], Asbjørn Haugen[2], Geir U. Haugen[2], Erik N. Steen[2] and Hans G. Torp[1]
[1]Dept. of Circulation and Medical Imaging, NTNU, Trondheim, Norway
[2]GE Vingmed Ultrasound, Horten, Norway

Abstract

Three-dimensional (3D) echocardiography is challenging due to limitation of the data acquisition rate caused by the speed of sound. ECG-gated stitching of data from several cardiac cycles is a possible technique to achieve higher resolution.

The aim of this work is two-fold: it is, firstly, to provide a method for real-time presentation of stitched echocardiographic images acquired over several cardiac cycles and, secondly, to demonstrate that the geometrical distortion of the images is decreased when stitching is applied to 3D ultrasonic data of the left ventricle (LV).

We present a volume stitching algorithm that merges data from N consecutive heart cycles into an assembled data volume. The assembly is performed in real-time, making immediate volume rendering of the full volume possible. *In-vivo* images acquired with this technique are presented.

Through simulations with a kinematic model of the LV wall, geometrical distortion and volume estimation errors due to long image capture time was quantified for 3D recordings of the LV. Curves showing the variation throughout the cardiac cycle of the maximal geometrical distortion in the LV walls are presented, as well as curves showing the volume estimates compared with the true LV volume of the model.

We conclude that real-time display of stitched 3D ultrasound data is feasible and that it is an adequate technique for increasing the volume acquisition rate at a given spatial resolution. Furthermore, the geometrical distortion decreases substantially for data with higher volume rate and, for a full scan of the LV, stitching over at least four cycles is recommended. (E-mail: svein.brekke@ntnu.no)

Ultrasound Med Biol vol. 33 no 5 pp. 782-796, Apr 2007

1 Introduction

Real-time acquisition of three-dimensional (3D) ultrasound data has been an aspired goal among echocardiographers since the early 1990s. Reconstructed, non-real-time 3D echocardiography (3DE) has proved to be a clinically useful technique in estimation of volume and mass of the left ventricle (LV) [3;18] and regional motion analysis of the myocardium [4;21] and for helping in assessment of various kinds of heart diseases [13]. However, since the acquisition of reconstructed 3D data is time-consuming and the resulting images are not immediately available, the clinical use of this technique has been limited.

As the speed of sound in human tissue is close to 1540 m/s and each pulse has to propagate approximately 0.25 m of tissue in transthoracic echocardiography (when maximal depth is 12.5 cm), at most 1540/0.25=6160 pulses may be fired each second, making only 205 pulses available for each data volume if a volume rate of 30 is to be achieved. Thus, such a volume would only contain 15 beams in each direction, which can be somewhat increased by parallel beam processing (e.g., 21 beams in each direction by processing two parallel beams). This illustrates that a tough compromise between spatial and temporal resolution must be done in real-time 3DE and gated acquisition may be imperative.

Early attempts to create 3D ultrasonic images were made over 30 years ago [5]. The strategy was to create dynamic 3D cardiac data with a conventional ultrasound scanner by combining B-mode cine-loops from several different positions. Numerous contributions have later refined this technique [8]. The temporal and spatial coordinates of the different B-mode frames were used to position the frames in a four-dimensional (4D) space (time and three spatial dimensions) and a scanning scheme was applied so that the data from a sequence of cine-loops spanned a 4D region in an adequate way. The position of the B-mode frames at different times could be steered by a motor [6;12] or decided freely by the sonographer [1]; the latter technique requires a probe position registration system for optimal results. This form of 3D data acquisition can be called reconstruction and it suffers from several disadvantages: These are 1) inaccuracy of measured or calculated position of the B-mode frame in the 3D volume may create artifacts, 2) for a phased array transducer, the resolution in the elevation direction is lower than the resolution the azimuth direction, 3) heart rate variation may cause artifacts due to inaccurate synchronization between loops, 4) motion of the patient due to respiration will distort the reconstructed image, 5) long acquisition time makes the recording procedure cumbersome and vulnerable and 6) it is difficult to visualize the reconstructed data during the acquisition.

The first system capable of acquiring and displaying 3D ultrasound data in real-time was built at Duke University around 1990 [17;19]. This first generation 3D ultrasound scanner utilized a 20 $\times$ 20 elements 2D matrix transducer and

could, with its large processing capacity, process eight receive beams in parallel. In 1997, Volumetrics Medical Imaging introduced a commercial scanner with a sparsely sampled 2D matrix based on the research at Duke University [11].

Achieving sufficiently high volume acquisition rate and image quality is particularly difficult for 3D ultrasound scans covering the entire LV. Reconstructive techniques have the possibility to obtain the same combination of B-mode image quality and frame rate as two-dimensional echocardiography (2DE) and 100 frames/s is easily achievable. However, to get an acceptable out-of-plane resolution, one will have to gather a large number of cine-loops, making problems with patient motion and heart-rate variability more likely to occur.

The initial second-generation real-time 3D scanner (SONOS 7500 by Philips Medical Systems; available from 2002) utilized a fully sampled transducer array and exhibited substantially improved image quality compared with the Volumetrics scanner. The SONOS 7500 also made it possible to combine 3D data from four to seven consecutive cycles into one wide-angle pyramidal volume [20]. The data acquisition was done without visual feed-back to the operator; both the patient and the transducer position were supposed to be fixed as the scan set-up ran through a series of subvolumes, and the full data set was assembled as postprocessing in the scanner after the recording was completed. On-line visualization during acquisition of stitched volume data could potentially enhance the image acquisition process through better quality control and lower time consumption.

Echocardiographic images in general have a certain amount of geometrical distortion, caused by the motion of the cardiac structures during the acquisition of each single scan. The amount of geometrical distortion depends on the location within the scanned beam sequence and on the velocity of the myocardium at the specific time and location. At a fixed spatial resolution, stitched reconstructed ultrasound recordings exhibit higher temporal resolution than do true real-time 3D recordings. Thus, the time interval used to acquire each single subvolume is shortened and the total distance of myocardial motion during the same interval is smaller, implying that the geometrical distortion, too, is smaller. The amount of distortion present in 3D echocardiographic scans is still unexplored.

The aim of this work was, firstly, to demonstrate stitched, 3D ultrasound recordings with volume assembly and on-screen presentation performed real-time and, secondly, to present simulations that quantify the decrease of geometrical distortion and the increase in accuracy of volume measurements, caused by the higher frame rate in stitched compared with nonstitched 3D ultrasound recordings.

The text continues with four sections. The following section describes the experimental set-up, with the first part showing how stitching is applied to *in-vivo* data acquired with a matrix probe and the second part describing simulations aiming to quantify geometrical distortion present in 3D echocardiographic data.

The two subsequent sections present the results of the experiments and discusses the experimental results. Finally, the last section contains the authors' conclusions.

Notation

A brief description of the notation used in sections 2 and 3 follows.

N_i,N_j,N_k	Number of ranges, azimuth beams and elevation beams in a 3D scanning grid.
i,j,k	Range, azimuth and elevation index in a 3D scanning grid.
$\mathbf{r}$	Arbitrary 3D position.
$\mathbf{r}_{ijk}$	A 3D position in the scanning grid.
I_{ijk}	The time-gain compensated echo amplitude value at $\mathbf{r}_{ijk}$.
t	Acquisition time, with $t = 0$ corresponding to the first pulse firing time of the 3D scan.
t_m; m	Acquisition time of the mth 3D volume is t_m.
n; N	Cardiac cycle number and number of cycles in a recording. $n \in \{1, 2, \cdots, N\}$.
T_n	QRS trigger times, $n \in \{0, 1, \cdots, N\}$.
τ	Relative cycle time. $\tau \triangleq (t - T_{n-1})/(T_n - T_{n-1})$, with $T_{n-1} \leq t \leq T_n$.
M_n	The number of volumes acquired in cycle number n.
m_n	The frame number in cycle number n which corresponds to frame number m in the last cycle.
$c_n(t)$	Local stitching cost: high cost implies poor match between two specific stitched subvolumes.
C	Global stitching cost: high cost implies that some of the stitched subvolumes in a recording had a poor match.

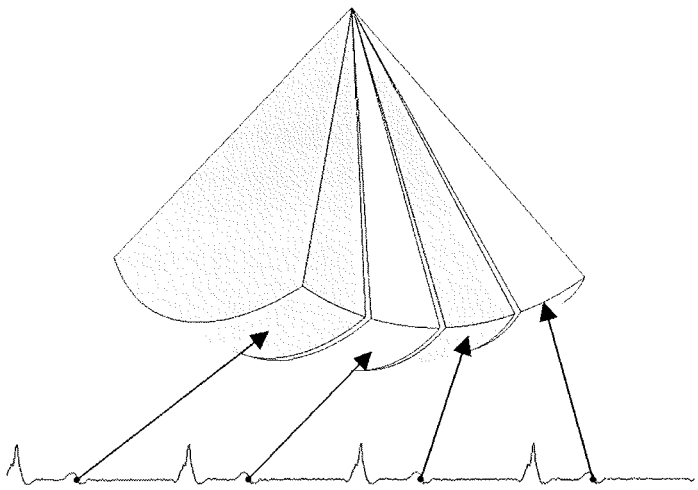

Figure B.1: Data from different scanning volumes and different cardiac cycles are assembled into a bigger, reconstructed 3D data-set.

2 Methods

2.1 Data acquisition

In the following, assembled data acquired over seperate cycles will be termed "stitched ultrasound data" (although the stitching process, in contrast to automatic creation of stitched panoramic photographs, does not include image registration in overlapping regions).

The volume to be scanned was divided into N disjointed subvolumes, N taking values between 2 and 8. One subvolume was scanned at the time and the active subvolume was changed upon QRS triggering. The geometry of the subvolumes were organized in "pyramidal slices", as shown in figure B.1, such that the union of the scanned regions constituted a symmetric pyramidal scan. Typical example was four subvolumes with an azimuth angle of 65° and an elevation angle of 16°, yielding a pyramidal volume with 65° angle in both directions. After scanning the N subvolumes during N cardiac cycles, the scanning immediately continued in the first subvolume.

The experiments were conducted with a Vivid 7 ultrasound system from GE Healthcare, utilizing the 3V matrix probe with a frequency range of 2 to 5 MHz. The volume assembly algorithm was implemented as a C++ program that ran concurrently with the scanner control program during live scanning. The operator

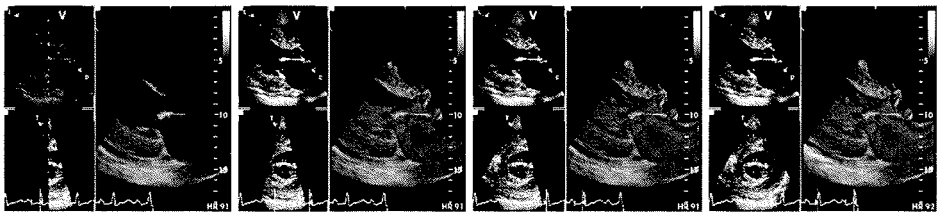

Figure B.2: One frame in each of the first four cycles of a real-time stitched scan with four subvolumes.

could enter N-cycle stitching mode with a button on the front panel of the scanner and the entire pyramidal scan volume was filled with data during the first N cycles, with N default set to 4 but being adjustable. During the first loop after entering stitching mode, the first subvolume was filled by data while the remaining $N-1$ subvolumes contained black/transparent data. After N full cycles, the entire pyramidal volume was completed, as shown in figure B.2 for a scan with four subvolumes.

Only the unstitched subvolume data were stored in the cine-loop buffer of the scanner; thus, the amount of data needed to be stored each second was the same for stitched as it was for unstitched data acquisition, making the duration of the retrospective cine-loop memory equal for the two modes.

2.2 Stitched cine-loop playback

A complete, stitched cine-loop consisted of N separate cardiac cycles, as described above. The ordered time points of the nth cycle are denoted $t_{n,1}, \cdots, t_{n,M_n}$, all $t_{n,m}$ within a cycle $[T_{n-1}, T_n\rangle$, where $\{T_n\}_0^N$ are successive QRS-trigger times defining cycles of length $\Delta T_n = T_n - T_{n-1}$. When cycle lengths varied with n, the number M_n of frames sometimes differed from loop to loop.

Cine-loop playback was performed by sequentially visualizing assembled volumes at the times $\{t_{N,m}\}$ of the last recorded cardiac cycle.

To assemble a volume at a specific time $t_{N,m}$, volume times t_{n,m_n} for $n = 1, \cdots, N-1$ needed to be determined. The following two algorithms for time alignment were implemented.

1. Stretched time, stretching the diastolic part of the time axis of each cardiac cycle. According to Mor-Avi et al. [14], the duration of the systole empirically is approximately $T_{es} = \sqrt{\Delta T} \cdot 0.343\,\mathrm{s}$, where ΔT is the length in seconds of the cardiac cycle. The normalized time $t_{norm,n}$ corresponding to $t \in$

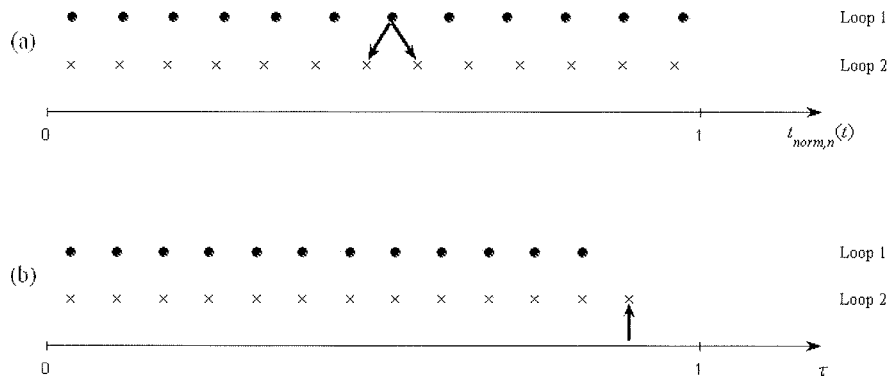

Figure B.3: Two different algorithms for temporal alignment of subvolumes when stitching cardiac cycles with different heart rate. (a) Stretched time alignment, implying that both frames 7 and 8 in loop 2 are aligned with frame 7 in loop 2, as indicated by the two arrows. (b) Abbreviated time, implying that the last frame of loop 1 is never shown (marked with an arrow).

$[T_{n-1}, T_n\rangle$ in the cycle n is calculated by

$$t_{norm,n}(t) = \begin{cases} 0.343 \cdot \frac{\tau}{T_{ES}}, & \tau \leq T_{es} \\ 0.343 + 0.657 \cdot \frac{\tau - T_{es}}{\Delta T_n - T_{es}}, & \tau > T_{es} \end{cases} \tag{B.1}$$

with $\tau = t - T_{n-1}$ being time relative to start of the cycle, ensuring that $t_{norm,n}(t)$ runs from 0 to 0.343 in the systole and from 0.343 to 1 in the diastole of the nth cardiac cycle. The subvolume in cycle n was picked at the index m_n which had stretched time $r_n(t_{n,m_n})$ closest to the stretched time $r_N(t_{N,m})$ of the last cycle, i.e., the time t_{n,m_n} that minimized $|t_{norm,N}(t_{N,m}) - t_{norm,n}(t_{n,m_n})|$

2. Abbreviated time, using only the time interval of the shortest cardiac cycle for play-back. Cine-loop display was performed by running through the times $t_{N,1}, \cdots, t_{N,\min M_n}$ and, when presenting the volume at $t_{N,m}$, setting $m_n = m$ in all cycles $n = 1, \cdots, N$.

Figure B.3 shows an example of how stretched and abbreviated alignment may differ for cine-loops with different durations.

Upon presentation of a volume at time $t_{N,m}$, the N subvolume memory blocks were copied into a larger memory block and the assembled volume data were sent to the scanner software for presentation. Thus, the volume rendering and 2D-slice displays followed the same layout and could be customized by the operator in the same manner as with ordinary 3D data.

Stitching artifacts were measured by the cost function $C(t) = \{c_n(t)\}$, where, for a particular time t and subvolume number $n \in \{1, \cdots, N-1\}$, c_n measured the stitching artifact between subvolumes n and $n+1$ by calculating the two-dimensional correlation between neighbouring image planes. Let t be given and $\rho(\phi_k)$ be the correlation between the sequences $\{I_{\cdot,\cdot,k}\}$ and $\{I_{\cdot,\cdot,k+1}\}$:

$$\rho(\phi_k) = \sum_{i,j} I_{i,j,k} I_{i,j,k+1} / \sqrt{\sum_{i,j} I_{i,j,k}^2 \sum_{i,j} I_{i,j,k+1}^2}, \tag{B.2}$$

ϕ_k being any elevation plane angle in a stitched acquisition volume, $1 \leq k \leq N_k$. For an angle ϕ' at the seam between subvolumes, one would expect $\rho(\phi')$ to be significantly lower than $\rho(\phi \neq \phi')$ if the match between the subvolumes was poor. The stitching cost used in each seam was therefore chosen to be

$$c_n = (\rho(\phi'_n) - \bar{\rho})/\sigma(\rho), \tag{B.3}$$

where $\bar{\rho}$ and $\sigma(\rho)$ are the mean and standard deviation of $\rho(\phi)$ taken over the subvolumes n and $n+1$. Different volume times t gave different values of c_n; thus, the stitching cost was actually a function $c_n(t)$ of time. The overall stitching cost for a cine-loop was calculated by

$$C = \max_t(\max_n(c_n(t)) \tag{B.4}$$

Stitching costs were calculated for both stretched time alignment and abbreviated time alignment for each cine-loop.

2.3 Real-time stitching

During acquisition of stitched 3D data, subvolume data arriving from the scanner front end were directly transferred to the internal memory of the scanner. Each time a new subvolume was available, the stitching application created an assembled volume for the same time point and the assembled volume was passed to the scanner software in the same manner as described above for cine-loop display. Hence, the layout and tuning of the visualized image was controlled by the operator through the user interface of the scanner.

Both alignment-algorithms presented in section 2.2 were implemented for live scanning, too, but with minor modifications as follows.

1. Stretched time. Since the length of the current cardiac cycle was unknown during scanning, we assumed $\Delta T_N = \Delta T_{N-1}$.

2. Abbreviated time. When scanning a subvolume at time $t_{N,m}$, it was aligned with the subvolume at $t_{n,m}$ in each of the cycles $n = 1, \cdots, N-1$. If any cycle had fewer subvolumes than m, the last time stamp t_{n,M_n} was used, i.e. setting $m_n = \min(M_n, m)$.

In both algorithms, any missing data due to insufficient scan time were filled with black. Hence, when scanning was started, the first cycle showed an image with only a fraction $1/N$ of the total volume filled with data..

Data assembly was performed as the initial step in the rendering operation and only unstitched data were stored in the cine-memory of the scanner. It was thus possible retrospectively to visualize any scanning state in the entire recording interval, i.e, the replay memory worked in the same manner in stitching mode as in unstitched real-time 3D mode.

2.4 Experiment A: Examination efficiency

The real-time stitching method lets the operator observe image quality and possible artifacts during live scanning, contrary to a non-real-time stitching mode. We assumed that the flexibility of arbitrary scroll-back combined with the immediate data presentation would reduce the time required to achieve a full volume scan without stitching artifacts when examining patients, particularly in difficult cases with low image quality, frequent respiration artifacts or uneven heart rate.

The examination efficiency was measured on a group of 12 patients participating in a training program after heart failure. The echocardiographic examinations were approved by the ethical committee of the hospital. The age of the four women and eight men was 74 ± 7.8 years, four had atrial fibrillation and one had a pacemaker. The recordings were performed without breath-hold.

Two different examination methods were compared: these were post-processed stitching and real-time stitching, denoted PP-stitching and RT-stitching, respectively. RT-stitching was performed as described in section 2.3. PP-stitching could be carried out on the same system as well: when a dedicated button was pressed, the scanner entered real-time stitching mode, but with the real-time display turned off. After N+1 cycles of scanning, the scanner automatically entered cine-loop mode and stored the resulting recording.

Both examination methods were conducted on each patient and the time to achieve recordings with good image quality was measured for the two methods. The echocardiographer decided when the image quality of recordings was sufficiently high, concidering the general image quality obtained for the patient and the patient's physical condition. The order of the methods was altered for each

patient, ensuring that six patients were examined with RT-stitching first, then PP-stitching, while the other six patients were examined with PP-stitching first, then RT-stitching.

2.5 Experiment B: Simulations based on a kinematic model

A kinematic model[16] of the LV was used to generate synthetic data. The model consisted of two confocal semiellipsoids defining the outer and inner walls of the LV. The model described the 3D deformation of the myocardium throughout a cardiac cycle as a continuous function of time. The deformation of the model at a specific time t was the sum of two different deformation modes, deformation of shape, $\mathcal{S}$, and twist, $\mathcal{T}$. (Both longitudinal deformation, radial deformation and circumferential deformation were incorporated in $\mathcal{S}$.) Starting with a point $\mathbf{r}(t_0)$ at QRS trigger, the location to that point can be tracked forward at any time $t > t_0$:

$$\mathbf{r}(t) = \mathcal{T}_t(\mathcal{S}_t(\mathbf{r}(t_0))) \tag{B.5}$$

Both deformation modes were 1-1 mappings; thus, the location $\mathbf{r}(t)$ could be tracked backward as well by

$$\mathbf{r}(t_0) = \mathcal{S}_t^{-1}(\mathcal{T}_t^{-1}(\mathbf{r}(t))). \tag{B.6}$$

The deformation modes were furthermore periodic, with the period T_{model} corresponding to the length of the cardiac cycle; $\mathbf{r}(t+T_{model}) = \mathbf{r}(t)$. The calculations of $\mathcal{S}_t$ and $\mathcal{T}_t$ for a given location were performed in the prolate spheroidal coordinate system: see Rabben et al.[16] for details. The parameter values of these transforms were adapted to a large number of semiautomatically generated contours in M-mode images[15].

An artificial 3D ultrasonic scan was generated by simulating beam propagation in a realistic volumetric scan pattern. The echo-values along each single beam were calculated by intersecting the simulated beam with the kinematic model, as shown in figure B.4. One volumetric scan consisted of N_k scan planes, each with N_j beams sampled in N_i locations along the beam. The N_jN_k beams of the scan were assigned individual pulse firing times $\{t_{m,jk}\}$ with interpulse delay $T_P = 2D/c$, where $D = 12.5$ cm was the depth of the simulated scan and $c = 1540$ m/s was the speed of sound, yielding an upper limit of $1/T_P = 6160$ Hz for the pulse repetition frequency. Each simulated data volume was scanned plane-by-plane, corresponding to the following sequence of indices (j, k):

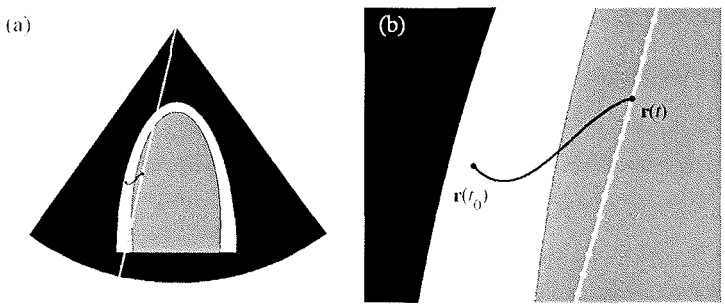

Figure B.4: Simulating an ultrasound scan by sampling individual beams from a kinematic model. (a) A slice of the pyramidal volume constituting one azimuth scan plane. (b) A magnified segment of (a). The gray-scale value $I(\mathbf{r}, t)$ sampled at time t in a point $\mathbf{r}(t)$ was calculated in two steps: 1) tracking $\mathbf{r}(t)$ backwards to $\mathbf{r}(t_0)$ and 2) sampling a static model consisting of two confocal ellipsoids at the position $\mathbf{r}(t_0)$. The volume lying between the ellipsoids is marked white and models the LV wall.

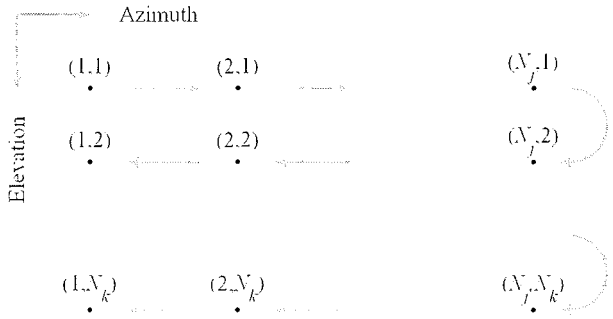

The resulting data volume was tagged with time $t_m = \text{mean}_{jk}(t_{m,jk})$, the mean pulse firing time of the transmitted beams.

Each 3D location $\mathbf{r}_{ijk}$ in the acquisition grid was tracked backwards from the beam time $t_{m,jk}$ using (B.6), resulting in a point $\mathbf{r}_{m,ijk}$ in the model space. The simulated echo value $I_{ijk}(t_m)$ was assigned a value depending on the position of $\mathbf{r}_{m,ijk}$ relative to the model (corresponding to $\mathbf{r}(t_0)$ in figure B.4):

- 0 if outside the outer ellipsoid or below the center of the ellipsoids;
- 1 if inside the inner ellipsoid and above the center of the ellipsoids, i.e., inside the LV;

Scanned cycles	Planes in subvolume	Sequence length	Volumes/s
1	36	210 ms	4.8
2	18	105 ms	9.5
3	12	70 ms	14
4	9	53 ms	19
6	6	35 ms	29
8	4.5	26 ms	38

Table B.1: Resulting acquisition rate for a volumetric scan for different stitching configurations, using a volumetric scan with 36 by 36 transmitted beams.

- Gray-scale value between 2 and 255 if between the ellipsoids and above the center of the ellipsoids, i.e., in the left ventricular wall. The gray-scale value was chosen from a 3D texture similar to a speckle pattern.

After completing the scan of one data block, the scan of the next block was started immediately; thus, $t_{m+1,1,1} = t_{m,N_j,N_k} + T_P$.

Synthetic data corresponding to a full volumetric scan of the LV was generated for six different configurations listed in table B.1. All simulations used a scan depth of 12.5 cm, yielding 6160 pulse firing per second, and a scan grid of 36 by 36 transmitted beams was utilized (assuming that adequate combinations of higher beam density and parallel beam processing would give similar results).

2.6 Volume measurements

The volume of the LV cavity in the simulated data sets described in section 2.5 was calculated by summing the volume elements corresponding to each sample position in the scan

$$\hat{V}_{cav}(\tau_m) = \sum_{n=1}^{N} \sum_{\mathbf{r} \in I(t_{n,m})} V(\mathbf{r}), \tag{B.7}$$

where $I(t_{n,m})$ was the set of points $\mathbf{r}_{ijk}$ of the subvolume scan-grid at time $t_{n,m}$ lying inside the LV cavity (i.e., in the gray area of figure B.4) and $V(\mathbf{r})$ was calculated as shown in the Appendix.

The volumes $\hat{V}_{cav}$ calculated by (B.7) and thus resulting from a realistic scan-pattern were compared by the true LV cavity volume curve of the model: $V_{cav} = \frac{1}{2} \cdot \frac{4}{3}\pi a_i(t)^2 b_i(t)$. The semiaxes $a_i(t)$ and $b_i(t)$ corresponded to the inner radius of the atrioventricular annulus and the distance from the AV-plane to the inner LV wall at apex.

2.7 Geometrical distortion

When scanning volumetric ultrasound data, the acquisition time of each volume generally is higher than in B-mode scanning. The on-screen presentation of one acquired volume normally neglects the time difference between individual beams within the scan. Thus, the shape of the imaged object as it appears on the screen is not exactly equal to the true shape, since the different beams were captured at different times, a phenomenon we call "geometrical distortion" of the image. The amount of geometrical distortion strongly depends on the amount of time used to acquire a single subvolume, and is thus lower for stitched ultrasound volumes than for volumes obtained in real-time by scanning the same spatial grid.

In simulated volumetric scans performed as in section 2.5, the geometrical distortion may be calculated in each image location. The simulated echo $I_{ijk}(t_m)$ appearing in the image to be sampled in location $\mathbf{r}_{ijk}$ at time t_m is really sampled in that location at time $t_{m,jk}$. If we let $\bar{\mathbf{r}}(t)$ be the path of a scatterer in the target, passing through $\mathbf{r}_{ijk}$ at the time $t_{m,jk}$ so that $\bar{\mathbf{r}}(t_{m,jk}) = \mathbf{r}_{ijk}$, then $\xi_{ijk}(t_m)$ is the simulated echo of this scatterer. At the time t_m that was assigned to the data volume, the same scatterer was at a different position $\bar{\mathbf{r}}(t_m)$. The vector

$$\mathbf{d}(t_m, \mathbf{r}_{ijk}) \triangleq \bar{\mathbf{r}}(t_m) - \mathbf{r}_{ijk} \tag{B.8}$$

thus represents the difference between the position where I_{ijk} was captured and the position where it was presented. Hence, the maximal relative displacement of any two locations in the LV wall can be measured by

$$d_{max}(t_m) \triangleq \max_{\mathbf{r},\mathbf{r}' \in J(t_m)} |\mathbf{d}(t_m, \mathbf{r}) - \mathbf{d}(t_m, \mathbf{r}')| \,. \tag{B.9}$$

The maximum was taken over all pairs of points being the set $J(t_m)$ of grid points lying inside the LV walls (i.e., the white area in figure B.4). The quantity $d_{max}(t_m)$ was used as a measure of the geometrical distortion of a volume acquired at relative time t_m.

In a stitched scan, we still define d_{max} by (B.9), but with the maximum taken over $J(\tau_m) \triangleq \cup_{n=1}^{N} J(t_{n,m})$, i.e., all grid points in the assembled volume lying inside the LV walls. Thus, the geometrical distortion at relative cycle time τ_m in a stitched scan was measured as the maximal difference between local distortion vectors in any two LV locations in the assembled data volume.

Even though the times τ_m for which d_{max} are defined in a real scan would be restricted to the volume acquisition times in the scan, the value $d_{max}(\tau)$ obtained in a simulation could be calculated for arbitrary $\tau \in [0, T_{model})$, by adding an initial delay $\Delta\tau$ before the first pulse firing in each subvolume.

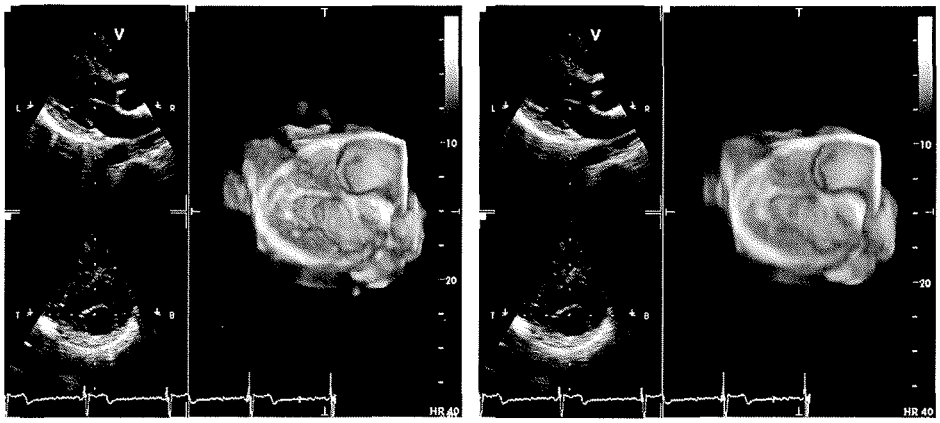

Figure B.5: A stitched scan acquired over four cycles presented in two ways. At full resolution (left) and decimated by a factor two in both azimuth and elevation direction (right). The decimated image would be possible to acquire without stitching.

3 Results

3.1 Real-time stitching and cine-loop display

The gain in spatial resolution for stitched over unstitched images was evident. Figure B.5 shows the impact of stitching on the spatial resolution, the scan region and volume acquisition rate being held constant. The left image in figure B.5 is a $63° \times 63°$ stitched scan acquired over four cycles with 19 volumes per second. In the right image, the data were down-sampled with a factor two in each scan direction, thus resulting in a data set that would be possible to acquire in real time.

Image artifacts were likely to occur in some patients, while other patients hardly showed artifacts at all. Artifacts were readily visible to the sonographer as misalignments in the B-mode view, see figure B.6 and figure B.7, and were mainly of two kinds as follows. 1) Respirational artifacts. Some patients were not able to hold their breath and most respirations lead to artifacts. Figure B.6 shows a four-cycle stitched recording with evident respiration artifact in the systole. 2) Uneven heart rate. Recordings with large difference $T_{max} - T_{min}$ between the longest and shortest cardiac cycle showed artifacts. Reconstructed with abbreviated time alignment, the last frames were likely to be hidden for some of the subvolumes, while reconstructed with stretched time, one or more frames in the diastole were likely to be misaligned. Figure B.7 presents a four-

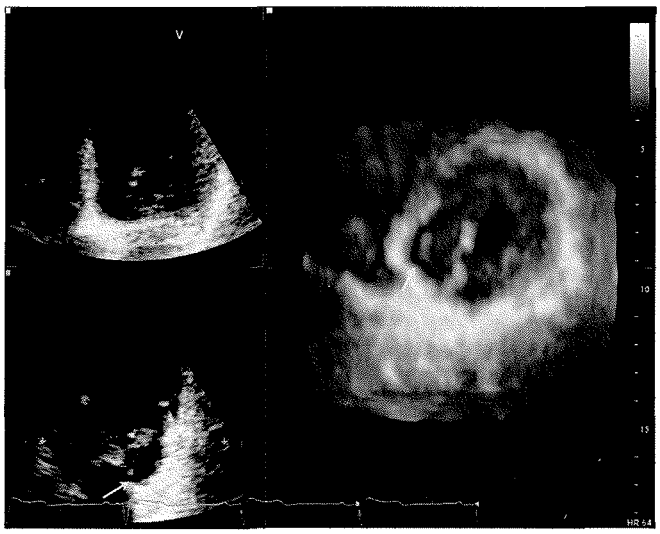

Figure B.6: A four-cycle stitched cine-loop with a stitching artifact in the middle seen due to respiration. The same artifact is marked with an arrow in both the elevation slice-view (lower left) and the volume rendering (right). Movie available at http://folk.ntnu.no/sveinbr/StitchingSamples/StitchingRespArtefact.mpg.

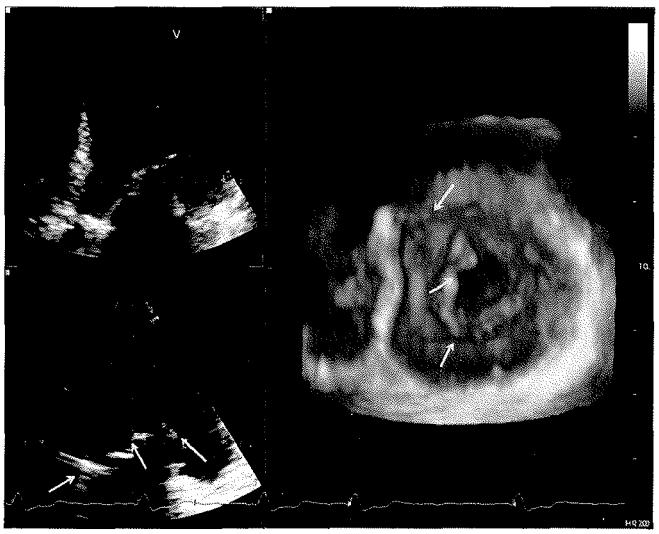

Figure B.7: A four-cycle stitched cine-loop with artifacts due to uneven heart rate. The patient suffered from atrial fibrillation and four consecutive cycles that were well aligned were difficult to find. There are artifacts in all the three seams (marked with arrows). Movie available at http://folk.ntnu.no/sveinbr/StitchingSamples/StitchingHRArtefact.mpg.

		1	2	3	4	5	6	7	8	9	10	11	12
RT	Time [s]	82	72	54	46	46	69	150	119	195	60	77	29
	Cost C	41.5	13.1	6.7	4.1	21.9	6.1	6.0	8.6	8.9	3.8	25.3	8.4
PP	Time [s]	29	180	26	125	30	186	242	136	77	113	83	23
	Cost C	18.6	6.1	6.1	7.8	27.3	4.8	18.7	3.2	14.3	6.6	18.0	12.0
Order		R,P	P,R	R,P	P,R	R,P	P,R	R,P	P,R	R,P	P,R	P,R	R,P

Table B.2: Examination time and the resulting stitching cost for two different stitching methods, real-time stitching (RT) and postprocessed stitching (PP). Order P,R means that postprocessed stitching was performed first; R,P means that real-time stitching was performed first.

cycle stitched recording, showing artifacts due to uneven heart rate, with M_n varying from 22 to 30.

Alignment artifacts were more readily visible in a dynamic computer display than in printed images. Movies showing the cine-loops of figure B.6 and figure B.7 are available on-line[2].

The local stitching cost function $c_n(t)$ and the overall stitching cost C as defined in (B.3) and (B.4) were calculated for all recordings. A high value of $c_n(t)$ indicates a poor match between subvolumes from loops n and $n+1$ when assembling volume data for time t. The calculation of $c_n(t)$ from $\rho(\phi)$ is illustrated in the left columns in figure B.8, where $\rho(\phi)$ is plotted as a function of elevation angle ϕ for a single frame in three different cases: These were no visible stitching artifacts, small but visible stitching artifacts and severe stitching artifacts. The elevation angle at the stitches are marked with vertical lines and one can, in the two lower rows of figure B.8, see that a substantial drop in ρ was present when the assembled volume had a stitching artifact. Careful examination of 3D images and their corresponding ρ-curves confirmed that drops in $\rho(\phi)$ generally coincided with visible stitching artifacts. Letting $c_n(t)$ be the number of standard deviations of the ρ-drop at the seam of subvolumes n and $n+1$, the amount of stitching artifacts throughout a cine-loop can be plotted, as shown in the right column of figure B.8. The local cost functions resulting from both stretched time alignment (solid lines) and abbreviated time alignment (dashed lines) are shown and the difference in stitching cost for the two methods was small in these three cases.

The overall cost C for each recording was assigned the highest maximal value of the local cost, $C = \max_t \max_n c_n(t)$, which was 6.7 for the recording without artifacts, 14.5 for the one with minor artifacts and 41.5 for the one with severe artifacts.

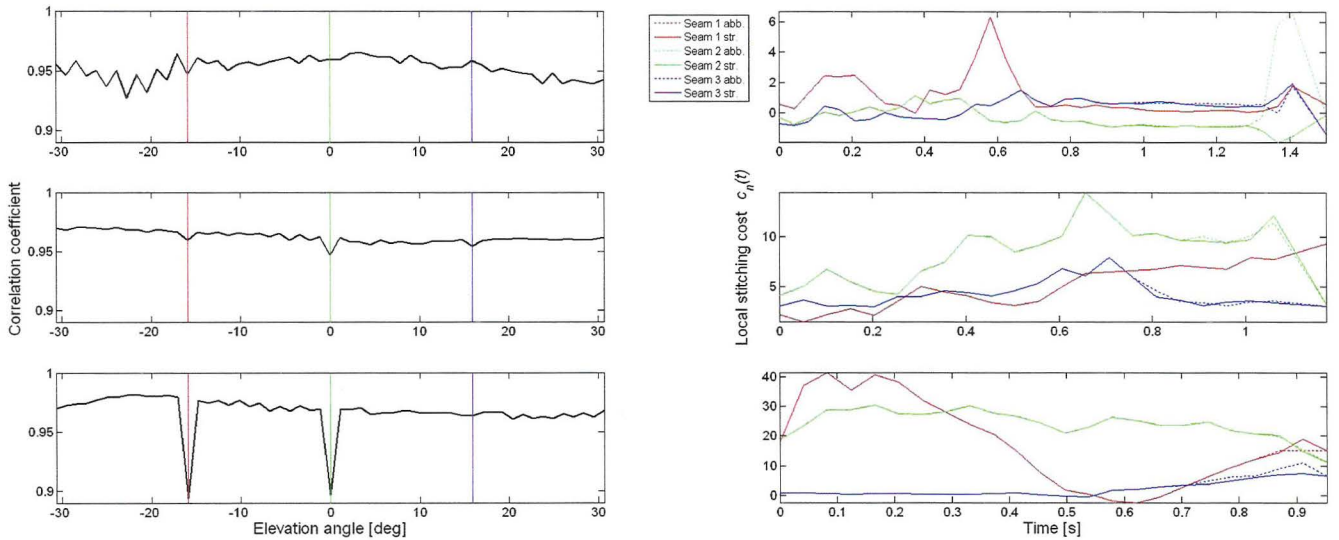

Figure B.8: Correlation plots for three different recordings: No visible stitching artifacts (top row), moderate stitching artifects (middle row) and severe stitching artifacts (bottom row). The plots on the left side shows cross correlation $\rho(\phi)$ between neighboring elevation planes as a function of elevation angle ϕ, plotted at one single time. The plots on the right side show local stitching cost $c_n(t)$ at the joint between subvolumes, shown as a function of time throughout a cine-loop (solid lines: stretched time alignment; dashed lines: abbreviated time alignment). Each drop in $\rho(\phi)$ in the left-most plots correspond to a value of c_n at a specific time point in the right-most plots.

3.2 Experiment A: Examination time

Examination times for the patients are listed in table B.2. Examination time for real-time stitching was 83 ± 48 s and for postprocessed stitching, 105 ± 72 s. One can observe that both the mean and the standard deviation was lowest when applying real-time stitching, but the mean was not significantly lower ($p = 0.2$ using a t-test of one-sided larger mean, no assumptions on the two standard deviations).

The maximal stitching cost C as defined in (B.4) was calculated for each patient, both from the recording with postprocessed stitching (P-recording) and the recording with real-time stitching (R-recording). The value of C varied substantially between recordings, with the mean value of C for the best R-recordings being slightly higher than that of the best P-recordings, 12.9 ± 11.3 and 12.0 ± 7.4 respectively. The maximal stitching costs for the recordings are listed in table B.2.

3.3 Experiment B: Simulated ultrasound data

Figure B.9 shows simulated data of relative time $\tau = 0.5$ s for two different cases: these are an unstitched scan and a six-cycle stitched scan. The geometrical distortion due to the long acquisition duration has induced an evident asymmetry in the unstitched data-set (left panel), while the stitched data-set (right panel) shows better symmetry and hence better agreement with the model. A synchronized cine-loop display of the data in figure B.9 is available on-line [2].

3.4 Volume measurements

Automatic volume measurements were performed for all the scan-configurations listed in table B.1. During the experiments, it became evident that the results of the volume measurements depended on the orientation of the scanning region relative to the simulation model. Therefore, results from two different orientations are presented: these were LV axis parallel to the probe direction and LV axis deviating 20° from the probe axis. The development throughout the cardiac cycle of the true LV cavity volume V_{cav} and the measured LV cavity volume $\hat{V}_{cav}$ calculated by (B.7) for an unstitched scan and a four-cycle stitched scan is shown in figure B.10 for both on-axis scanning and 20° off-axis scanning.

Table B.3 lists the peak deviation of $\hat{V}_{cav}$ from V_{cav} for an on-axis scan using all the scan configurations in table B.1. We see that the average estimation error is small in all the listed cases.

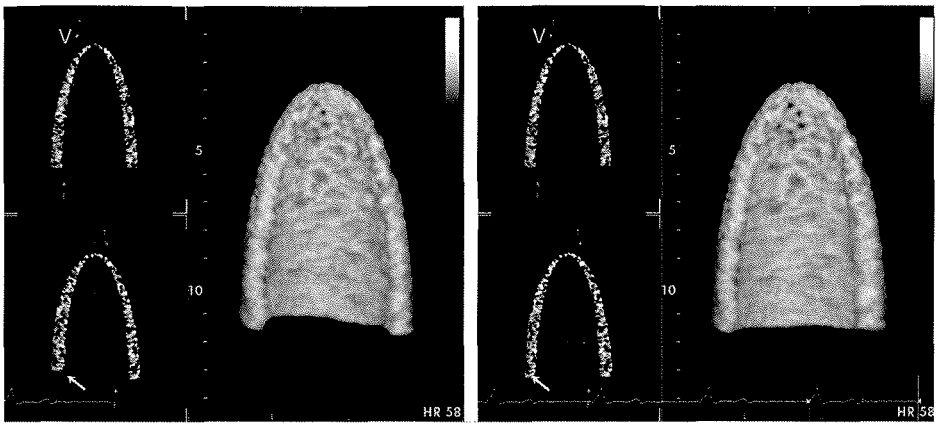

Figure B.9: Simulated ultrasonic images of the left ventricle, using a volumetric scan with 36 by 36 transmitted beams. Left panel: real-time scan. Right panel: six-cycle, stitched scan. The model used in the simulations was perfectly symmetric, while the elevation slice of the simulated images were asymmetric due to geometrical distortion (the arrows show locations with a large distortion vector). Movie available at http://folk.ntnu.no/sveinbr/StitchingSamples/StitchingSimDual.mpg.

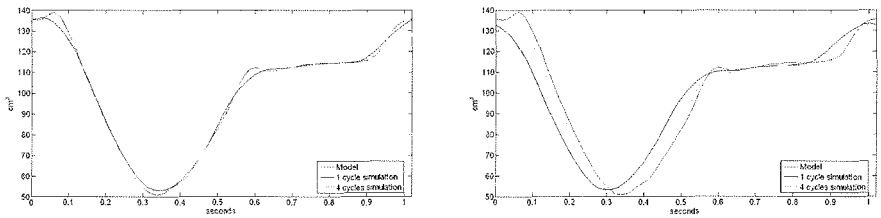

Figure B.10: Curves showing the development of LV cavity volume V_{cav} (red lines), $\hat{V}_{cav}$ resulting from an unstitched scan (blue lines) and $\hat{V}_{cav}$ resulting from a four-cycle stitched scan (green lines). Left panel shows results obtained when LV axis were parallel to the probe axis; right panel, when LV axis had angle 20° to the probe axis.

Number of cycles	Mean ± std	Min	Max
1	0.3 ± 1.9	-4.3	4.6
2	0.1 ± 0.6	-1.6	1.3
3	0.0 ± 0.3	-0.9	0.7
4	0.0 ± 0.2	-0.6	0.5
6	0.0 ± 0.1	-0.3	0.3
8	0.0 ± 0.1	-0.3	0.4

Table B.3: Mean, standard deviation and peak deviation within the cardiac cycle of the fractional difference between estimated LV cavity volume$\hat{V}_{cav}$ (i.e., measured by accumulating volume elements in a simulated on-axis scan of the LV cavity) and the true model cavity volume V_{cav} of the model presented in 2.5. The numbers show estimation error in percent of true value.

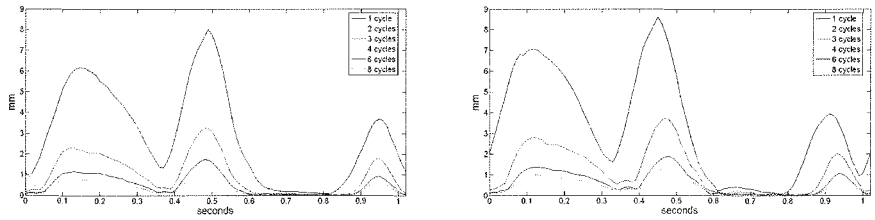

Figure B.11: Maximal geometrical distortion $d_{max}(\tau)$ for the six different configurations of table B.1. Left panel: LV axis parallel to the probe axis; right panel: LV axis had 20° angle to the probe axis.

3.5 Geometrical distortion

The geometrical distortion $d_{max}(\tau)$, see (B.8), was measured in the same two cases for model orientation as the volume measurements in section 3.4: These were LV axis parallel to the probe axis and LV axis having angle 20° to the probe axis. Curves showing the d_{max} development through the cardiac cycle for all the scan-configurations in table B.1 are shown in figure B.11. We see that the geometrical distortion is similar for the two different LV-axis angles, though slightly higher for off-axis scanning. The peak values in all cases were in the dilatation phase of the diastole, being substantial only in low volume-rate scanning (8.0 mm at 4.8 volumes/s and 5.0 mm at 9.6 volumes/s), but noticeable (> 1 mm) also in the the other cases (14-38 volumes/s).

4 Discussion

4.1 Cine-loop display with stitched images

Figure B.3 shows the subvolume alignment of a two-cycle, stitched scan with nonconstant heart rate. In this example, both the alignment schemes described in the experimental set-up lead to artifacts in the assembled volume data. When displayed with stretched time alignment, subvolume number 7 of loop 2 will be presented two successive times in the cine-loop (both when frame 7 and frame 8 of loop 1 are presented); thus, only half the image changes when stepping from frame 7 to 8. When abbreviated time is applied to the same sequence, the last subvolume of loop 1 is never displayed and the diastole is presented as having shorter duration than in reality. Side-by-side display of an *in-vivo* cine-loop, presented with both alignment-schemes, is available on-line [2]. Note that, in either alignment scheme, the synchronization is best at the first frame and degrades towards the end of the cycle.

4.2 Real-time stitching

The ability to display the stitched 3D data during the data acquisition, with both 2D slice display and volume rendering, proved to be a valuable tool for the sonographer. By examining the elevation B-mode view (e.g., bottom left image in figure B.7), artifacts could be monitored during live scanning. Also, during probe motion or probe positioning, the sonographer could control the artifacts by monitoring the elevation B-mode view.

In cases where the patient had arrhythmias during the image acquisition, the assembled cine-loops always showed major stitching artifacts. Thus, stitching is not an adequate technique for investigation of arrhythmias.

Due to to the long aquisition time of a full assembled data set, respiration artifacts were more likely to occur in stitched cine-loops than in unstitched cine-loops. Therefore, the gain in spatial and temporal resolution achieved by stitching should, in each recording situation, be weighed against the difficulty of capturing artifact-free data.

4.3 Experiment A: Examination efficiency

There was no significant trend showing improved performance of RT-stitching over PP-stitching, either of lower time consumption or of lower stitching cost (see figure B.8 and table B.2). Reasons for this could be that image quality and heart rate variability were very different among the 12 patients and that the recording conditions could vary distinctively from time to time, even within the examination period of one patient. Furthermore, with RT-stitching, more data were available for the examiner when deciding which cine-loop to archive, implying that more time was needed for review of the available loops. This extra time consumption might (or might not) balance the benefit of real-time quality control.

Table B.2 shows that, for all patients except patient number 7, the latter examination method was performed in shorter time than the former, suggesting that the echocardiographer "learned" the patient during the first examination, thus making the second examination more effective. Prior to the experiments, we were concerned that a learning effect might take place and, therefore, the echocardiographer was instructed to move the arm completely away from the patient between the two examinations. To cancel the learning effect from this experiment, either only one examination method should have been applied to each patient (implying the need for recruitment of more patients) or, alternatively, different echocardiographers should have performed the two examinations of each patient.

With a larger examined population, significant improvements of attained image quality and/or examination efficiency might have been possible to achieve.

4.4 Experiment B: Volume measurements and geometrical distortion

Increased accuracy for LV volume measurements with 3DE over 2DE has been demonstrated in several studies[7;9;10;18] and the fact that no assumption about LV shape has to be taken in 3DE has been assumed to be the reason for this improvement[9]. The results of the simulations listed in table B.3, showing good agreement (2%) between true LV volume V_{cav} of the model and LV volume $\hat{V}_{cav}$ calculated from simulated 3D data, are thus consistent with earlier work.

When recording volumetric data of the LV with a volume acquisition time of T_{vol} =100 ms or more, the performed simulations indicated a substantial geometrical distortion of the captured volume data compared with the imaged object. Although the distortion was slightly larger for a 20° off-axis scan than for an on-axis scan, the difference was not large, as was shown in figure B.11. Despite the geometrical distortion, volume measurements of the LV cavity were almost identical to the true cavity volume of the model when scanning on-axis. On the contrary, when scanning off-axis at low volume rate, the true and measured volume curves were not well aligned: the curve for the low volume rate scan was shifted by about 60 ms towards the left on the time axis. The reason for the better match in the on-axis scan may be that the symmetry ensures that geometrical distortion vectors **d** as defined in (B.8) has opposite directions for positive and negative time lags $t_n - t_{n,ij}$, while, in the off-axis scan, the lack of symmetry prevents the distortion vectors to add up to zero. In a real *in-vivo* scan, the perfect symmetry of the LV model will not be present and we could expect poorer agreement between measured and true LV cavity volume than was shown in figure B.10, left panel. This result indicates that special care should be taken to ensure on-axis scanning when recording 3DE data at low volume rate.

Several other factors than the investigated ones (volume acquisition time and LV axis angle relative to probe axis) may influence the resulting volume measurements and geometrical distortion as well. It is likely that, when the following factors may change, worst-case scenarios would yield considerably more distortion than in the presented simulations.

1. Asymmetric ventricle. As dysfunctional regions of the myocardium may imply asymmetric motion, the good match between $V_{cav}(\tau)$ and $\hat{V}_{cav}(\tau)$ seen in the left panel of figure B.10 may be unrealistic in many pathological cases. Hence, volume measurements based on recordings with low volume rate may imply larger estimation error than indicated even for on-axis scanning.

2. Heart rate variability. In the simulations, a fixed heart rate of 59 beats/min was used. Thus, extra geometrical distortion due to an additional per-volume delay of cycles 1 to $N-1$ would be present if the heart rate was allowed to vary between the loops.

3. Overall heart rate. A higher rate than 59 beats/min would of course decrease the number of data-volumes per cardiac cycle, but also increase geometrical distortion, since the tissue would have moved faster.

A factor that could improve the overall results is the geometric layout of the scan. Dividing the full volume into subvolumes in different ways (e.g., four or nine

symmetric subpyramids), or changing the beam sequence within each subvolume, could influence the measured volumes and/or the geometrical distortion.

5 Conclusion

Real-time display of 3D volumes assembled from data captured in several consecutive cardiac cycles has been demonstrated on an ultrasound system utilizing a 2D matrix transducer. The data were presented to the operator in the same manner as nonassembled real-time cardiac data, defaulting with two perpendicular 2D planes and a shaded volume rendering. The data from the different scanning regions were synchronized by the ECG signal. The visual feedback to the operator and the possibility retrospectively to review the entire recorded sequence and to pick N arbitrary consecutive cycles gives the echocardiographer a versatile examination tool. In addition to making subjective judgement of the stitching result possible in real-time, we propose a stitching cost function which can be used for automatic evaluation of stitching quality. These two techniques could potentially help the echocardiographer to achieve better stitched images in a shorter time, even though no significant improvement was found in a group of 12 patents with cardiac disease, compared with a system applying blind volume stitching.

A method for quantification of geometrical distortion is proposed and the amount of geometrical distortion in both stitched and unstitched scan configurations has been investigated for synthetic data generated from a kinematic model of the left ventricle (LV). For low volume-rate scanning, the geometrical distortion was readily visible in the images and it attained values as high as 9 mm. Volume measurements performed on the synthetic data showed that the estimated LV cavity volume could differ substantially from the true LV volume of the model, in particular when the volume rate was low and the LV axis was not well aligned with the scan direction. Scanning with less than 20 volumes/s is not recommended for full scans of the LV and at least four-cycle stitching should be applied.

The increased spatial and/or temporal resolution obtained by volume assembly may increase the 4D usability in many clinical applications.

Appendix

In the following, we show how the volume element size $V(\mathbf{r})$ used in (B.7) was calculated. Consider a volumetric scanning grid formed by tilting a planar sector B-mode scan around an axis through the sector apex point. A point $\mathbf{r}_{ijk}$ in the scanning grid may be indexed by the discrete spherical coordinates (r_i, θ_j, ϕ_k), where r_i is the range of the sample, θ_j is the azimuth angle and ϕ_k is the elevation

angle. Using the notation $r_{i-} = r_i - \frac{1}{2}\Delta r$ and $r_{i+} = r_i + \frac{1}{2}\Delta r$ (and correspondingly for the angles θ_j and ϕ_k), the volume element $V(\mathbf{r}_{ijk})$ in the acquisition grid was spanned by a line segment at depth $[r_{i-}, r_{i+}]$, rotated in the azimuth plane from θ_{j-} to θ_{j+}, then rotated from ϕ_{k-} to ϕ_{k+} around the tilt-axis of the scan (i.e., the axis perpendicular to the probe direction in the azimuth plane). The size of this volume element was calculated by

$$\begin{aligned} V(\mathbf{r}_{ijk}) &= \int_{\phi_{k-}}^{\phi_{k+}} \int_{\theta_{j-}}^{\theta_{j+}} \int_{r_{i-}}^{r_{i+}} (r\cos\theta d\phi)(rd\theta)dr \\ &= \frac{1}{3}(r_{i+}^3 - r_{i-}^3)(\sin\theta_{j+} - \sin\theta_{j-})(\phi_{k+} - \phi_{k-}). \end{aligned} \tag{B.10}$$

References

1. S. Berg, H. Torp, D. Martens, E. Steen, S. Samstad, I. Høyvik, and B. Olstad. Dynamic three-dimensional freehand echocardiography using raw digital ultrasound data. *Ultrasound Med Biol*, 25(5):745–53, Jun 1999.

2. S. Brekke. Image samples of real-time stitched 4D echocardiographic images, Dec 28th, 2005. http://www.ntnu.no/~sveinbr/StitchingSamples/index.html.

3. M. L. Chuang, R. A. Parker, M. F. Riley, M. A. Reilly, R. B. Johnson, V. J. Korley, A. B. Lerner, and P. S. Douglas. Three-dimensional echocardiography improves accuracy and compensates for sonographer inexperience in assessment of left ventricular ejection fraction. *J Am Soc Echocardiogr*, 12(5):290–299, May 1999.

4. M. Collins, A. Hsieh, C. J. Ohazama, T. Ota, G. Stetten, C. L. Donovan, J. Kisslo, and T. Ryan. Assessment of regional wall motion abnormalities with real-time 3-dimensional echocardiography. *J Am Soc Echocardiogr*, 12(1):7–14, Jan 1999.

5. D. L. Dekker, R. L. Piziali, and E. D. Jr. A system for ultrasonically imaging the human heart in three dimensions. *Comput Biomed Res*, 7(6): 544–553, 1974.

6. A. Delabays, N. G. Pandian, Q. L. Cao, L. Sugeng, G. Marx, A. Ludomirski, and S. L. Schwartz. Transthoracic real-time three-dimensional echocardiography using a fan-like scanning approach for data acquisition:

methods, strengths, problems, and initial clinical experience. *Echocardiography*, 12(1):49–59, Jan 1995.

7. F. M. Y. et.al. Accurate measurement of left ventricular ejection fraction by three-dimensional echocardiography. a comparison with radionuclide angiography. *Circulation*, 94:460–466, August 1996.

8. E. A. Geiser, M. Ariet, D. A. Conetta, S. M. Lupkiewicz, L. G. C. Jr., and C. R. Conti. Dynamic three-dimensional echocardiographic reconstruction of the intact human left ventricle: technique and initial observations in patients. *Am Heart J*, 103(6):1056–1065, 1982.

9. A. S. Gopal, A. M. Keller, R. Rigling, D. L. K. Jr, and D. L. King. Left ventricular volume and endocardial surface area by three-dimensional echocardiography: comparison with two-dimensional echocardiography and nuclear magnetic resonance imaging in normal subjects. *J Am Coll Cardiol*, 22(1):258–270, Jul 1993.

10. M. G. Hibberd, M. L. Chuang, R. A. Beaudin, M. F. Riley, M. G. Mooney, J. T. Fearnside, W. J. Manning, and P. S. Douglas. Accuracy of three-dimensional echocardiography with unrestricted selection of imaging planes for measurement of left ventricular volumes and ejection fraction. *Am Heart J*, 140(3):469–475, Sep 2000.

11. B. J. Krenning, M. M. Voormolen, and J. R. Roelandt. Assessment of left ventricular function by three-dimensional echocardiography. *Cardiovasc Ultrasound*, 1(1):1–12, Sep 2003.

12. I. Kupferwasser, S. Mohr-Kahaly, P. Stahr, H. J. Rupprecht, U. Nixdorff, M. Fenster, T. Voigtlander, R. Erbel, and J. Meyer. Transthoracic three-dimensional echocardiographic volumetry of distorted left ventricles using rotational scanning. *J Am Soc Echocardiogr*, 10(8):840–844, Oct 1997.

13. A. Lange, P. Palka, D. J. Burstow, and M. J. Godman. Three-dimensional echocardiography: historical development and current applications. *J Am Soc Echocardiogr*, 14(5):403–412, May 2001.

14. V. Mor-Avi, P. Vignon, R. Koch, L. Weinert, M. J. Garcia, K. T. Spencer, and R. M. Lang. Segmental analysis of color kinesis images: new method for quantification of the magnitude and timing of endocardial motion during left ventricular systole and diastole. *Circulation*, 95(8):2082–2097, Apr 1997.

15. S. I. Rabben, A. H. Torp, A. Stoylen, S. Slordahl, K. Bjornstad, B. O. Haugen, and B. Angelsen. Semiautomatic contour detection in ultrasound m-mode images. *Ultrasound Med Biol*, 26(2):287–296, Feb 2000.

16. S. I. Rabben, A. L. Haukanes, and F. Irgens. A kinematic model for simulating physiological left ventricular deformation patterns - a tool for evaluation of myocardial strain imaging. *Proc IEEE Ultrasonic Symposium*, pages 134–137, 2003.

17. O. T. V. Ramm, S. W. Smith, and H. G. P. Jr. High-speed ultrasound volumetric imaging system - part II: Parallel processing and image display. *IEEE Trans Ultrason Ferroelectr Freq Control*, 38(2):109–115, Mar 1991.

18. S. C. Siu, R. A. Levine, J. M. Rivera, S. W. Xie, J. P. Lethor, M. D. Handschumacher, A. E. Weyman, and M. H. Picard. Three-dimensional echocardiography improves noninvasive assessment of left ventricular volume and performance. *Am Heart J*, 130(4):812–822, Oct 1995.

19. S. W. Smith, H. G. P. Jr., and O. T. von Ramm. High-speed ultrasound volumetric imaging system part I: Transducer design and beam steering. *IEEE Trans Ultrason Ferroelectr Freq Control*, 38(2):100–108, Mar 1991.

20. R. S. von Bardeleben, H. P. Kühl, S. Mohr-Kahaly, and A. Franke. Second-generation real-time three-dimensional echocardiography. finally on its way into clinical cardiology? *Z Kardiol*, 93(Suppl 4):IV/56–IV/64, 2004.

21. J. Yao, Q.-L. Cao, N. Masani, A. Delabays, G. Magni, P. Acar, C. Laskari, and N. G. Pandian. Three-dimensional echocardiographic estimation of infarct mass based on quantification of dysfunctional left ventricular mass. *Circulation*, 96:1660–1666, 1997.

Tissue Doppler gated (TDOG) dynamic 3D ultrasound imaging of the fetal heart

Svein Brekke[1], Eva Tegnander[2], Hans G. Torp[1], Sturla H. Eik-Nes[2]
[1]Dept. of Circulation and Medical Imaging, NTNU, Trondheim, Norway
[2]National Center for Fetal Medicine, Trondheim University Hospital, Norway

Abstract

Dynamic three-dimensional (3D) ultrasound imaging of the fetal heart is difficult due to the absence of an electrocardiogram (ECG) signal for synchronization between loops. In this study we introduce tissue Doppler gating (TDOG), a technique in which tissue Doppler data are used to calculate a gating signal. We have applied this cardiac gating method to dynamic 3D reconstructions of the heart of eight fetuses aged 20-24 weeks.

The gating signal was derived from the amplitude and frequency contents of the tissue Doppler signal. We used this signal as a replacement for ECG in a 3D-volume reconstruction and visualization, utilizing techniques established in ECG-gated 3D echocardiography.

The reliability of the TDOG signal for fetal cardiac cycle detection was experimentally investigated. Simultaneous recordings of tissue Doppler of the heart and continuous wave (CW) spectral Doppler of the umbilical artery (UA) were performed using two independent ultrasound systems, and the TDOG signal from one system was compared to the Doppler spectrum data from the other system. Each recording consisted of a two-dimensional (2D) sector scan, transabdominally and slowly tilted by the operator, covering the fetal heart over approximately 40 cardiac cycles. The total angle of the sweep was estimated by recording a separate loop through the center of the heart, in the elevation direction of the sweep.

3D reconstruction and visualization were performed with the EchoPAC-3D software (GE Medical Systems). The 3D data were visualized by showing simultaneous cineloops of three 2D slices, as well as by volume projections running in cineloop.

Synchronization of B-mode cineloops with the TDOG signal proved to be sufficiently accurate for reconstruction of high-quality dynamic 3D data. We show one example of a B-mode recording with a frame rate of 96 frames/s over 20 seconds. The reconstruction consists of 31 volumes, each with 49 tilted frames. With the fetal heart positioned 5-8 cm from the transducer, the sampling distances were approximately 0.15 mm in the beam direction, $0.33^\circ \sim 0.37$ mm azimuth and $0.45^\circ \sim 0.51$ mm elevation. From this single dataset we were able to generate a complete set of classical 2D views (such as four-chamber, three-vessel and short-axis views as well as those of the ascending aorta, aortic and ductal arches and inferior and superior venae cavae) with high image quality adequate for clinical use.

Ultrasound Obstet Gynecol. 24(2): 192-198, Aug 2004

1 Introduction

Over the past few years there has been an increasing interest in dynamic three-dimensional (3D) imaging of the fetal heart. A full B-mode investigation may be time-consuming, requiring various insonation angles. The possibility of a retrospective offline complete analysis of the total heart acquired in a 3D block would make the evaluation of normal as well as abnormal anatomy easier [11]. By storing 3D ultrasound data from one cardiac cycle, the physician is able to do analysis offline (without the presence of the patient).

Different approaches to 3D ultrasound imaging of the fetal heart have previously been investigated. Using both gated and non-gated B-mode reconstruction techniques [14], as well as real time 3D acquisition using a 2D array transducer [6]. Several different gating techniques have been studied, including operator input based on an M-mode display [4], temporal Fourier transforms of the volume data itself [14], and Doppler spectrum acquisition and analysis performed by an independent ultrasound system [5;7]. The spatio-temporal image correlation (STIC) technique available on the VOLUSON 730 (GE Medical Systems, GE Healthcare, Chalfont St. Giles, UK), was used to produce 3D gray-scale images with the gating signal automatically detected from the underlying B-mode sequence [8;15]. 3D color Doppler images reconstructed using the STIC technique have also been presented [3;9]. Recently, 3D images of the fetal heart were obtained by free-hand scanning gated with cardiotocography (CTG) [10].

The current gating techniques have different strengths, but also limitations: The M-mode technique provides a satisfactory synchronization, but the method is manual and time-consuming. Fourier methods estimate the main heart rate well, but do not handle tracking of inter-cycle variations. The use of an additional recording device, such as the spectral Doppler or CTG technique, provides a satisfactory synchronization, but it is cumbersome, and acoustic interference between the transducers may introduce artifacts. However, the double-transducer approach has the potential for real time gating, which seems difficult to achieve with all the other methods, including STIC.

A gating signal may be utilized for 3D data reconstruction in different ways: Building a volume from B-mode slices from consecutive loops makes it possible to acquire 3D data with a standard phased array probe. Acquiring true 3D data with a 2D array transducer, assuming that a gating signal is available, makes it possible to increase the temporal or spatial resolution by grouping sub-volumes from consecutive loops into larger volumes. Ideally, the gating signal should be easy to obtain, accurate and technically reliable. In addition, in order to be clinically applicable, it should be fully automatically generated. In 3D echocardiography of children and adults, the electrocardiogram (ECG) is an ideal gating signal. For fetuses however, ECG is not easily available, and the synchronization

must be carried out in other ways.

Two-dimensional (2D) tissue Doppler is an ultrasonic mode in which the velocity of the tissue is measured on each point in a sector grid or rectilinear grid. Tissue Doppler data can be acquired simultaneously and with the same transducer as the B-mode data, allowing the recording of tissue Doppler data as part of a gated 3D scan. This would provide additional velocity information that might be utilized for synchronization.

The aim of this study was to utilize TDOG to create reconstructed, dynamic 3D ultrasound images of the fetal heart, and to evaluate the accuracy of the TDOG signal by comparing it to Doppler recordings of the umbilical artery.

2 Methods

2.1 Data acquisition

Eight pregnant women were scheduled for a regular cardiac scan, with fetuses aged 20-24 weeks. The women were informed that additional post processing would be done to develop a 3D reconstruction of the fetal heart. Several data sets were acquired for each fetus, and each data set consisted of a duplex sector scan with B-mode and 2D tissue Doppler. The scan-plane was tilted manually, making sure the heart was covered during the sweep. All recordings were over a period of 8 to 20 seconds (20-50 cardiac cycles). The B-mode image was visible during acquisition of the dataset but the tissue Doppler data was not visible.

The recordings were performed with a Vivid 7 scanner from GE Medical Systems using a 1.5D probe with a frequency range of 2-5 MHz. To find an adequate trade-off between frame rate and image quality, different B-mode scanner settings, such as transmit and receive frequencies, inter-beam distance and frame rate (frames/s), were examined. Based on the initial subjective evaluation of the clinical data, and utilizing a second harmonic setup with a transmit frequency of 2.5 MHz and a receive frequency of 5.1 MHz, an inter-beam distance of 0.3° and a data rate of 96 frames/s were decided upon. The tissue Doppler settings were adjusted to provide a small bandwidth compared to that of B-mode, but the frame size and frame rate were the same, with transmit and receive frequencies of 2.4 MHz and an inter-beam distance of 3.8°. There were three pulse firings in each beam direction of the tissue Doppler.

The gating signal was derived from clutter-filtered IQ data (complex demodulated radio frequency data): Firstly, the autocorrelation of lag one was calculated, then the imaginary part of this was averaged over each frame, before the local minima were extracted, i.e. the synchronization times were the local temporal minima of the function

$$s(t) = \mathrm{Im}(\mathrm{mean}(R_1(r, \theta, t))), \tag{C.1}$$

where the mean value was taken over all grid points (r, θ) in one tissue Doppler frame. The basic signal s is a function of time t; its value at a given time is calculated from the mean Doppler shift measured over one tissue Doppler frame.

The local minima were detected from $s(t)$, yielding the time stamps used for gating. In the parts of the 2D sequence where $s(t)$ was too weak for local minimum detection, typically in the beginning and the end of a sweep, new gating times were added using a cycle length equal to the median of the detected cycles.

2.2 Reconstruction

Reconstruction was performed with the EchoPAC-3D software product (GE Medical Systems). The program converted the B-mode scan lines into a sequence of voxel data sets, yielding a four-dimensional (4D) data set with temporal resolution equal to the B-mode frame rate and duration of one cardiac cycle, as has been done in ECG gated 3D echocardiography [1].

Ultimately, the 4D data were visualized by two standard examination techniques for 3D medical imaging:

- 2D slicing: Simultaneous scan conversion of three arbitrary planar intersections was performed from the volumetric scan-line data, and the intersections were shown in a synchronized cine-loop display.
- Volume projection: Gray-scale values for each pixel were computed as a weighted sum of all voxels projected onto each pixel in a rectangular grid, the weight decreasing with increasing distance to the plane chosen. In order to display a running loop, projections were precalculated for each frame.

2.3 Gating signal accuracy

To evaluate the accuracy of the TDOG signal, we compared it to continuous wave (CW) spectral Doppler. CW Doppler and tissue Doppler data were recorded simultaneously on two different ultrasound systems and compared. One system recorded CW Doppler data from the UA, and the other recorded B-mode and tissue Doppler IQ data from the fetal heart. The recordings were synchronized for offline analysis by simultaneously recording an independent signal (the ECG signal from an independent person) on both ultrasound systems.

The two-system recordings were performed, and the cycle lengths from the two methods were compared. The variation in time delay between upstroke readings from the spectrum and the TDOG signal was examined.

The usefulness of the tissue Doppler signal for synchronization was evaluated visually by running side-by-side consecutive cine-loops.

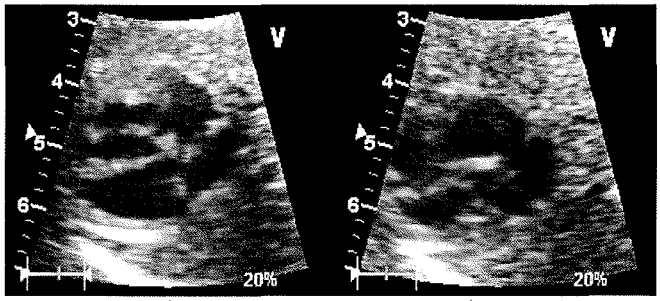

$f = 2/4.1\ MHz$
$\Delta\theta = 0.55°$
$113\,fr/s$

$f = 2.5/5.1\ MHz$
$\Delta\theta = 0.51°$
$124\,fr/s$

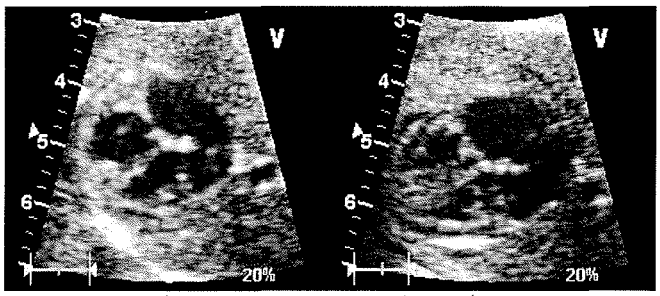

$f = 2/4.1\ MHz$
$\Delta\theta = 0.36°$
$87\,fr/s$

$f = 2.5/5.1\ MHz$
$\Delta\theta = 0.33°$
$96\,fr/s$

Figure C.1: B-mode image quality for different frequencies and beam density settings. All recordings are from the same fetus.

3 Results and discussion

3.1 Image quality

Optimal image quality of the 3D reconstruction was achieved by a compromise between high B-mode quality and high frame rate. By increasing the frequency towards the upper part of the frequency range, the lateral resolution was improved at the cost of reduced echo sensitivity.

Second harmonic imaging gave the highest lateral resolution and was used on all recordings. Figure C.1 shows how the image quality was affected for some combinations of frame rate and angular resolution for the system used in this work. A frequency of 2.5/5.1 MHz and an inter-beam distance of 0.33^o produced a good image quality in the scan plane and a relatively high frame rate at 96

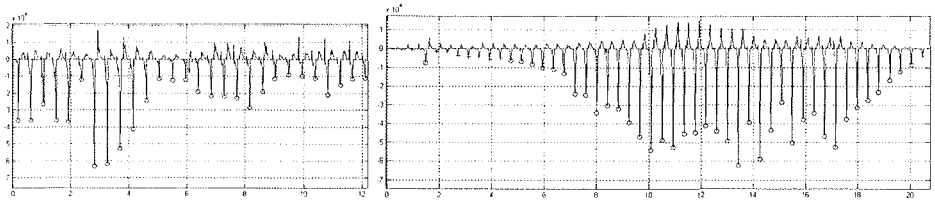

Figure C.2: The basic signal (continuous line) and the derived gating signal (circles) are shown. X-axis: time (sec.), y-axis: basic signal. The left panel shows a fixed apical four-chamber view and the right panel shows the signal for a manual sweep of 22°.

frames/s. The frame rate would have increased if the scan angle had been further decreased.

3.2 Gating signal

We recorded 2D tissue Doppler data along with the B-mode frames and calculated a gating signal based on these. The Doppler data intercepts the radial component of the motion in a slice surrounding the B-mode scan plane. Using a 1.5D probe made it possible to reduce the elevational aperture in the tissue Doppler firing, and hence increase the elevational beam width. Thus, cardiac motion could positively contribute to the gating signal, even when the motion was not visible within the B-mode image.

Comments to the choice of the basic signal s, see (C.1), for the tissue Doppler synchronization signal:

- Considering a set of IQ samples of Doppler data and the autocorrelation R_1 at lag 1, $\mathrm{Im}(R_1)$ depends both on the strength of the reflected signal and the velocity of the signal. Contribution to the mean from blood cells in s is therefore negligible, since the blood signal is much weaker than the tissue signal.

- Since s is calculated as a spatial mean value, motion towards the transducer in one part of the image will compensate motion away from the transducer in another part. Thus, uniform or massive motion produces a strong signal.

Hence, the basic signal we used emphasized strong echoes and massive motion of tissue in the ultrasound beam direction. The continuous line in the left panel of figure C.2 shows the basic signals for a fixed 4 chamber view of a fetus aged 24 weeks. Positive values of s imply that mean motion was towards the transducer,

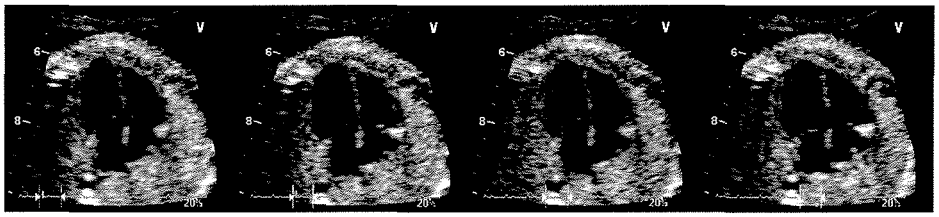

Figure C.3: Visual control of gating accuracy: Four different cine-loops from the same recording are running synchronized, based on the tissue Doppler gating signal. The snapshot is taken 50 ms after maximal relaxation, as the atrioventricular valves are closing.

Also the resulting 3D reconstructions would have artifacts if the trigger signal was very inaccurate, hence the successful reconstructions indicate the trigger signals usability.

i.e. during contraction of the myocardium. The negative values represent motion away from the transducer, and the negative peaks show the moments with the most rapid relaxation of the myocardium. We also see that the negative peaks were the most explicit events in the signal.

The gating signal was calculated as the set of local minima for s, and is marked as circles in figure C.2. The right panel shows s and the synchronization times used for a 3D reconstruction. Read from an apical recording, the minima of s in figure C.2 occured at times with the highest velocity of the dilating myocardium in diastole, producing the highest Doppler shift. By examining s immediately before the various gating times, one could possibly even detect the start of systole and of diastole from s, but this has not been addressed further here.

Since the basic signal s at a given time t depends only on the tissue Doppler frame at that time, the signal $s(t)$ is possible to produce in real time on an ultrasound system. Such a real-time TDOG signal could be useful both for workflow improvements in fetal echocardiography, and for real-time display of reconstructed 3D ultrasound images. Accuracy of the gating signal was evaluated visually by comparing consecutive loops running simultaneously and slowly side-by-side, as shown in figure C.3.

3.3 Validating tissue Doppler gating signal by comparison to CW Doppler

In both cases when Doppler CW data and tissue Doppler data were recorded, the inter-system acoustic noise was visible only if the CW beam intersected the B-mode sector. By ensuring that the distance between the transducers was not

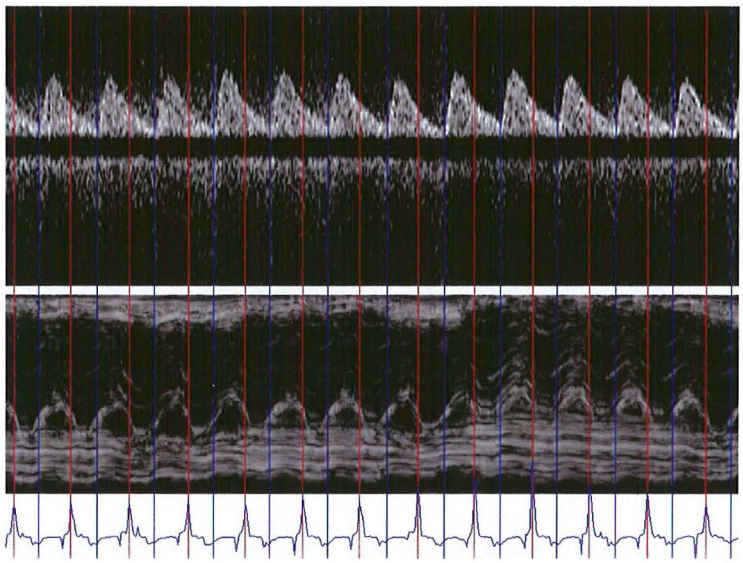

Figure C.4: Doppler CW data through the umbilical artery and M-mode data through the atrioventricular area, as well as the tissue Doppler trigger signal. The M-mode and the trigger signal were both generated from a B-mode loop with 2D tissue Doppler. The blue line shows the basic signal from which the trigger signals (red bars) are automatically generated. The blue bars show time stamps for start systole, manually selected from the spectrum.

too short, and that the CW Doppler beam did not intersect the B-mode sector, we could position the CW beam such that the noise was low. Figure C.4 shows an M-mode along a beam through the atrioventricular plane and a CW Doppler of the UA in the same time axis. The negative peak of the tissue Doppler basic signal s occurred at a moment when the atrioventricular plane moved away from the probe with high velocity.

From the spectrum data we recorded the time at the start of systole as the moment when the velocity in the UA started to increase. For the recording in figure C.4, spanning 20 cardiac cycles, we registered systole lengths 410 ± 9 ms from the spectrum, and 410 ± 8 ms from the tissue Doppler signal. The temporal resolution (i.e. the time between successive samples of the data) for the data streams were 4 ms for the spectral Doppler and 10.4 ms for the tissue Doppler, and hence the variation of the estimated cycle length was in the same order as the temporal resolution.

To calculate the difference of estimated cycle length between the two methods,

we had to decide how to align cycles to each other. As seen in figure C.4, the start of one "tissue Doppler cycle" occurs in the middle of a "spectral Doppler cycle". By comparing cycle estimates containing the same diastole for this recording, we obtained differences 0.3 ± 12 ms between the two estimates, whereas comparison of cycle estimates containing the same systole yielded 0.1 ± 10 ms, which indicates that the estimation difference occurs both in the systole and in the diastole. In both cases, the standard deviation approximately equals the temporal resolution of the tissue Doppler.

3.4 3D data acquisition

When acquiring 3D data by sweeping a B-mode scan over the heart, consecutive cine-loops become neighboring planes in the 3D data set; the number of B-mode planes in the reconstructed volume for each time step is the same as the number of cardiac cycles in the sweep. Thus, a long sweep time yields high scan plane density, but too long a sweep time makes it difficult to perform the sweep with constant tilt velocity. The usefulness of a recording depended on the following factors: no obstacles from bones or other structures in front of any part of the heart; a short distance from the heart to the probe (ideal is less than 6 cm); and no fetal or respiratory motion during the sweep time.

To cover the fetal heart with maximal diameter 2 cm at depth 5–7 cm, we used an angle of approximately 25° for both the B-mode sector and the elevational tilt. The tilt angle was estimated for each recording by comparing a cross-sectional intersection of the 3D data and a separate B-mode cine-loop scanned in the direction equal to the 3D tilt direction, see figure C.5 shows that in the presented example a tilt angle of 22° gave good agreement between the B-mode and a planar slice.

The image quality from four of the eight fetuses studied was adequate, while the results for the remaining four were poor or lacking. There were severe motion artifacts from two of the fetuses, and for the other two there was no adequate access at all to the four-chamber view during the 30 minutes each subject was available.

3.5 3D reconstruction

3D reconstructions of data were obtained from 6 fetuses (four adequate recordings and two recordings with motion artifacts).

The quality of the reconstructions varied between different recordings, mainly due to the following reasons: (1) fetal position was not suitable for high-quality B-mode imaging of the fetal heart, (2) fetus was moving during the sweep, and (3) probe motion was uneven during the sweep.

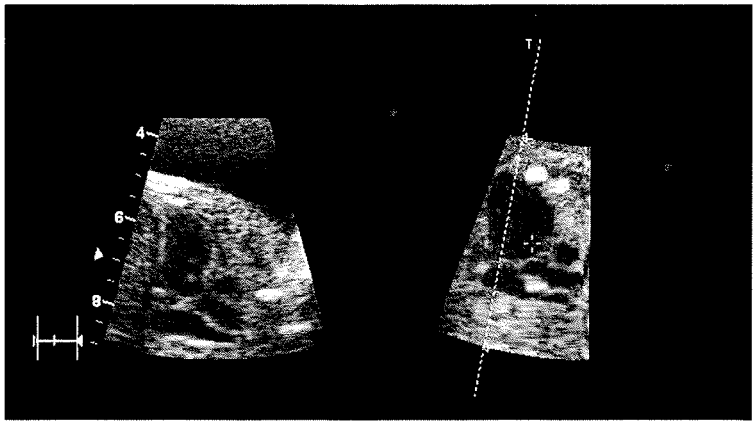

Figure C.5: The B-mode image on the left is recorded immediately after the 3D acquisition, but with the scan plane rotated 90°. The right image shows a planar intersection from the reconstructed 3D data, where the total tilt angle (input to the EchoPAC SW) and the image plane were adjusted for a best possible match between the two images. Thus, the two images show approximately the same view of the heart.

Reason (3) was not addressed in our experiments. Different methods to control reconstruction accuracy have been studied in the literature, such as magnetic position sensors [1] or a speckle decorrelation technique [13]. Furthermore, errors that may occur in position sensor systems have been corrected for by image analysis [12]. In our case, the total sweep angle was estimated by comparing the 3D data set with a separate cross-sectional B-mode recording. Hence, we expect variations in the sweep velocity to be the main concern regarding accuracy.

One example recording is presented from a fetus (figure C.6). The total recording time was 20.7 seconds, comprising 49 full cardiac cycles. The total tilt angle was estimated to 22° (based on the images shown in figure C.3), yielding an angle of 0.45° between intermediate scan planes. The volume projections shown in figure C.6 were performed in view directions corresponding to seven classical B-mode views for a fetal heart examination. Each volume projection was carried out in two steps using the EchoPAC-3D software. Firstly, transforming the scan-line data into a regular 3D grid in the viewing direction, then performing a back-to-front accumulation of voxel color with the opacity value depending on the intensity in each voxel. The software allowed the user to specify any opacity curve, and different opacity curves resulted in renderings that emphasized different aspects of the volume data. The images in figure C.6 were made with uniform

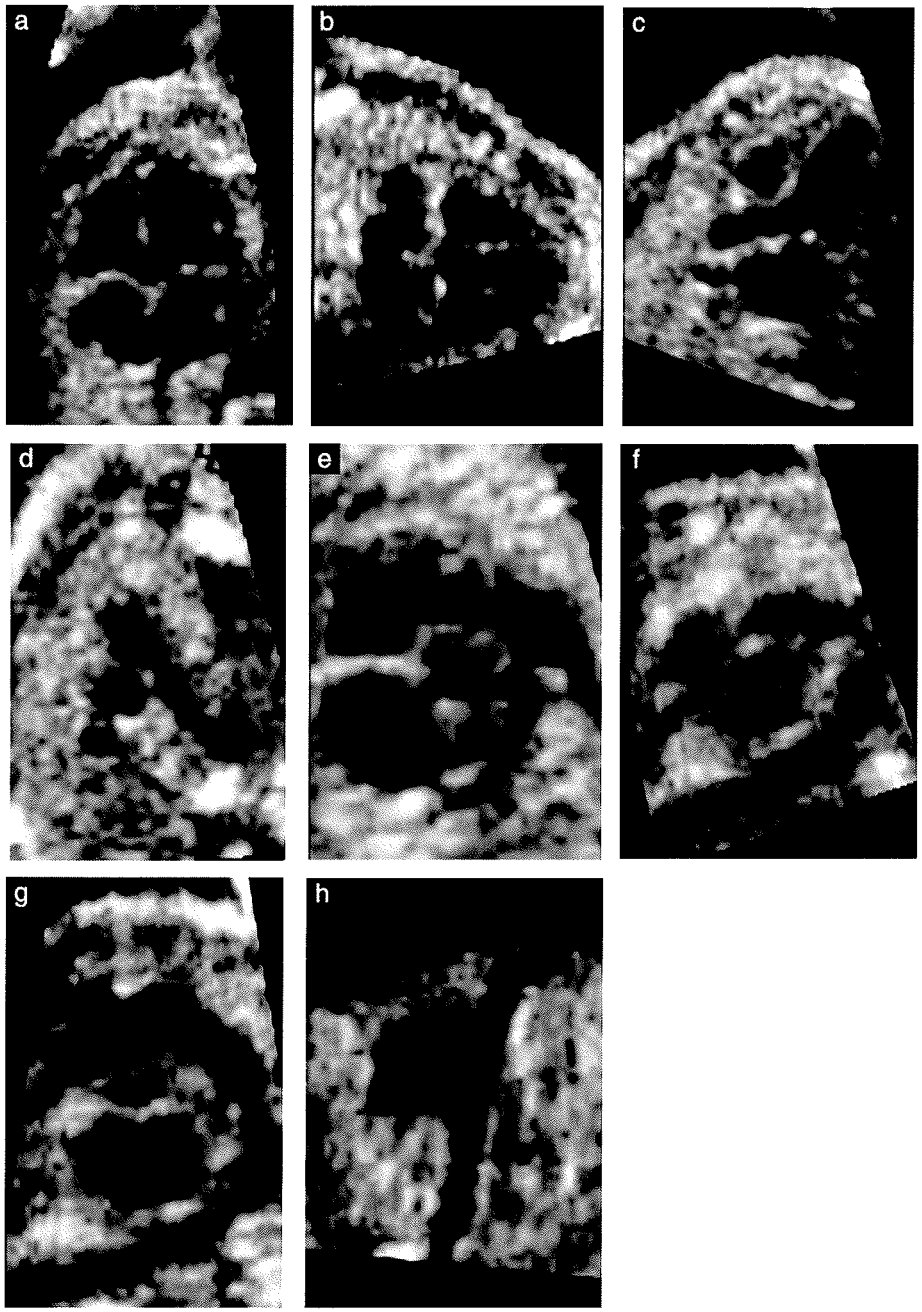

Figure C.6: Volume projections of the heart of a fetus aged 24 weeks , all images retrospectively produced from one cine-loop of 3D data, derived by apical insonation. (a) Apical four-chamber view. (b) Subcostal four-chamber view. (c) Ascending aorta. (d) Three-vessel view. (e) Short-axis view. (f) Aortic arch. (g) Ductal arch. (h) Long-axis of inferior and superior vena cavae.

opacity curve at 75%, which gave images similar to 2D slices, but the summation of voxels provided better contrast and enhancement of small structures. Images are clearer on cine-loops running on a screen than on prints [2].

In figure C.6 (a) and (b), it can be seen that apical insonation gives weak echoes from the atrial and ventricular septae. This effect is due to the nature of ultrasound backscattering, as the strength of the echoes in the septae depends both on the resolution in the imaging system and the direction of the tissue structures. This is analogous to the difference between apical and subcostal four-chamber views in ultrasound B-mode. Thus, optimal image quality of all structures cannot be achieved in one single 3D ultrasound recording, regardless of resolution.

3.6 Alternative approaches

Real time 3D ultrasound with 2D array transducers is the easiest way of acquiring 3D data of the fetal heart, but at the expense of lower temporal and/or spatial resolution. For high resolution fetal echocardiography, gated techniques like TDOG and STIC [3;8;9;15] deliver spatial and temporal resolutions that almost correspond to 2D B-mode images, but suffer from more cumbersome acquisition. Since the gating algorithm of TDOG directly detects events in the basic signal, this technique may be used to display a partly acquired data volume in real time during the acquisition phase, which might not be possible with the STIC method.

4 Conclusion

TDOG gave sufficient accurate synchronization of cardiac cycles to be used for 3D reconstruction based on tilted four-chamber view ultrasound B-mode scans.

In a dual system recording spanning 20 cardiac cycles, we found that the timing accuracy of the tissue Doppler signal was approximately the same as that of CW spectral Doppler gating, as was used by Deng et al. [5].

Free-hand sweep as a method for 3D acquisition is influenced by the operator's expertise, so this acquisition mode should be viewed as a test case for other techniques with higher spatial accuracy, such as position sensor systems or 2D array transducers. However, as demonstrated, a well performed B-mode sweep may result in a good dynamic 3D reconstruction, making it possible to obtain good visualizations of planar intersections and volume projections of the fetal heart. When performing 3D fetal echocardiography with a 2D array transducer, TDOG can be used to improve temporal resolution through assembly of subvolumes acquired over successive cardiac cycles.

This study demonstrates the feasibility of tissue Doppler gated high frame rate 3D ultrasound imaging of the fetal heart with currently available ultrasound

systems. The temporal resolution and image quality of tissue Doppler gated fetal echocardiography was similar to the STIC method [8]. In contrast to STIC however, TDOG directly detects events in the data stream, and is thus suitable for real time applications in future ultrasound systems.

Acknowledgements

Text revised by Nancy Lea Eik-Nes.

References

1. S. Berg, H. Torp, D. Martens, E. Steen, S. Samstad, I. Høyvik, and B. Olstad. Dynamic three-dimensional freehand echocardiography using raw digital ultrasound data. *Ultrasound Med Biol*, 25(5):745–53, Jun 1999.

2. S. Brekke. Dynamic 3D fetal echocardiography: Image and movie samples, Feb 3rd, 2004. http://www.medisin.ntnu.no/~sveinbr/3DFetalHeartSamples/index.html.

3. R. Chaoui, J. Hoffmann, and K. S. Heling. Three-dimensional (3D) and 4D color Doppler fetal echocardiography using spatio-temporal image correlation (STIC). *Ultrasound Obstet Gynecol*, page (in press), 2004.

4. J. Deng, J. E. Gardener, C. H. Rodeck, and W. R. Lees. Fetal echocardiography in three and four dimensions. *Ultrasound Med Biol*, 22(8):979–986, 1996.

5. J. Deng, C. F. Ruff, A. D. Linney, W. R. Lees, M. A. Hanson, and C. H. Rodeck. Simultaneous use of two ultrasound scanners for motion-gated three-dimensional fetal echocardiography. *Ultrasound Med Biol*, 26(6): 1021–1032, 2000.

6. J. Deng, I. D. Sullivan, R. Yates, M. Vogel, D. Mcdonald, A. D. Linney, C. H. Rodeck, and R. H. Anderson. Real-time three-dimensional fetal echocardiography - optimal imaging windows. *Ultrasound Med Biol*, 28 (9):1099–1105, 2002.

7. J. Deng, R. Yates, I. D. Sullivan, D. McDonald, A. Linney, W. R. Lees, R. H. Anderson, and C. H. Rodeck. Note this is picture of the month dynamic three-dimensional color Doppler ultrasound of human fetal intracardiac flow. *Ultrasound Obstet Gynecol*, 20(2):131–136, 2002.

8. G. R. Devore, P. Falkensammer, M. S. Sklansky, and L. D. Platt. Spatiotemporal image correlation (STIC): new technology for evaluation of the fetal heart. *Ultrasound Obstet Gynecol*, 22(4):380–87, Oct 2003.

9. L. F. Gonçalves, R. Romero, J. Espinoza, W. Lee, M. Treadwell, K. Chintala, H. Brandl, and T. Chaiworapongsa. Four-dimensional ultrasonography of the fetal heart using color Doppler spatiotemporal image correlation. *J Ultrasound Med*, 23(4):473–481, 2004.

10. U. Herberg, H. Goldberg, and J. Breuer. Dynamic free-hand three-dimensional fetal echocardiography gated by cardiotocography. *Ultrasound Obstet Gynecol*, 22(5):493–502, November 2003.

11. M. Meyer-Wittkopf, S. Cooper, J. Vaughan, and G. Sholler. Three-dimensional (3D) echocardiographic analysis of congenital heart disease in the fetus: Comparison with cross-sectional (2D) fetal echocardiography. *Ultrasound Obstet Gynecol*, 17(6):485–492, June 2001.

12. Z. Nieckarz, G. Taton, and E. Rokita. Geometry corrections in a rotating 3-dimensional sonographic system. *J Ultrasound Med*, 23(4):527–553, 2004.

13. R. W. Prager, A. H. Gee, G. M. Treece, C. J. C. Cash, and L. H. Berman. Sensorless freehand 3-D ultrasound using regression of the echo intensity. *Ultrasound Med Biol*, 29(3):237–46, 2003.

14. M. S. Sklansky, T. R. Nelson, and D. H. Pretorius. Three-dimensional fetal echocardiography: gated versus nongated techniques. *J Ultrasound Med*, 17:451–457, 1998.

15. F. Viñals, P. Poblete, and A. Giuliano. Spatio-temporal image correlation (STIC): a new tool for the prenatal screening of congenital heart defects. *Ultrasound Obstet Gynecol*, 22(9):380–387, September 2003.

Tissue Doppler gated (TDOG) real-time stitching in three-dimensional fetal echocardiography

Svein Brekke[1], Eva Tegnander[2], Hans G. Torp[1] and Sturla H. Eik-Nes[2]

[1]Dept. of Circulation and Medical Imaging, NTNU, Trondheim, Norway
[2]National Center for Fetal Medicine, Dept. of Ob. and Gyn.,
Trondheim University Hospital, Norwegian University of Science and Technology

Abstract

Three-dimensional (3D) fetal echocardiography is a promising technique for assessment of fetal cardiac structure and function, but suffers from lower temporal resolution than ultrasound imaging in two dimensions. Real-time, ECG-gated volume stitching is a known method in adult echocardiography, used to increase the spatial and/or temporal resolution of volumetric cardiac scans. In fetal echocardiography however, stitching has been impossible due to lack of ECG data for gating.

Method: A real-time gating signal for fetal echocardiography is suggested in this work. An ultrasound system was set up to acquire 3D gray-scale data and 3D tissue Doppler data simultaneously, with only the gray-scale data visible to the sonographer. Derived from the Doppler data, a gating signal, denoted the tissue Doppler gating (TDOG) signal, was calculated in real-time. The TDOG trigger events were used to induce changes in the geometry setup of the 3D gray-scale scan, ensuring that data from consecutive cardiac cycles were captured from separate parts of the total volumetric scan. A scan setup with six disjoint subvolumes was used, and the system could in real-time assemble and display volume data sets with data from the six most resent heart cycles.

Results: In-vivo data ware recorded from 5 pregnant women with fetuses aged 20-24 weeks, utilizing a matrix transducer with a center frequency of 3 MHz. TDOG signals from several different tissue Doppler scan geometries are presented: 5° and 10° planar sector scans and $8^\circ \times 8^\circ$ volumetric scans. Volumetric, assembled scans acquired with TDOG gated stitching are shown, and both good and poor match between subvolumes are demonstrated.

We conclude that the TDOG technique provides real-time gating of fetal cardiac cycles and it can be used to acquire stitched, 3D fetal echocardiographic data with high frame rate.

Proceeding of IEEE Ultrasonic Symposium, Vancouver BC, Oct 2-6, 2006

1 Introduction

Fetal echocardiography is, in many ways, more challenging than adult echocardiography: The dimension of the myocardium is smaller, the heart rate at rest is higher and abnormal shapes are more likely to occur.

Two-dimensional (2D) ultrasound imaging of the fetal heart is established as an important tool for prenatal diagnosis of congenital heart disease [5]. However, two-dimensional echocardiography (2DE) examinations have limitations. Firstly, when investigating a malformed myocardium, structural abnormalities may fall outside the slice-plane of recorded cine-loops and therefore the disorders may remain undiscovered. Secondly, it requires high skill for the sonographer to find the correct views when performing a 2D scan and, therefore, the quality of the recorded data may depend too much on the operator cleverness.

Three-dimensional echocardiography (3DE) applied to the fetal heart promises to address these limitations of fetal 2DE, by giving the physician full off-line access to all structures in the myocardium. This distresses the competence requirements of the sonographer and allows in a better way for second opinion judgements.

Two different data acquisition principles are available in commercial ultrasound scanners: reconstructed, 3D cine-loops with cardiac gating and real-time 3D scanning utilizing matrix transducers.

Different techniques for cardiac gating (i.e., registration of the cardiac phase) have previously been applied for reconstructed, fetal 3DE: Fourier-analysis of the image data it selves [8], spectral Doppler gating [4], cardiotocographic gating [7], spatio-temporal image correlation (STIC) [6] and tissue Doppler gating (TDOG) [1]. However, none of these methods provide a gating signal that is available in real-time during scanning, hence the 3D reconstruction can not be performed and the resulting 3D image cab not be visualized while the data are acquired.

This work extends the TDOG method introduced in Brekke et al. [1], making it possible to perform real-time, stitched scanning in a way similar to what is available for 3DE examination of the adult heart [2].

2 Methods

2.1 Real-time TDOG signal

The extraction of the gating signals is similar to, but not identical with, the signal described in Brekke et al. [1]. A Vivid7 Dimension ultrasound scanner (GE Medical Systems) was used for the experiments, utilizing a 2D matrix probe with 3 MHz center frequency. Two data streams were recorded simultaneously: 3D echo amplitude data and 3D tissue Doppler data - the latter was only used to create a gating signal and was not visible to the user during scanning.

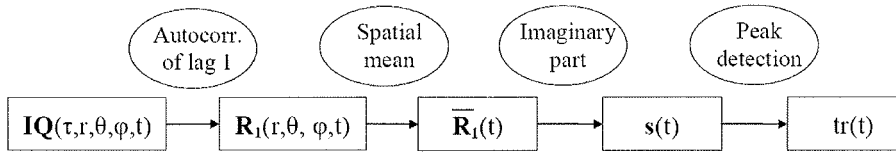

Figure D.1: Processing chain of the real-time TDOG gating technique.

Complex demodulated tissue Doppler data was recorded at in a 2D sector or a 3D pyramidal scan with scan depth equal to the tissue scan. Several scan geometries were tried, such as a 5° 2D scan, a 10° 2D scan, a $8° \times 8°$ 3D scan and more. The following processing was performed on the 3D IQ data, in real-time on the scanner (see figure D.1, too):

1. In each spatial position (r, θ, ϕ) of the Doppler scan, the auto correlation of lag 1 was calculated, yielding $R_1(r, \theta, \phi, t)$.

2. The mean value of the imaginary part of R_1 was calculated in each frame, yielding a complex valued function of time. The imaginary part s of this function is in the following termed the *tissue Doppler trace*:

$$s(t) = Im(\text{mean}_{r,\theta,\phi} R_1(r, \theta, \phi, t)) \tag{D.1}$$

   It was shown in Brekke et al.[1] that, for data captured from the fetal myocardium with apical insonation, $s(t)$ exhibited distinct local minima in each rapid relaxation of the myocardium.

3. Let $\bar{s}(t, T)$ be the sliding mean of $s(t)$ over the interval $[t-T, T]$, and $\sigma_s(t, T)$ be the standard deviation over the same interval. The gain-corrected tissue Doppler trace S_{AGC} defined by

$$S_{AGC}(t, T) = \frac{s(t) - \bar{s}(t, T)}{\sigma_s(t, T)} \tag{D.2}$$

   then had an amplitude that scaled with the noise level of s. The threshold signal $S_{thr}(t)$ was furthermore defined as a binary signal derived from $S_{AGC}(t, T)$:

$$S_{thr}(t) \begin{cases} 1 & \text{, when } S_{AGC}(t, T) > C_{\text{thr}} \\ 0 & \text{, otherwise} \end{cases} \tag{D.3}$$

4. A trigger event time T_n was detected each time the threshold $S_{thr}(T_n, T)$ changed from 0 to 1 (with the additional condition $T_n > T_{n-1} + 1/HR_{max}$, i.e. suppressing multiple peaks corresponding to too high heart rate).

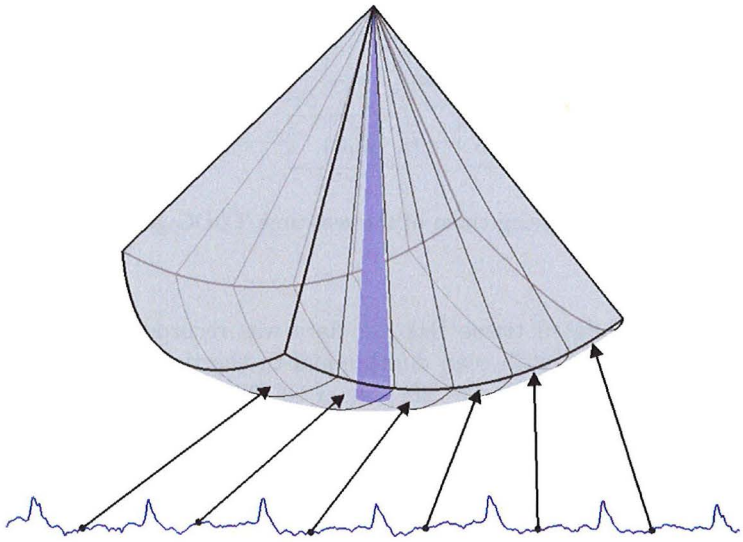

Figure D.2: In TDOG stitched scanning mode, the total scanning volume is divided into subvolumes which are scanned in successive cardiac cycles. The cycles are detected by the TDOG trigger signal, derived from tissue Doppler data simultaneously captured in the center part of the total scanning area (indicated by the blue cone).

The gain-corrected tissue Doppler trace and the detected trig times were sent as external traces to the scanner control SW and displayed in real-time as on the scanner display (being similar to an ECG signal with peaks corresponding to heart beats).

2.2 Real-time volume stitching

Real-time volume stitching is a method for gated acquisition of echocardiographic data with real-time volume rendering display [2]. With this technique, the data volume to be captured is divided into N separate subvolumes. One subvolume is scanned at the time, and QRS events detected from an ECG trace induce a change of active subvolume, see figure D.2. At screen refresh time during scanning, a full cardiac volume with $N-1$ seams between subvolumes is assembled and volume-rendered on the fly.

The same method was in this work applied to cardiac 3D images of the fe-

tal heart. The algorithm described in section 2.1 was implemented as a C++ program running concurrently with the scanner control software in an Vivid 7 scanner from GE Healthcare, and TDOG trigger events were passed to the acquisition setup SW of the scanner inducing the scanning location to be swapped to the next subvolume.

The scanner was configured to capture two data streams: 1) A volumetric gray-scale tissue scan with angle $30° \times 30°$, set up for gated scanning over six cardiac cycles (utilizing the technique presented in Brekke et al. [2]). A scan geometry with six subvolume scans spanning $30° \times 5°$ was applied, but both lower and higher numbers of subvolume could be configured. 2) A tissue Doppler data stream spanning a volume with angles $\theta_{max} \times \phi_{max}$. Different combination of azimuth angular span θ_{max} and elevational angular span ϕ_{max} were tried. The Doppler data stream was used for gating and was not changed from cycle to cycle.

The transducer operated in second harmonic mode for the capture of gray-scale data, with a transmit frequency of 2.0 MHz and a receive frequency of 4.1 MHz, and in fundamental mode with frequency 2 MHz for capture of tissue Doppler data. Two Doppler volumes were captured for each single tissue data set, thus doubling the temporal resolution of the TDOG signal compared to the 3D volume rate.

3 Results

3.1 Real-time TDOG signal

Figure D.3 shows captured TDOG signal and the derived TDOG trigger times under different circumstances. We readily see that the waveform of tissue Doppler trace s differed substantially between the settings. Row one and four showed a stable tissue Doppler trace with good trigger detection, while row one and three showed such a small difference in signal amplitude between main peaks and intermediate peaks that the real-time peak-detection algorithm missed some of the peaks.

The lowermost trace in figure D.3 shows the tissue Doppler trace derived from a 2D tissue Doppler scan with a scan angle of 45°, taken from an apical four-chamber cardiac view. In this case, the peak level was substantially higher compared to non-significant peaks and noise than in the 3D Doppler scan setup tested.

3.2 Real time volume stitching

The real-time stitching algorithm described in section 2.2 was applied to to data captured from fetal hearts of five fetuses with gestational age 20-24 weeks. Figure

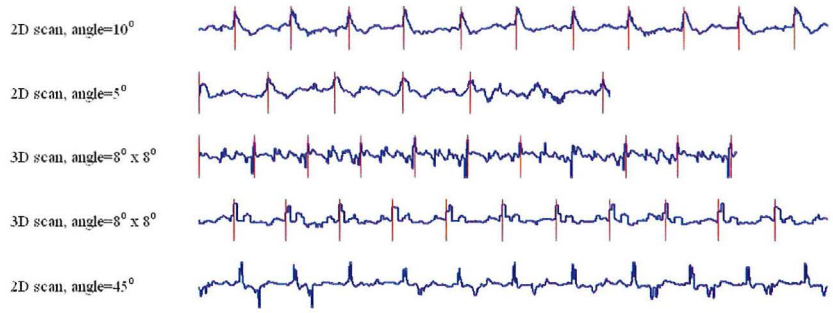

Figure D.3: TDOG signal with trigger times calculated in real-time from 3D tissue Doppler data from different fetuses. The first and fourth rows show tissue Doppler traces that were adequate for TDOG gating, while in number two and three, the TDOG algorithm failed to detect all the heart beats due to a too noisy trace. The fifth row shows the tissue Doppler trace from a wide angle 2D tissue Doppler scan from a apical four-chamber cardiac view.

Figure D.4: Three planar slices taken from a 3D cine-loop in a TDOG stitched 4D scan. The 3D volume was assembled from 6 cardiac cycles, and apical insonation was applied, yielding a reliable TDOG signal and well-aligned subvolumes. Left: four-chamber view, middle: ascending aorta, right: short axis view.

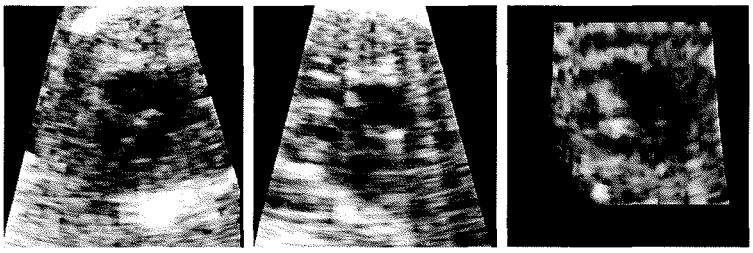

Figure D.5: Same setup as in figure D.4, but with an irregular TDOG signal due to weak motion in the image. This caused severe stitching artifacts.

D.4 shows an example of a cine-loop with successful stitching, while figure D.5 shows a cine-loop with evident stitching artefacts.

4 Discussion

4.1 Real-time detection of peaks in the TDOG signal

As illustrated in figure D.3, the regularity of the tissue Doppler trace depended on both the image contents and the scan setup of the Doppler scan. There were two reasons for failure of detecting heart beats with TDOG, both due to difficult position of the fetus: 1) inadequate acoustic access to the fetal heart in general and 2) low velocity component along the ultrasound beams due to unfavourable orientation of the fetal heart in the image.

In case 1), 2DE examination, too, would give poor results, thus this case was not a failure of the TDOG method itself.

Case 2) could be addressed in two ways. Firstly, one could aim at getting apical insonation angle and let the Doppler scan cover a wide area, thereby getting significant velocity components along the beams in the Doppler scan. This precaution was taken for the rows 1, 4 and 5 in figure D.3, all of which had satisfactory trigger stability. Secondly, one could use vector velocity estimators as a supplement to the pure Doppler estimators utilized in the experiment, thereby getting a velocity trace that better adapts to lateral motion (one could e.g. use a combined Doppler and speckle tracking estimator as proposed by Brekke et al. [3]).

4.2 Volume stitching in-vivo

Although adequate reconstruction were obtained for only two of five fetuses, the experiments show that the proposed method is a feasible way to increase frame

rate for fetal 3DE.

Fetus motion during data acquisition occurred frequently during all echo examinations. This caused two problems: 1) false peaks were present in the tissue Doppler trace and 2) stitching artifacts were visible in the assembled data. Artifacts is impossible to eliminate for any gated technique when the fetus is moving. However, artifacts constitute a smaller problem with volume-stitched reconstructions than with B-mode reconstruction, since the acquisition time of a full volume is much smaller (2 s vs. $\approx$10 s).

The resolution of the 3D data shown in figure D.4 appears poor compared to B-mode images recorded with dedicated transducers for fetal echo examinations. This is due to the low frequency and limited aperture of the applied transducer, being designed for cardiac imaging of adult persons. An ideal transducer for acquisition of high-frame rate 3D fetal cardiac images should have larger aperture and higher frequency and be able to do octave imaging with higher frequency (e.g., 5 MHz transmit- and 10 MHz receive frequency).

5 Conclusion

Real-time generation of a cardiac gating signal calculated from tissue Doppler data (the TDOG signal) has been implemented, and a trigger signal coherent with the cardiac phase was derived from data captured from fetal hearts *in-vivo*.

Real-time volume stitching triggered by the TDOG signal was successfully demonstrated and, for a stitched cine-loop acquired over six cardiac cycles, a volume rate of 67 frames/s was obtained.

References

1. S. Brekke, E. Tegnander, S. H. Eik-Nes, and H. G. Torp. Tissue Doppler gated (TDOG) dynamic 3D ultrasound imaging of the fetal heart. *Ultrasound Obstet Gynecol*, 24(5):192–198, May 2004.

2. S. Brekke, S. I. Rabben, A. Haugen, G. U. Haugen, E. N. Steen, and H. G. Torp. Real-time volume stitching in 4D echocardiography. In *IEEE UFFC Ultrasonic Symposium Proceedings*. IEEE UFFC, 2005.

3. S. Brekke, C. B. Ingul, S. A. Aase, and H. G. Torp. Increasing frame rate in ultrasound imaging by temporal morphing using tissue Doppler. *IEEE Trans Ultrason Ferroelectr Freq Control*, 53(5):936–946, May 2006.

4. J. Deng, C. F. Ruff, A. D. Linney, W. R. Lees, M. A. Hanson, and C. H. Rodeck. Simultaneous use of two ultrasound scanners for motion-gated three-dimensional fetal echocardiography. *Ultrasound Med Biol*, 26(6): 1021–1032, 2000.

5. G. R. DeVore. The prenatal diagnosis of congenital heart disease–a practical approach for the fetal sonographer. *J Clin Ultrasound*, 13(4):229–245, May 1985.

6. G. R. Devore, P. Falkensammer, M. S. Sklansky, and L. D. Platt. Spatio-temporal image correlation (STIC): new technology for evaluation of the fetal heart. *Ultrasound Obstet Gynecol*, 22(4):380–87, Oct 2003.

7. U. Herberg, H. Goldberg, and J. Breuer. Dynamic free-hand three-dimensional fetal echocardiography gated by cardiotocography. *Ultrasound Obstet Gynecol*, 22(5):493–502, November 2003.

8. M. S. Sklansky, T. R. Nelson, and D. H. Pretorius. Usefulness of gated three-dimensional fetal echocardiography to reconstsruct and display structures not visualized with two-dimensional imaging. *Am J Cardiol*, 80: 665–8, Sept 1997.

Dissertations at the Faculty of Medicine, NTNU

1977

1. Knut Joachim Berg: EFFECT OF ACETYLSALICYLIC ACID ON RENAL FUNCTION
2. Karl Erik Viken and Arne Ødegaard: STUDIES ON HUMAN MONOCYTES CULTURED *IN VITRO*

1978

3. Karel Bjørn Cyvin: CONGENITAL DISLOCATION OF THE HIP JOINT.
4. Alf O. Brubakk: METHODS FOR STUDYING FLOW DYNAMICS IN THE LEFT VENTRICLE AND THE AORTA IN MAN.

1979

5. Geirmund Unsgaard: CYTOSTATIC AND IMMUNOREGULATORY ABILITIES OF HUMAN BLOOD MONOCYTES CULTURED *IN VITRO*

1980

6. Størker Jørstad: URAEMIC TOXINS
7. Arne Olav Jenssen: SOME RHEOLOGICAL, CHEMICAL AND STRUCTURAL PROPERTIES OF MUCOID SPUTUM FROM PATIENTS WITH CHRONIC OBSTRUCTIVE BRONCHITIS

1981

8. Jens Hammerstrøm: CYTOSTATIC AND CYTOLYTIC ACTIVITY OF HUMAN MONOCYTES AND EFFUSION MACROPHAGES AGAINST TUMOR CELLS *IN VITRO*

1983

9. Tore Syversen: EFFECTS OF METHYLMERCURY ON RAT BRAIN PROTEIN.
10. Torbjørn Iversen: SQUAMOUS CELL CARCINOMA OF THE VULVA.

1984

11. Tor-Erik Widerøe: ASPECTS OF CONTINUOUS AMBULATORY PERITONEAL DIALYSIS.
12. Anton Hole: ALTERATIONS OF MONOCYTE AND LYMPHOCYTE FUNCTIONS IN REALTION TO SURGERY UNDER EPIDURAL OR GENERAL ANAESTHESIA.
13. Terje Terjesen: FRACTURE HEALING AN STRESS-PROTECTION AFTER METAL PLATE FIXATION AND EXTERNAL FIXATION.
14. Carsten Saunte: CLUSTER HEADACHE SYNDROME.
15. Inggard Lereim: TRAFFIC ACCIDENTS AND THEIR CONSEQUENCES.
16. Bjørn Magne Eggen: STUDIES IN CYTOTOXICITY IN HUMAN ADHERENT MONONUCLEAR BLOOD CELLS.
17. Trond Haug: FACTORS REGULATING BEHAVIORAL EFFECTS OG DRUGS.

1985

18. Sven Erik Gisvold: RESUSCITATION AFTER COMPLETE GLOBAL BRAIN ISCHEMIA.
19. Terje Espevik: THE CYTOSKELETON OF HUMAN MONOCYTES.
20. Lars Bevanger: STUDIES OF THE Ibc (c) PROTEIN ANTIGENS OF GROUP B STREPTOCOCCI.
21. Ole-Jan Iversen: RETROVIRUS-LIKE PARTICLES IN THE PATHOGENESIS OF PSORIASIS.
22. Lasse Eriksen: EVALUATION AND TREATMENT OF ALCOHOL DEPENDENT BEHAVIOUR.
23. Per I. Lundmo: ANDROGEN METABOLISM IN THE PROSTATE.

1986

24. Dagfinn Berntzen: ANALYSIS AND MANAGEMENT OF EXPERIMENTAL AND CLINICAL PAIN.
25. Odd Arnold Kildahl-Andersen: PRODUCTION AND CHARACTERIZATION OF MONOCYTE-DERIVED CYTOTOXIN AND ITS ROLE IN MONOCYTE-MEDIATED CYTOTOXICITY.
26. Ola Dale: VOLATILE ANAESTHETICS.

1987

27. Per Martin Kleveland: STUDIES ON GASTRIN.
28. Audun N. Øksendal: THE CALCIUM PARADOX AND THE HEART.
29. Vilhjalmur R. Finsen: HIP FRACTURES

1988

30. Rigmor Austgulen: TUMOR NECROSIS FACTOR: A MONOCYTE-DERIVED REGULATOR OF CELLULAR GROWTH.
31. Tom-Harald Edna: HEAD INJURIES ADMITTED TO HOSPITAL.
32. Joseph D. Borsi: NEW ASPECTS OF THE CLINICAL PHARMACOKINETICS OF METHOTREXATE.
33. Olav F. M. Sellevold: GLUCOCORTICOIDS IN MYOCARDIAL PROTECTION.

34. Terje Skjærpe: NONINVASIVE QUANTITATION OF GLOBAL PARAMETERS ON LEFT VENTRICULAR FUNCTION: THE SYSTOLIC PULMONARY ARTERY PRESSURE AND CARDIAC OUTPUT.
35. Eyvind Rødahl: STUDIES OF IMMUNE COMPLEXES AND RETROVIRUS-LIKE ANTIGENS IN PATIENTS WITH ANKYLOSING SPONDYLITIS.
36. Ketil Thorstensen: STUDIES ON THE MECHANISMS OF CELLULAR UPTAKE OF IRON FROM TRANSFERRIN.
37. Anna Midelfart: STUDIES OF THE MECHANISMS OF ION AND FLUID TRANSPORT IN THE BOVINE CORNEA.
38. Eirik Helseth: GROWTH AND PLASMINOGEN ACTIVATOR ACTIVITY OF HUMAN GLIOMAS AND BRAIN METASTASES - WITH SPECIAL REFERENCE TO TRANSFORMING GROWTH FACTOR BETA AND THE EPIDERMAL GROWTH FACTOR RECEPTOR.
39. Petter C. Borchgrevink: MAGNESIUM AND THE ISCHEMIC HEART.
40. Kjell-Arne Rein: THE EFFECT OF EXTRACORPOREAL CIRCULATION ON SUBCUTANEOUS TRANSCAPILLARY FLUID BALANCE.
41. Arne Kristian Sandvik: RAT GASTRIC HISTAMINE.
42. Carl Bredo Dahl: ANIMAL MODELS IN PSYCHIATRY.

1989

43. Torbjørn A. Fredriksen: CERVICOGENIC HEADACHE.
44. Rolf A. Walstad: CEFTAZIDIME.
45. Rolf Salvesen: THE PUPIL IN CLUSTER HEADACHE.
46. Nils Petter Jørgensen: DRUG EXPOSURE IN EARLY PREGNANCY.
47. Johan C. Ræder: PREMEDICATION AND GENERAL ANAESTHESIA IN OUTPATIENT GYNECOLOGICAL SURGERY.
48. M. R. Shalaby: IMMUNOREGULATORY PROPERTIES OF TNF-α AND THE RELATED CYTOKINES.
49. Anders Waage: THE COMPLEX PATTERN OF CYTOKINES IN SEPTIC SHOCK.
50. Bjarne Christian Eriksen: ELECTROSTIMULATION OF THE PELVIC FLOOR IN FEMALE URINARY INCONTINENCE.
51. Tore B. Halvorsen: PROGNOSTIC FACTORS IN COLORECTAL CANCER.

1990

52. Asbjørn Nordby: CELLULAR TOXICITY OF ROENTGEN CONTRAST MEDIA.
53. Kåre E. Tvedt: X-RAY MICROANALYSIS OF BIOLOGICAL MATERIAL.
54. Tore C. Stiles: COGNITIVE VULNERABILITY FACTORS IN THE DEVELOPMENT AND MAINTENANCE OF DEPRESSION.
55. Eva Hofsli: TUMOR NECROSIS FACTOR AND MULTIDRUG RESISTANCE.
56. Helge S. Haarstad: TROPHIC EFFECTS OF CHOLECYSTOKININ AND SECRETIN ON THE RAT PANCREAS.
57. Lars Engebretsen: TREATMENT OF ACUTE ANTERIOR CRUCIATE LIGAMENT INJURIES.
58. Tarjei Rygnestad: DELIBERATE SELF-POISONING IN TRONDHEIM.
59. Arne Z. Henriksen: STUDIES ON CONSERVED ANTIGENIC DOMAINS ON MAJOR OUTER MEMBRANE PROTEINS FROM ENTEROBACTERIA.
60. Steinar Westin: UNEMPLOYMENT AND HEALTH: Medical and social consequences of a factory closure in a ten-year controlled follow-up study.
61. Ylva Sahlin: INJURY REGISTRATION, a tool for accident preventive work.
62. Helge Bjørnstad Pettersen: BIOSYNTHESIS OF COMPLEMENT BY HUMAN ALVEOLAR MACROPHAGES WITH SPECIAL REFERENCE TO SARCOIDOSIS.
63. Berit Schei: TRAPPED IN PAINFUL LOVE.
64. Lars J. Vatten: PROSPECTIVE STUDIES OF THE RISK OF BREAST CANCER IN A COHORT OF NORWEGIAN WOMAN.

1991

65. Kåre Bergh: APPLICATIONS OF ANTI-C5a SPECIFIC MONOCLONAL ANTIBODIES FOR THE ASSESSMENT OF COMPLEMENT ACTIVATION.
66. Svein Svenningsen: THE CLINICAL SIGNIFICANCE OF INCREASED FEMORAL ANTEVERSION.
67. Olbjørn Klepp: NONSEMINOMATOUS GERM CELL TESTIS CANCER: THERAPEUTIC OUTCOME AND PROGNOSTIC FACTORS.
68. Trond Sand: THE EFFECTS OF CLICK POLARITY ON BRAINSTEM AUDITORY EVOKED POTENTIALS AMPLITUDE, DISPERSION, AND LATENCY VARIABLES.

69. Kjetil B. Åsbakk: STUDIES OF A PROTEIN FROM PSORIATIC SCALE, PSO P27, WITH RESPECT TO ITS POTENTIAL ROLE IN IMMUNE REACTIONS IN PSORIASIS.
70. Arnulf Hestnes: STUDIES ON DOWN'S SYNDROME.
71. Randi Nygaard: LONG-TERM SURVIVAL IN CHILDHOOD LEUKEMIA.
72. Bjørn Hagen: THIO-TEPA.
73. Svein Anda: EVALUATION OF THE HIP JOINT BY COMPUTED TOMOGRAMPHY AND ULTRASONOGRAPHY.

1992

74. Martin Svartberg: AN INVESTIGATION OF PROCESS AND OUTCOME OF SHORT-TERM PSYCHODYNAMIC PSYCHOTHERAPY.
75. Stig Arild Slørdahl: AORTIC REGURGITATION.
76. Harold C Sexton: STUDIES RELATING TO THE TREATMENT OF SYMPTOMATIC NON-PSYCHOTIC PATIENTS.
77. Maurice B. Vincent: VASOACTIVE PEPTIDES IN THE OCULAR/FOREHEAD AREA.
78. Terje Johannessen: CONTROLLED TRIALS IN SINGLE SUBJECTS.
79. Turid Nilsen: PYROPHOSPHATE IN HEPATOCYTE IRON METABOLISM.
80. Olav Haraldseth: NMR SPECTROSCOPY OF CEREBRAL ISCHEMIA AND REPERFUSION IN RAT.
81. Eiliv Brenna: REGULATION OF FUNCTION AND GROWTH OF THE OXYNTIC MUCOSA.

1993

82. Gunnar Bovim: CERVICOGENIC HEADACHE.
83. Jarl Arne Kahn: ASSISTED PROCREATION.
84. Bjørn Naume: IMMUNOREGULATORY EFFECTS OF CYTOKINES ON NK CELLS.
85. Rune Wiseth: AORTIC VALVE REPLACEMENT.
86. Jie Ming Shen: BLOOD FLOW VELOCITY AND RESPIRATORY STUDIES.
87. Piotr Kruszewski: SUNCT SYNDROME WITH SPECIAL REFERENCE TO THE AUTONOMIC NERVOUS SYSTEM.
88. Mette Haase Moen: ENDOMETRIOSIS.
89. Anne Vik: VASCULAR GAS EMBOLISM DURING AIR INFUSION AND AFTER DECOMPRESSION IN PIGS.
90. Lars Jacob Stovner: THE CHIARI TYPE I MALFORMATION.
91. Kjell Å. Salvesen: ROUTINE ULTRASONOGRAPHY IN UTERO AND DEVELOPMENT IN CHILDHOOD.

1994

92. Nina-Beate Liabakk: DEVELOPMENT OF IMMUNOASSAYS FOR TNF AND ITS SOLUBLE RECEPTORS.
93. Sverre Helge Torp: *erb*B ONCOGENES IN HUMAN GLIOMAS AND MENINGIOMAS.
94. Olav M. Linaker: MENTAL RETARDATION AND PSYCHIATRY. Past and present.
95. Per Oscar Feet: INCREASED ANTIDEPRESSANT AND ANTIPANIC EFFECT IN COMBINED TREATMENT WITH DIXYRAZINE AND TRICYCLIC ANTIDEPRESSANTS.
96. Stein Olav Samstad: CROSS SECTIONAL FLOW VELOCITY PROFILES FROM TWO-DIMENSIONAL DOPPLER ULTRASOUND: Studies on early mitral blood flow.
97. Bjørn Backe: STUDIES IN ANTENATAL CARE.
98. Gerd Inger Ringdal: QUALITY OF LIFE IN CANCER PATIENTS.
99. Torvid Kiserud: THE DUCTUS VENOSUS IN THE HUMAN FETUS.
100. Hans E. Fjøsne: HORMONAL REGULATION OF PROSTATIC METABOLISM.
101. Eylert Brodtkorb: CLINICAL ASPECTS OF EPILEPSY IN THE MENTALLY RETARDED.
102. Roar Juul: PEPTIDERGIC MECHANISMS IN HUMAN SUBARACHNOID HEMORRHAGE.
103. Unni Syversen: CHROMOGRANIN A. Phsysiological and Clinical Role.

1995

104. Odd Gunnar Brakstad: THERMOSTABLE NUCLEASE AND THE *nuc* GENE IN THE DIAGNOSIS OF *Staphylococcus aureus* INFECTIONS.
105. Terje Engan: NUCLEAR MAGNETIC RESONANCE (NMR) SPECTROSCOPY OF PLASMA IN MALIGNANT DISEASE.
106. Kirsten Rasmussen: VIOLENCE IN THE MENTALLY DISORDERED.
107. Finn Egil Skjeldestad: INDUCED ABORTION: Timetrends and Determinants.
108. Roar Stenseth: THORACIC EPIDURAL ANALGESIA IN AORTOCORONARY BYPASS SURGERY.
109. Arild Faxvaag: STUDIES OF IMMUNE CELL FUNCTION *in mice infected with* MURINE RETROVIRUS.

1996

110. Svend Aakhus: NONINVASIVE COMPUTERIZED ASSESSMENT OF LEFT VENTRICULAR FUNCTION AND SYSTEMIC ARTERIAL PROPERTIES. Methodology and some clinical applications.
111. Klaus-Dieter Bolz: INTRAVASCULAR ULTRASONOGRAPHY.
112. Petter Aadahl: CARDIOVASCULAR EFFECTS OF THORACIC AORTIC CROSS-CLAMPING.
113. Sigurd Steinshamn: CYTOKINE MEDIATORS DURING GRANULOCYTOPENIC INFECTIONS.
114. Hans Stifoss-Hanssen: SEEKING MEANING OR HAPPINESS?
115. Anne Kvikstad: LIFE CHANGE EVENTS AND MARITAL STATUS IN RELATION TO RISK AND PROGNOSIS OF CANSER.
116. Torbjørn Grøntvedt: TREATMENT OF ACUTE AND CHRONIC ANTERIOR CRUCIATE LIGAMENT INJURIES. A clinical and biomechanical study.
117. Sigrid Hørven Wigers: CLINICAL STUDIES OF FIBROMYALGIA WITH FOCUS ON ETIOLOGY, TREATMENT AND OUTCOME.
118. Jan Schjøtt: MYOCARDIAL PROTECTION: Functional and Metabolic Characteristics of Two Endogenous Protective Principles.
119. Marit Martinussen: STUDIES OF INTESTINAL BLOOD FLOW AND ITS RELATION TO TRANSITIONAL CIRCULATORY ADAPATION IN NEWBORN INFANTS.
120. Tomm B. Müller: MAGNETIC RESONANCE IMAGING IN FOCAL CEREBRAL ISCHEMIA.
121. Rune Haaverstad: OEDEMA FORMATION OF THE LOWER EXTREMITIES.
122. Magne Børset: THE ROLE OF CYTOKINES IN MULTIPLE MYELOMA, WITH SPECIAL REFERENCE TO HEPATOCYTE GROWTH FACTOR.
123. Geir Smedslund: A THEORETICAL AND EMPIRICAL INVESTIGATION OF SMOKING, STRESS AND DISEASE: RESULTS FROM A POPULATION SURVEY.

1997

124. Torstein Vik: GROWTH, MORBIDITY, AND PSYCHOMOTOR DEVELOPMENT IN INFANTS WHO WERE GROWTH RETARDED *IN UTERO*.
125. Siri Forsmo: ASPECTS AND CONSEQUENCES OF OPPORTUNISTIC SCREENING FOR CERVICAL CANCER. Results based on data from three Norwegian counties.
126. Jon S. Skranes: CEREBRAL MRI AND NEURODEVELOPMENTAL OUTCOME IN VERY LOW BIRTH WEIGHT (VLBW) CHILDREN. A follow-up study of a geographically based year cohort of VLBW children at ages one and six years.
127. Knut Bjørnstad: COMPUTERIZED ECHOCARDIOGRAPHY FOR EVALUTION OF CORONARY ARTERY DISEASE.
128. Grethe Elisabeth Borchgrevink: DIAGNOSIS AND TREATMENT OF WHIPLASH/NECK SPRAIN INJURIES CAUSED BY CAR ACCIDENTS.
129. Tor Elsås: NEUROPEPTIDES AND NITRIC OXIDE SYNTHASE IN OCULAR AUTONOMIC AND SENSORY NERVES.
130. Rolf W. Gråwe: EPIDEMIOLOGICAL AND NEUROPSYCHOLOGICAL PERSPECTIVES ON SCHIZOPHRENIA.
131. Tonje Strømholm: CEREBRAL HAEMODYNAMICS DURING THORACIC AORTIC CROSSCLAMPING. An experimental study in pigs.

1998

132. Martinus Bråten: STUDIES ON SOME PROBLEMS REALTED TO INTRAMEDULLARY NAILING OF FEMORAL FRACTURES.
133. Ståle Nordgård: PROLIFERATIVE ACTIVITY AND DNA CONTENT AS PROGNOSTIC INDICATORS IN ADENOID CYSTIC CARCINOMA OF THE HEAD AND NECK.
134. Egil Lien: SOLUBLE RECEPTORS FOR **TNF** AND **LPS**: RELEASE PATTERN AND POSSIBLE SIGNIFICANCE IN DISEASE.
135. Marit Bjørgaas: HYPOGLYCAEMIA IN CHILDREN WITH DIABETES MELLITUS
136. Frank Skorpen: GENETIC AND FUNCTIONAL ANALYSES OF DNA REPAIR IN HUMAN CELLS.
137. Juan A. Pareja: SUNCT SYNDROME. ON THE CLINICAL PICTURE. ITS DISTINCTION FROM OTHER, SIMILAR HEADACHES.
138. Anders Angelsen: NEUROENDOCRINE CELLS IN HUMAN PROSTATIC CARCINOMAS AND THE PROSTATIC COMPLEX OF RAT, GUINEA PIG, CAT AND DOG.
139. Fabio Antonaci: CHRONIC PAROXYSMAL HEMICRANIA AND HEMICRANIA CONTINUA: TWO DIFFERENT ENTITIES?

140. Sven M. Carlsen: ENDOCRINE AND METABOLIC EFFECTS OF METFORMIN WITH SPECIAL EMPHASIS ON CARDIOVASCULAR RISK FACTORES.

1999

141. Terje A. Murberg: DEPRESSIVE SYMPTOMS AND COPING AMONG PATIENTS WITH CONGESTIVE HEART FAILURE.
142. Harm-Gerd Karl Blaas: THE EMBRYONIC EXAMINATION. Ultrasound studies on the development of the human embryo.
143. Noèmi Becser Andersen:THE CEPHALIC SENSORY NERVES IN UNILATERAL HEADACHES. Anatomical background and neurophysiological evaluation.
144. Eli-Janne Fiskerstrand: LASER TREATMENT OF PORT WINE STAINS. A study of the efficacy and limitations of the pulsed dye laser. Clinical and morfological analyses aimed at improving the therapeutic outcome.
145. Bård Kulseng: A STUDY OF ALGINATE CAPSULE PROPERTIES AND CYTOKINES IN RELATION TO INSULIN DEPENDENT DIABETES MELLITUS.
146. Terje Haug: STRUCTURE AND REGULATION OF THE HUMAN UNG GENE ENCODING URACIL-DNA GLYCOSYLASE.
147. Heidi Brurok: MANGANESE AND THE HEART. A Magic Metal with Diagnostic and Therapeutic Possibilites.
148. Agnes Kathrine Lie: DIAGNOSIS AND PREVALENCE OF HUMAN PAPILLOMAVIRUS INFECTION IN CERVICAL INTRAEPITELIAL NEOPLASIA. Relationship to Cell Cycle Regulatory Proteins and HLA DQB1 Genes.
149. Ronald Mårvik: PHARMACOLOGICAL, PHYSIOLOGICAL AND PATHOPHYSIOLOGICAL STUDIES ON ISOLATED STOMACS.
150. Ketil Jarl Holen: THE ROLE OF ULTRASONOGRAPHY IN THE DIAGNOSIS AND TREATMENT OF HIP DYSPLASIA IN NEWBORNS.
151. Irene Hetlevik: THE ROLE OF CLINICAL GUIDELINES IN CARDIOVASCULAR RISK INTERVENTION IN GENERAL PRACTICE.
152. Katarina Tunòn: ULTRASOUND AND PREDICTION OF GESTATIONAL AGE.
153. Johannes Soma: INTERACTION BETWEEN THE LEFT VENTRICLE AND THE SYSTEMIC ARTERIES.
154. Arild Aamodt: DEVELOPMENT AND PRE-CLINICAL EVALUATION OF A CUSTOM-MADE FEMORAL STEM.
155. Agnar Tegnander: DIAGNOSIS AND FOLLOW-UP OF CHILDREN WITH SUSPECTED OR KNOWN HIP DYSPLASIA.
156. Bent Indredavik: STROKE UNIT TREATMENT: SHORT AND LONG-TERM EFFECTS
157. Jolanta Vanagaite Vingen: PHOTOPHOBIA AND PHONOPHOBIA IN PRIMARY HEADACHES

2000

158. Ola Dalsegg Sæther: PATHOPHYSIOLOGY DURING PROXIMAL AORTIC CROSS-CLAMPING CLINICAL AND EXPERIMENTAL STUDIES
159. xxxxxxxxx (blind number)
160. Christina Vogt Isaksen: PRENATAL ULTRASOUND AND POSTMORTEM FINDINGS – A TEN YEAR CORRELATIVE STUDY OF FETUSES AND INFANTS WITH DEVELOPMENTAL ANOMALIES.
161. Holger Seidel: HIGH-DOSE METHOTREXATE THERAPY IN CHILDREN WITH ACUTE LYMPHOCYTIC LEUKEMIA: DOSE, CONCENTRATION, AND EFFECT CONSIDERATIONS.
162. Stein Hallan: IMPLEMENTATION OF MODERN MEDICAL DECISION ANALYSIS INTO CLINICAL DIAGNOSIS AND TREATMENT.
163. Malcolm Sue-Chu: INVASIVE AND NON-INVASIVE STUDIES IN CROSS-COUNTRY SKIERS WITH ASTHMA-LIKE SYMPTOMS.
164. Ole-Lars Brekke: EFFECTS OF ANTIOXIDANTS AND FATTY ACIDS ON TUMOR NECROSIS FACTOR-INDUCED CYTOTOXICITY.
165. Jan Lundbom: AORTOCORONARY BYPASS SURGERY: CLINICAL ASPECTS, COST CONSIDERATIONS AND WORKING ABILITY.
166. John-Anker Zwart: LUMBAR NERVE ROOT COMPRESSION, BIOCHEMICAL AND NEUROPHYSIOLOGICAL ASPECTS.
167. Geir Falck: HYPEROSMOLALITY AND THE HEART.
168. Eirik Skogvoll: CARDIAC ARREST Incidence, Intervention and Outcome.
169. Dalius Bansevicius: SHOULDER-NECK REGION IN CERTAIN HEADACHES AND CHRONIC PAIN SYNDROMES.

170. Bettina Kinge: REFRACTIVE ERRORS AND BIOMETRIC CHANGES AMONG UNIVERSITY STUDENTS IN NORWAY.
171. Gunnar Qvigstad: CONSEQUENCES OF HYPERGASTRINEMIA IN MAN
172. Hanne Ellekjær: EPIDEMIOLOGICAL STUDIES OF STROKE IN A NORWEGIAN POPULATION. INCIDENCE, RISK FACTORS AND PROGNOSIS
173. Hilde Grimstad: VIOLENCE AGAINST WOMEN AND PREGNANCY OUTCOME.
174. Astrid Hjelde: SURFACE TENSION AND COMPLEMENT ACTIVATION: Factors influencing bubble formation and bubble effects after decompression.
175. Kjell A. Kvistad: MR IN BREAST CANCER – A CLINICAL STUDY.
176. Ivar Rossvoll: ELECTIVE ORTHOPAEDIC SURGERY IN A DEFINED POPULATION. Studies on demand, waiting time for treatment and incapacity for work.
177. Carina Seidel: PROGNOSTIC VALUE AND BIOLOGICAL EFFECTS OF HEPATOCYTE GROWTH FACTOR AND SYNDECAN-1 IN MULTIPLE MYELOMA.

2001

178. Alexander Wahba: THE INFLUENCE OF CARDIOPULMONARY BYPASS ON PLATELET FUNCTION AND BLOOD COAGULATION – DETERMINANTS AND CLINICAL CONSEQUENSES
179. Marcus Schmitt-Egenolf: THE RELEVANCE OF THE MAJOR hISTOCOMPATIBILITY COMPLEX FOR THE GENETICS OF PSORIASIS
180. Odrun Arna Gederaas: BIOLOGICAL MECHANISMS INVOLVED IN 5-AMINOLEVULINIC ACID BASED PHOTODYNAMIC THERAPY
181. Pål Richard Romundstad: CANCER INCIDENCE AMONG NORWEGIAN ALUMINIUM WORKERS
182. Henrik Hjorth-Hansen: NOVEL CYTOKINES IN GROWTH CONTROL AND BONE DISEASE OF MULTIPLE MYELOMA
183. Gunnar Morken: SEASONAL VARIATION OF HUMAN MOOD AND BEHAVIOUR
184. Bjørn Olav Haugen: MEASUREMENT OF CARDIAC OUTPUT AND STUDIES OF VELOCITY PROFILES IN AORTIC AND MITRAL FLOW USING TWO- AND THREE-DIMENSIONAL COLOUR FLOW IMAGING
185. Geir Bråthen: THE CLASSIFICATION AND CLINICAL DIAGNOSIS OF ALCOHOL-RELATED SEIZURES
186. Knut Ivar Aasarød: RENAL INVOLVEMENT IN INFLAMMATORY RHEUMATIC DISEASE. A Study of Renal Disease in Wegener's Granulomatosis and in Primary Sjögren's Syndrome
187. Trude Helen Flo: RESEPTORS INVOLVED IN CELL ACTIVATION BY DEFINED URONIC ACID POLYMERS AND BACTERIAL COMPONENTS
188. Bodil Kavli: HUMAN URACIL-DNA GLYCOSYLASES FROM THE UNG GENE: STRUCTRUAL BASIS FOR SUBSTRATE SPECIFICITY AND REPAIR
189. Liv Thommesen: MOLECULAR MECHANISMS INVOLVED IN TNF- AND GASTRIN-MEDIATED GENE REGULATION
190. Turid Lingaas Holmen: SMOKING AND HEALTH IN ADOLESCENCE; THE NORD-TRØNDELAG HEALTH STUDY, 1995-97
191. Øyvind Hjertner: MULTIPLE MYELOMA: INTERACTIONS BETWEEN MALIGNANT PLASMA CELLS AND THE BONE MICROENVIRONMENT
192. Asbjørn Støylen: STRAIN RATE IMAGING OF THE LEFT VENTRICLE BY ULTRASOUND. FEASIBILITY, CLINICAL VALIDATION AND PHYSIOLOGICAL ASPECTS
193. Kristian Midthjell: DIABETES IN ADULTS IN NORD-TRØNDELAG. PUBLIC HEALTH ASPECTS OF DIABETES MELLITUS IN A LARGE, NON-SELECTED NORWEGIAN POPULATION.
194. Guanglin Cui: FUNCTIONAL ASPECTS OF THE ECL CELL IN RODENTS
195. Ulrik Wisløff: CARDIAC EFFECTS OF AEROBIC ENDURANCE TRAINING: HYPERTROPHY, CONTRACTILITY AND CALCUIM HANDLING IN NORMAL AND FAILING HEART
196. Øyvind Halaas: MECHANISMS OF IMMUNOMODULATION AND CELL-MEDIATED CYTOTOXICITY INDUCED BY BACTERIAL PRODUCTS
197. Tore Amundsen: PERFUSION MR IMAGING IN THE DIAGNOSIS OF PULMONARY EMBOLISM
198. Nanna Kurtze: THE SIGNIFICANCE OF ANXIETY AND DEPRESSION IN FATIQUE AND PATTERNS OF PAIN AMONG INDIVIDUALS DIAGNOSED WITH FIBROMYALGIA: RELATIONS WITH QUALITY OF LIFE, FUNCTIONAL DISABILITY, LIFESTYLE, EMPLOYMENT STATUS, CO-MORBIDITY AND GENDER

199. Tom Ivar Lund Nilsen: PROSPECTIVE STUDIES OF CANCER RISK IN NORD-TRØNDELAG: THE HUNT STUDY. Associations with anthropometric, socioeconomic, and lifestyle risk factors
200. Asta Kristine Håberg: A NEW APPROACH TO THE STUDY OF MIDDLE CEREBRAL ARTERY OCCLUSION IN THE RAT USING MAGNETIC RESONANCE TECHNIQUES

2002

201. Knut Jørgen Arntzen: PREGNANCY AND CYTOKINES
202. Henrik Døllner: INFLAMMATORY MEDIATORS IN PERINATAL INFECTIONS
203. Asta Bye: LOW FAT, LOW LACTOSE DIET USED AS PROPHYLACTIC TREATMENT OF ACUTE INTESTINAL REACTIONS DURING PELVIC RADIOTHERAPY. A PROSPECTIVE RANDOMISED STUDY.
204. Sylvester Moyo: STUDIES ON STREPTOCOCCUS AGALACTIAE (GROUP B STREPTOCOCCUS) SURFACE-ANCHORED MARKERS WITH EMPHASIS ON STRAINS AND HUMAN SERA FROM ZIMBABWE.
205. Knut Hagen: HEAD-HUNT: THE EPIDEMIOLOGY OF HEADACHE IN NORD-TRØNDELAG
206. Li Lixin: ON THE REGULATION AND ROLE OF UNCOUPLING PROTEIN-2 IN INSULIN PRODUCING ß-CELLS
207. Anne Hildur Henriksen: SYMPTOMS OF ALLERGY AND ASTHMA VERSUS MARKERS OF LOWER AIRWAY INFLAMMATION AMONG ADOLESCENTS
208. Egil Andreas Fors: NON-MALIGNANT PAIN IN RELATION TO PSYCHOLOGICAL AND ENVIRONTENTAL FACTORS. EXPERIENTAL AND CLINICAL STUDES OF PAIN WITH FOCUS ON FIBROMYALGIA
209. Pål Klepstad: MORPHINE FOR CANCER PAIN
210. Ingunn Bakke: MECHANISMS AND CONSEQUENCES OF PEROXISOME PROLIFERATOR-INDUCED HYPERFUNCTION OF THE RAT GASTRIN PRODUCING CELL
211. Ingrid Susann Gribbestad: MAGNETIC RESONANCE IMAGING AND SPECTROSCOPY OF BREAST CANCER
212. Rønnaug Astri Ødegård: PREECLAMPSIA – MATERNAL RISK FACTORS AND FETAL GROWTH
213. Johan Haux: STUDIES ON CYTOTOXICITY INDUCED BY HUMAN NATURAL KILLER CELLS AND DIGITOXIN
214. Turid Suzanne Berg-Nielsen: PARENTING PRACTICES AND MENTALLY DISORDERED ADOLESCENTS
215. Astrid Rydning: BLOOD FLOW AS A PROTECTIVE FACTOR FOR THE STOMACH MUCOSA. AN EXPERIMENTAL STUDY ON THE ROLE OF MAST CELLS AND SENSORY AFFERENT NEURONS

2003

216. Jan Pål Loennechen: HEART FAILURE AFTER MYOCARDIAL INFARCTION. Regional Differences, Myocyte Function, Gene Expression, and Response to Cariporide, Losartan, and Exercise Training.
217. Elisabeth Qvigstad: EFFECTS OF FATTY ACIDS AND OVER-STIMULATION ON INSULIN SECRETION IN MAN
218. Arne Åsberg: EPIDEMIOLOGICAL STUDIES IN HEREDITARY HEMOCHROMATOSIS: PREVALENCE, MORBIDITY AND BENEFIT OF SCREENING.
219. Johan Fredrik Skomsvoll: REPRODUCTIVE OUTCOME IN WOMEN WITH RHEUMATIC DISEASE. A population registry based study of the effects of inflammatory rheumatic disease and connective tissue disease on reproductive outcome in Norwegian women in 1967-1995.
220. Siv Mørkved: URINARY INCONTINENCE DURING PREGNANCY AND AFTER DELIVERY: EFFECT OF PELVIC FLOOR MUSCLE TRAINING IN PREVENTION AND TREATMENT
221. Marit S. Jordhøy: THE IMPACT OF COMPREHENSIVE PALLIATIVE CARE
222. Tom Christian Martinsen: HYPERGASTRINEMIA AND HYPOACIDITY IN RODENTS – CAUSES AND CONSEQUENCES
223. Solveig Tingulstad: CENTRALIZATION OF PRIMARY SURGERY FOR OVARAIN CANCER. FEASIBILITY AND IMPACT ON SURVIVAL
224. Haytham Eloqayli: METABOLIC CHANGES IN THE BRAIN CAUSED BY EPILEPTIC SEIZURES
225. Torunn Bruland: STUDIES OF EARLY RETROVIRUS-HOST INTERACTIONS – VIRAL DETERMINANTS FOR PATHOGENESIS AND THE INFLUENCE OF SEX ON THE SUSCEPTIBILITY TO FRIEND MURINE LEUKAEMIA VIRUS INFECTION

226. Torstein Hole: DOPPLER ECHOCARDIOGRAPHIC EVALUATION OF LEFT VENTRICULAR FUNCTION IN PATIENTS WITH ACUTE MYOCARDIAL INFARCTION
227. Vibeke Nossum: THE EFFECT OF VASCULAR BUBBLES ON ENDOTHELIAL FUNCTION
228. Sigurd Fasting: ROUTINE BASED RECORDING OF ADVERSE EVENTS DURING ANAESTHESIA – APPLICATION IN QUALITY IMPROVEMENT AND SAFETY
229. Solfrid Romundstad: EPIDEMIOLOGICAL STUDIES OF MICROALBUMINURIA. THE NORD-TRØNDELAG HEALTH STUDY 1995-97 (HUNT 2)
230. Geir Torheim: PROCESSING OF DYNAMIC DATA SETS IN MAGNETIC RESONANCE IMAGING
231. Catrine Ahlén: SKIN INFECTIONS IN OCCUPATIONAL SATURATION DIVERS IN THE NORTH SEA AND THE IMPACT OF THE ENVIRONMENT
232. Arnulf Langhammer: RESPIRATORY SYMPTOMS, LUNG FUNCTION AND BONE MINERAL DENSITY IN A COMPREHENSIVE POPULATION SURVEY. THE NORD-TRØNDELAG HEALTH STUDY 1995-97. THE BRONCHIAL OBSTRUCTION IN NORD-TRØNDELAG STUDY
233. Einar Kjelsås: EATING DISORDERS AND PHYSICAL ACTIVITY IN NON-CLINICAL SAMPLES
234. Arne Wibe: RECTAL CANCER TREATMENT IN NORWAY – STANDARDISATION OF SURGERY AND QUALITY ASSURANCE

2004

235. Eivind Witsø: BONE GRAFT AS AN ANTIBIOTIC CARRIER
236. Anne Mari Sund: DEVELOPMENT OF DEPRESSIVE SYMPTOMS IN EARLY ADOLESCENCE
237. Hallvard Lærum: EVALUATION OF ELECTRONIC MEDICAL RECORDS – A CLINICAL TASK PERSPECTIVE
238. Gustav Mikkelsen: ACCESSIBILITY OF INFORMATION IN ELECTRONIC PATIENT RECORDS; AN EVALUATION OF THE ROLE OF DATA QUALITY
239. Steinar Krokstad: SOCIOECONOMIC INEQUALITIES IN HEALTH AND DISABILITY. SOCIAL EPIDEMIOLOGY IN THE NORD-TRØNDELAG HEALTH STUDY (HUNT), NORWAY
240. Arne Kristian Myhre: NORMAL VARIATION IN ANOGENITAL ANATOMY AND MICROBIOLOGY IN NON-ABUSED PRESCHOOL CHILDREN
241. Ingunn Dybedal: NEGATIVE REGULATORS OF HEMATOPOIETEC STEM AND PROGENITOR CELLS
242. Beate Sitter: TISSUE CHARACTERIZATION BY HIGH RESOLUTION MAGIC ANGLE SPINNING MR SPECTROSCOPY
243. Per Arne Aas: MACROMOLECULAR MAINTENANCE IN HUMAN CELLS – REPAIR OF URACIL IN DNA AND METHYLATIONS IN DNA AND RNA
244. Anna Bofin: FINE NEEDLE ASPIRATION CYTOLOGY IN THE PRIMARY INVESTIGATION OF BREAST TUMOURS AND IN THE DETERMINATION OF TREATMENT STRATEGIES
245. Jim Aage Nøttestad: DEINSTITUTIONALIZATION AND MENTAL HEALTH CHANGES AMONG PEOPLE WITH MENTAL RETARDATION
246. Reidar Fossmark: GASTRIC CANCER IN JAPANESE COTTON RATS
247. Wibeke Nordhøy: MANGANESE AND THE HEART, INTRACELLULAR MR RELAXATION AND WATER EXCHANGE ACROSS THE CARDIAC CELL MEMBRANE

2005

248. Sturla Molden: QUANTITATIVE ANALYSES OF SINGLE UNITS RECORDED FROM THE HIPPOCAMPUS AND ENTORHINAL CORTEX OF BEHAVING RATS
249. Wenche Brenne Drøyvold: EPIDEMIOLOGICAL STUDIES ON WEIGHT CHANGE AND HEALTH IN A LARGE POPULATION. THE NORD-TRØNDELAG HEALTH STUDY (HUNT)
250. Ragnhild Støen: ENDOTHELIUM-DEPENDENT VASODILATION IN THE FEMORAL ARTERY OF DEVELOPING PIGLETS
251. Aslak Steinsbekk: HOMEOPATHY IN THE PREVENTION OF UPPER RESPIRATORY TRACT INFECTIONS IN CHILDREN
252. Hill-Aina Steffenach: MEMORY IN HIPPOCAMPAL AND CORTICO-HIPPOCAMPAL CIRCUITS
253. Eystein Stordal: ASPECTS OF THE EPIDEMIOLOGY OF DEPRESSIONS BASED ON SELF-RATING IN A LARGE GENERAL HEALTH STUDY (THE HUNT-2 STUDY)
254. Viggo Pettersen: FROM MUSCLES TO SINGING: THE ACTIVITY OF ACCESSORY BREATHING MUSCLES AND THORAX MOVEMENT IN CLASSICAL SINGING

255. Marianne Fyhn: SPATIAL MAPS IN THE HIPPOCAMPUS AND ENTORHINAL CORTEX
256. Robert Valderhaug: OBSESSIVE-COMPULSIVE DISORDER AMONG CHILDREN AND ADOLESCENTS: CHARACTERISTICS AND PSYCHOLOGICAL MANAGEMENT OF PATIENTS IN OUTPATIENT PSYCHIATRIC CLINICS
257. Erik Skaaheim Haug: INFRARENAL ABDOMINAL AORTIC ANEURYSMS – COMORBIDITY AND RESULTS FOLLOWING OPEN SURGERY
258. Daniel Kondziella: GLIAL-NEURONAL INTERACTIONS IN EXPERIMENTAL BRAIN DISORDERS
259. Vegard Heimly Brun: ROUTES TO SPATIAL MEMORY IN HIPPOCAMPAL PLACE CELLS
260. Kenneth McMillan: PHYSIOLOGICAL ASSESSMENT AND TRAINING OF ENDURANCE AND STRENGTH IN PROFESSIONAL YOUTH SOCCER PLAYERS
261. Marit Sæbø Indredavik: MENTAL HEALTH AND CEREBRAL MAGNETIC RESONANCE IMAGING IN ADOLESCENTS WITH LOW BIRTH WEIGHT
262. Ole Johan Kemi: ON THE CELLULAR BASIS OF AEROBIC FITNESS, INTENSITY-DEPENDENCE AND TIME-COURSE OF CARDIOMYOCYTE AND ENDOTHELIAL ADAPTATIONS TO EXERCISE TRAINING
263. Eszter Vanky: POLYCYSTIC OVARY SYNDROME – METFORMIN TREATMENT IN PREGNANCY
264. Hild Fjærtoft: EXTENDED STROKE UNIT SERVICE AND EARLY SUPPORTED DISCHARGE. SHORT AND LONG-TERM EFFECTS
265. Grete Dyb: POSTTRAUMATIC STRESS REACTIONS IN CHILDREN AND ADOLESCENTS
266. Vidar Fykse: SOMATOSTATIN AND THE STOMACH
267. Kirsti Berg: OXIDATIVE STRESS AND THE ISCHEMIC HEART: A STUDY IN PATIENTS UNDERGOING CORONARY REVASCULARIZATION
268. Björn Inge Gustafsson: THE SEROTONIN PRODUCING ENTEROCHROMAFFIN CELL, AND EFFECTS OF HYPERSEROTONINEMIA ON HEART AND BONE

2006

269. Torstein Baade Rø: EFFECTS OF BONE MORPHOGENETIC PROTEINS, HEPATOCYTE GROWTH FACTOR AND INTERLEUKIN-21 IN MULTIPLE MYELOMA
270. May-Britt Tessem: METABOLIC EFFECTS OF ULTRAVIOLET RADIATION ON THE ANTERIOR PART OF THE EYE
271. Anne-Sofie Helvik: COPING AND EVERYDAY LIFE IN A POPULATION OF ADULTS WITH HEARING IMPAIRMENT
272. Therese Standal: MULTIPLE MYELOMA: THE INTERPLAY BETWEEN MALIGNANT PLASMA CELLS AND THE BONE MARROW MICROENVIRONMENT
273. Ingvild Saltvedt: TREATMENT OF ACUTELY SICK, FRAIL ELDERLY PATIENTS IN A GERIATRIC EVALUATION AND MANAGEMENT UNIT – RESULTS FROM A PROSPECTIVE RANDOMISED TRIAL
274. Birger Henning Endreseth: STRATEGIES IN RECTAL CANCER TREATMENT – FOCUS ON EARLY RECTAL CANCER AND THE INFLUENCE OF AGE ON PROGNOSIS
275. Anne Mari Aukan Rokstad: ALGINATE CAPSULES AS BIOREACTORS FOR CELL THERAPY
276. Mansour Akbari: HUMAN BASE EXCISION REPAIR FOR PRESERVATION OF GENOMIC STABILITY
277. Stein Sundstrøm: IMPROVING TREATMENT IN PATIENTS WITH LUNG CANCER – RESULTS FROM TWO MULITCENTRE RANDOMISED STUDIES
278. Hilde Pleym: BLEEDING AFTER CORONARY ARTERY BYPASS SURGERY - STUDIES ON HEMOSTATIC MECHANISMS, PROPHYLACTIC DRUG TREATMENT AND EFFECTS OF AUTOTRANSFUSION
279. Line Merethe Oldervoll: PHYSICAL ACTIVITY AND EXERCISE INTERVENTIONS IN CANCER PATIENTS
280. Boye Welde: THE SIGNIFICANCE OF ENDURANCE TRAINING, RESISTANCE TRAINING AND MOTIVATIONAL STYLES IN ATHLETIC PERFORMANCE AMONG ELITE JUNIOR CROSS-COUNTRY SKIERS
281. Per Olav Vandvik: IRRITABLE BOWEL SYNDROME IN NORWAY, STUDIES OF PREVALENCE, DIAGNOSIS AND CHARACTERISTICS IN GENERAL PRACTICE AND IN THE POPULATION
282. Idar Kirkeby-Garstad: CLINICAL PHYSIOLOGY OF EARLY MOBILIZATION AFTER CARDIAC SURGERY

283. Linn Getz: SUSTAINABLE AND RESPONSIBLE PREVENTIVE MEDICINE. CONCEPTUALISING ETHICAL DILEMMAS ARISING FROM CLINICAL IMPLEMENTATION OF ADVANCING MEDICAL TECHNOLOGY
284. Eva Tegnander: DETECTION OF CONGENITAL HEART DEFECTS IN A NON-SELECTED POPULATION OF 42,381 FETUSES
285. Kristin Gabestad Nørsett: GENE EXPRESSION STUDIES IN GASTROINTESTINAL PATHOPHYSIOLOGY AND NEOPLASIA
286. Per Magnus Haram: GENETIC VS. AQUIRED FITNESS: METABOLIC, VASCULAR AND CARDIOMYOCYTE ADAPTATIONS
287. Agneta Johansson: GENERAL RISK FACTORS FOR GAMBLING PROBLEMS AND THE PREVALENCE OG PATHOLOGICAL GAMBLING IN NORWAY
288. Svein Artur Jensen: THE PREVALENCE OF SYMPTOMATIC ARTERIAL DISEASE OF THE LOWER LIMB
289. Charlotte Björk Ingul: QUANITIFICATION OF REGIONAL MYOCARDIAL FUNCTION BY STRAIN RATE AND STRAIN FOR EVALUATION OF CORONARY ARTERY DISEASE. AUTOMATED VERSUS MANUAL ANALYSIS DURING ACUTE MYOCARDIAL INFARCTION AND DOBUTAMINE STRESS ECHOCARDIOGRAPHY
290. Jakob Nakling: RESULTS AND CONSEQUENCES OF ROUTINE ULTRASOUND SCREENING IN PREGNANCY – A GEOGRAPHIC BASED POPULATION STUDY
291. Anne Engum: DEPRESSION AND ANXIETY – THEIR RELATIONS TO THYROID DYSFUNCTION AND DIABETES IN A LARGE EPIDEMIOLOGICAL STUDY
292. Ottar Bjerkeset: ANXIETY AND DEPRESSION IN THE GENERAL POPULATION: RISK FACTORS, INTERVENTION AND OUTCOME – THE NORD-TRØNDELAG HEALTH STUDY (HUNT)
293. Jon Olav Drogset: RESULTS AFTER SURGICAL TREATMENT OF ANTERIOR CRUCIATE LIGAMENT INJURIES – A CLINICAL STUDY
294. Lars Fosse: MECHANICAL BEHAVIOUR OF COMPACTED MORSELLISED BONE – AN EXPERIMENTAL IN VITRO STUDY
295. Gunilla Klensmeden Fosse: MENTAL HEALTH OF PSYCHIATRIC OUTPATIENTS BULLIED IN CHILDHOOD
296. Paul Jarle Mork: MUSCLE ACTIVITY IN WORK AND LEISURE AND ITS ASSOCIATION TO MUSCULOSKELETAL PAIN
297. Björn Stenström: LESSONS FROM RODENTS: I: MECHANISMS OF OBESITY SURGERY – ROLE OF STOMACH. II: CARCINOGENIC EFFECTS OF *HELICOBACTER PYLORI* AND SNUS IN THE STOMACH

2007

298. Haakon R. Skogseth: INVASIVE PROPERTIES OF CANCER – A TREATMENT TARGET ? IN VITRO STUDIES IN HUMAN PROSTATE CANCER CELL LINES
299. Janniche Hammer: GLUTAMATE METABOLISM AND CYCLING IN MESIAL TEMPORAL LOBE EPILEPSY
300. May Britt Drugli: YOUNG CHILDREN TREATED BECAUSE OF ODD/CD: CONDUCT PROBLEMS AND SOCIAL COMPETENCIES IN DAY-CARE AND SCHOOL SETTINGS
301. Arne Skjold: MAGNETIC RESONANCE KINETICS OF MANGANESE DIPYRIDOXYL DIPHOSPHATE (MnDPDP) IN HUMAN MYOCARDIUM. STUDIES IN HEALTHY VOLUNTEERS AND IN PATIENTS WITH RECENT MYOCARDIAL INFARCTION
302. Siri Malm: LEFT VENTRICULAR SYSTOLIC FUNCTION AND MYOCARDIAL PERFUSION ASSESSED BY CONTRAST ECHOCARDIOGRAPHY
303. Valentina Maria do Rosario Cabral Iversen: MENTAL HEALTH AND PSYCHOLOGICAL ADAPTATION OF CLINICAL AND NON-CLINICAL MIGRANT GROUPS
304. Lasse Løvstakken: SIGNAL PROCESSING IN DIAGNOSTIC ULTRASOUND: ALGORITHMS FOR REAL-TIME ESTIMATION AND VISUALIZATION OF BLOOD FLOW VELOCITY
305. Elisabeth Olstad: GLUTAMATE AND GABA: MAJOR PLAYERS IN NEURONAL METABOLISM
306. Lilian Leistad: THE ROLE OF CYTOKINES AND PHOSPHOLIPASE A_2S IN ARTICULAR CARTILAGE CHONDROCYTES IN RHEUMATOID ARTHRITIS AND OSTEOARTHRITIS
307. Arne Vaaler: EFFECTS OF PSYCHIATRIC INTENSIVE CARE UNIT IN AN ACUTE PSYCIATHRIC WARD
308. Mathias Toft: GENETIC STUDIES OF LRRK2 AND PINK1 IN PARKINSON'S DISEASE

309. Ingrid Løvold Mostad: IMPACT OF DIETARY FAT QUANTITY AND QUALITY IN TYPE 2 DIABETES WITH EMPHASIS ON MARINE N-3 FATTY ACIDS
310. Torill Eidhammer Sjøbakk: MR DETERMINED BRAIN METABOLIC PATTERN IN PATIENTS WITH BRAIN METASTASES AND ADOLESCENTS WITH LOW BIRTH WEIGHT
311. Vidar Beisvåg: PHYSIOLOGICAL GENOMICS OF HEART FAILURE: FROM TECHNOLOGY TO PHYSIOLOGY
312. Olav Magnus Søndenå Fredheim: HEALTH RELATED QUALITY OF LIFE ASSESSMENT AND ASPECTS OF THE CLINICAL PHARMACOLOGY OF METHADONE IN PATIENTS WITH CHRONIC NON-MALIGNANT PAIN
313. Anne Brantberg: FETAL AND PERINATAL IMPLICATIONS OF ANOMALIES IN THE GASTROINTESTINAL TRACT AND THE ABDOMINAL WALL
314. Erik Solligård: GUT LUMINAL MICRODIALYSIS
315. Elin Tollefsen: RESPIRATORY SYMPTOMS IN A COMPREHENSIVE POPULATION BASED STUDY AMONG ADOLESCENTS 13-19 YEARS. YOUNG-HUNT 1995-97 AND 2000-01; THE NORD-TRØNDELAG HEALTH STUDIES (HUNT)
316. Anne-Tove Brenne: GROWTH REGULATION OF MYELOMA CELLS
317. Heidi Knobel: FATIGUE IN CANCER TREATMENT – ASSESSMENT, COURSE AND ETIOLOGY
318. Torbjørn Dahl: CAROTID ARTERY STENOSIS. DIAGNOSTIC AND THERAPEUTIC ASPECTS
319. Inge-Andre Rasmussen jr.: FUNCTIONAL AND DIFFUSION TENSOR MAGNETIC RESONANCE IMAGING IN NEUROSURGICAL PATIENTS
320. Grete Helen Bratberg: PUBERTAL TIMING – ANTECEDENT TO RISK OR RESILIENCE ? EPIDEMIOLOGICAL STUDIES ON GROWTH, MATURATION AND HEALTH RISK BEHAVIOURS; THE YOUNG HUNT STUDY, NORD-TRØNDELAG, NORWAY
321. Sveinung Sørhaug: THE PULMONARY NEUROENDOCRINE SYSTEM. PHYSIOLOGICAL, PATHOLOGICAL AND TUMOURIGENIC ASPECTS
322. Olav Sande Eftedal: ULTRASONIC DETECTION OF DECOMPRESSION INDUCED VASCULAR MICROBUBBLES
323. Rune Bang Leistad: PAIN, AUTONOMIC ACTIVATION AND MUSCULAR ACTIVITY RELATED TO EXPERIMENTALLY-INDUCED COGNITIVE STRESS IN HEADACHE PATIENTS
324. Svein Brekke: TECHNIQUES FOR ENHANCEMENT OF TEMPORAL RESOLUTION IN THREE-DIMENSIONAL ECHOCARDIOGRAPHY